Quantum transport and Optical properties of Nanostructure network systems

2006   1

Acknowledgements

"ARIGATOU GOZAIMASHITA."

February 2006, Hiroyuki Ishii

i

Contents

Chapter 1

Introduction

1.1   Nanotechnology and Quantum effects

In the field of semiconductor electronics, the micro-fabrication and integration techniques keep advancing. As a result, the sizes of the fabricated semiconductor devices have achieved the nanometer scale. Another remarkable progress in the production of nanometer scale systems is seen in a recent molecular science field. The control of molecular bonding enables the synthesis of supramolecules, which are made of simple molecules but have the designed bond networks with various shapes. Furthermore, one is also able to observe the surface structures in atomic level and control the single atom movements on the surfaces by dozing electronic current using the scanning tunneling microscopy (STM).

In above mentioned micro systems, the quantum effects appear clearly at the electronic states, and the interesting physical phenomena unable to explain by the classical theories are observed. In this section, we introduce the various physical phenomena originating from quantum effects, such as interference, of these micro systems.

1.1.1   Electronic states of Mesoscopic systems

When sizes of material become gradually small and the physical properties show quantum effects, such materials are called the mesoscopic systems. Some examples of the quantum effects are mainly the interference effect and the confinement effect. The quantum-interference effect originates from the wave character of electrons. On the other hand, the confinement effect makes the energy of electron become discrete values.

The mean free path and the phase coherent length are very important for the mesoscopic systems. The mean free path is average length that electrons go ahead through the system without the inelastic scattering and the elastic scattering. The energy of electron is changed by the inelastic scattering, on the other hand, the elastic scattering doesn't change the energy of electrons. In other words, the phase information of electrons is lost only by the inelastic scattering. The phase coherent length is the length in which electrons go ahead, until the electrons lose the phase information by the inelastic scattering. Examples of the inelastic scattering are
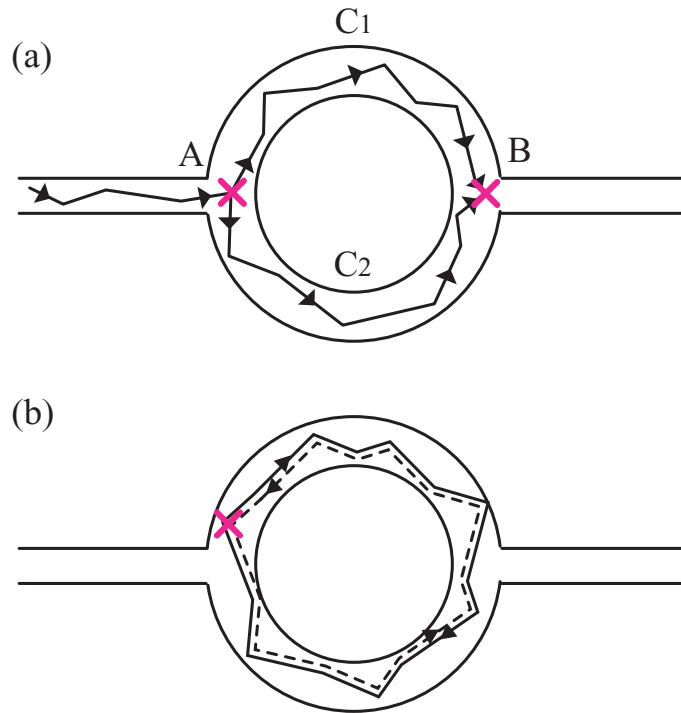
Figure 1.1: (a) Conceptual picture of AB effect. The two waves, which were divided at the entrance of the ring, interfere at the exit of the ring. (b) Conceptual picture of AAS effect. The clockwise wave and the anticlockwise wave produce the localized states in the ring. The electrons go ahead straight until elastic scattering. The electrons hold the phase information in the ring.

the phonon scattering or the scattering by the other electrons. An example of the elastic scattering is the scattering by impurities. Generally, the mean free path is shorter than the phase coherent length. When the system size is smaller than the phase coherent length, the system is a mesoscopic system, because the existence of interference distinguishes the macroscopic system and the mesoscopic system.

The mesoscopic systems are classified into two regions from the viewpoint of the mean free path. When the system size is larger than the mean free path, the physical properties of the system are independent of the shape of the system. It is because the spatial distribution of the phase of electrons is disturbed by the elastic scattering. Such systems are classified into the diffusive conduction region. On the other hand, when the system size is smaller than the mean free path, the shape of the system is important to the conductive properties. Such systems are classified into the ballistic conduction region.

AB and AAS effects

For example, the mean free path of the fine wires fabricated by normal metal is about 100 Å at low temperature. Usually, the system sizes made by normal metals are larger than this length. Thus, the conductive properties are diffusive.

However the interference effect appears in the conductive properties, because the systems hold the phase information. Webb and coworkers observed the resistance of the normal-metal ring under magnetic fields [1]. The conductive properties of the ring as shown in Fig. 1.1(a) were investigated. The wavefunction under a magnetic field satisfies the following Schrödinger equation,

$$\left[\frac{\{\mathbf{p} + e\mathbf{A}(\mathbf{r})\}^2}{2m} + V(\mathbf{r}) \right] \psi(\mathbf{r}) = E\psi(\mathbf{r}), \tag{1.1}$$

where $\mathbf{A}(\mathbf{r})$ is the vector potential. Solving this equation, we obtain the wavefunction at position B shown in Fig. 1.1(a),

$$\psi(\mathbf{r}_B) = \psi_0(\mathbf{r}_B) \exp\left[-\frac{ie}{\hbar} \int_{\mathbf{r}_A}^{\mathbf{r}_B} \mathbf{A}(\mathbf{r}')d\mathbf{r}' \right], \tag{1.2}$$

where $\psi_0(\mathbf{r})$ is the wavefunction in case that no magnetic field is applied to the ring. The line integral is depend on the path from the position A to the position B. Therefore, the phase difference between electrons, which pass through C_1 side of the ring and the C_2 side of the ring, is obtained as,

$$\Delta\theta \equiv \frac{e}{\hbar}\left\{ \int_{C_1} \mathbf{A}(\mathbf{r})d\mathbf{r} - \int_{C_2} \mathbf{A}(\mathbf{r})d\mathbf{r} \right\}. \tag{1.3}$$

The integral is equal to a magnetic flux Φ which penetrates the ring. Thus, we have

$$\Delta\theta = \frac{e\Phi}{\hbar}. \tag{1.4}$$

In case of no magnetic field, the phase difference is zero and the wavefunction ψ is equal to ψ_0. When the magnitude of magnetic field reaches $\Phi = h/(2e)$, the phase difference becomes π. As the result, the wavefunction amplitude at B becomes the node, and the resistance becomes the infinity. When the magnetic field becomes stronger and reaches $\Phi = h/e$, the resistance is equal to that in case of no magnetic field, because the phase difference is 2π. The periodic oscillation of magnetoresistance is called the Aharonov-Bohm effect (AB effect). Figure 1.2(a) shows the experimental result of the magnetoresistance of the normal-metal ring measured at low temperature 0.01K. Periodic oscillations are clearly visible superimposed on a more slowly varying background. The period of the high-frequency oscillations is $\Delta H = 0.00759T$. This period corresponds to the addition of the magnetic flux h/e. The Fourier power spectrum is shown in Fig. 1.2(b). A large peak around $1/\Delta H = 130$ [1/T] corresponds to the component of period $\Phi = h/e$.

There is a secondary large peak around $1/\Delta H = 260$ [1/T] in Fig. 1.2(b). Equations (1.1) and (1.2) show that when there is a clockwise wave in the ring, the anticlockwise wave always exists in the case of no magnetic field. Figure 1.1(b) shows a such situation. Generally, these two wavefunctions interfere each other and produce the localized states in the ring. This localized state doesn't contribute to the conductivity. When a magnetic field is applied to the ring, the field changes the phase of the clockwise wave to $e\Phi/\hbar$. On the other hand, the phase of the
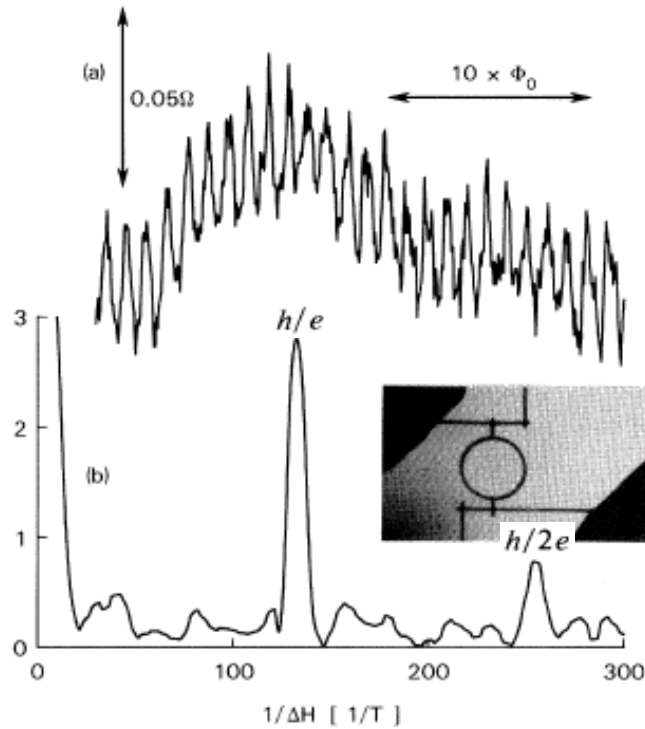
Figure 1.2: (a) Magnetoresistance of the normal-metal ring measured at T=0.01K. (b) Fourier power spectrum of the magnetoresistance [1].

anticlockwise wave is changed to $-e\Phi/\hbar$. Thus, the phase difference between two waves is $2e\Phi/\hbar$. When the phase difference is equal to π, the localized states are destroyed. As a result, the resistance becomes small. When the magnitude of magnetic field becomes larger, the resistance increases again by the interference. Therefore, the period of oscillation of the resistance is $\Phi = h/(2e)$. It is called the Al'tshuler-Aronov-Spivak effect (AAS effect).

Landauer formula

The mean free path of electrons in semiconductor hetero structures is much longer than one in fine wires of normal metal. It is about 50 μm at low temperature. Therefore, we can observe the ballistic transport by using semiconductor hetero structures. In the representative calculation method of the ballistic transport, there is the Landauer formula. To simplify, we consider the system, which consists of only a one-dimensional electrode. The schematic picture is shown in Fig. 1.3(a). We assume that the left and right reservers are filled with electrons up to Fermi energies μ_L and μ_R, respectively. The energies of electrons with wavenumber k in the electrodes are written by $E(k)$. The current of electron with k is defined as

$$I_k = \frac{e}{L}\frac{dE(k)}{\hbar dk},$$
(1.5)

(a)

Electrode

Reserver   Reserver

(b)

L   C   R
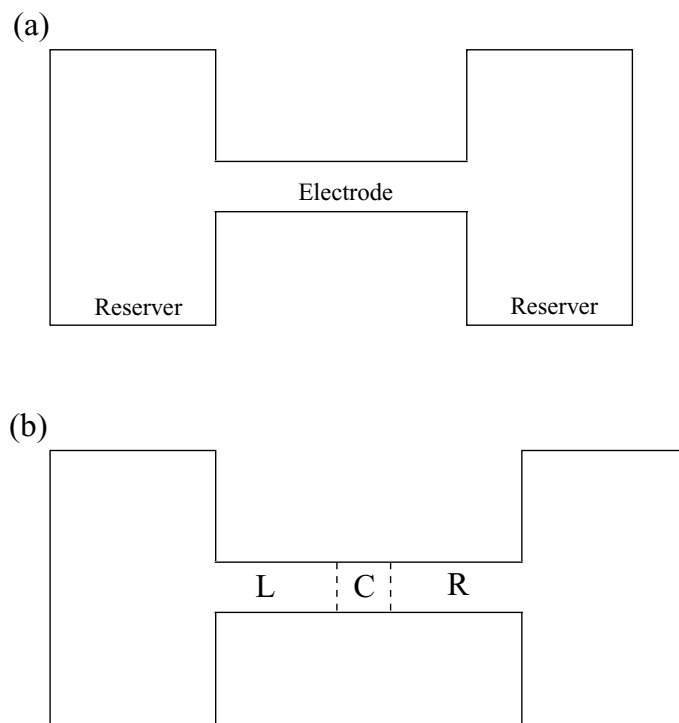
Figure 1.3: The models to obtain the Landauer formula. (a) The left bulk reserver and the right bulk reserver are connected by a fine wire. (b) A nanostructure (C) is sandwiched between the left electrode (L) and the right electrode (R).

where $dE(k)/\hbar dk$ is the group velocity and wavefunction is normalized in the length L. The states whose energies locate between μ_L and μ_R effectively contribute to the electronic current. Therefore we obtain the total electronic current as

$$I = 2 \int_{k_R}^{k_L} I_k \frac{L dk}{2\pi} \tag{1.6}$$

$$= \frac{2e}{h} \int_{k_R}^{k_L} \frac{dE(k)}{dk} dk \tag{1.7}$$

$$= \frac{2e}{h} \int_{\mu_R}^{\mu_L} dE \tag{1.8}$$

$$= \frac{2e}{h}(\mu_L - \mu_R), \tag{1.9}$$

where wavenumber k_L and k_R are defined as $E(k_L) = \mu_L$ and $E(k_R) = \mu_R$, respectively. The source-drain voltage is given by

$$eV \equiv \mu_L - \mu_R. \tag{1.10}$$

Thus, we have the conductance G as follows,

$$G = \frac{I}{V} = \frac{2e^2}{h}. \tag{1.11}$$

Then, as shown in Fig. 1.3(b), we consider the conductance of sample sandwiched between left and right electrodes. In the semiconductor hetero structure, the wavelength of electrons can be smaller than the size of sample. In this case, by the confinement effect, the electronic states in the sample are quantized and have discrete energy levels. When the transmission probability of n-th eigenstate is written by T_n, the conductance of sample is given as

$$G = \frac{2e^2}{h} \sum_n T_n. \tag{1.12}$$

Here, the summation runs over the state whose eigenenergies locate between two Fermi energies of reservers. Equation (1.12) is called the Landauer formula. Wees and coworkers observed the quantized conductance of point contact fabricated by the AlGaAs/GaAs hetero structure. The point-contact layout is shown in inset of Fig. 1.4 [2]. Figure 1.4 shows the point-contact conductance as a function of gate voltage. The conductance shows plateaus at multiples of $e^2/\pi\hbar$, because the transmission probability of n-th eigenstate is 1.

1.1.2   Conductive properties of single molecular systems

It is an ultimate goal in nano-surface science to fabricate atomic and molecular electronic devices and to syntheses novel chemical species with desired performance and properties via controlled surface chemical reactions at the single atomic and molecular scale. Scanning tunneling microscopy (STM) is powerful
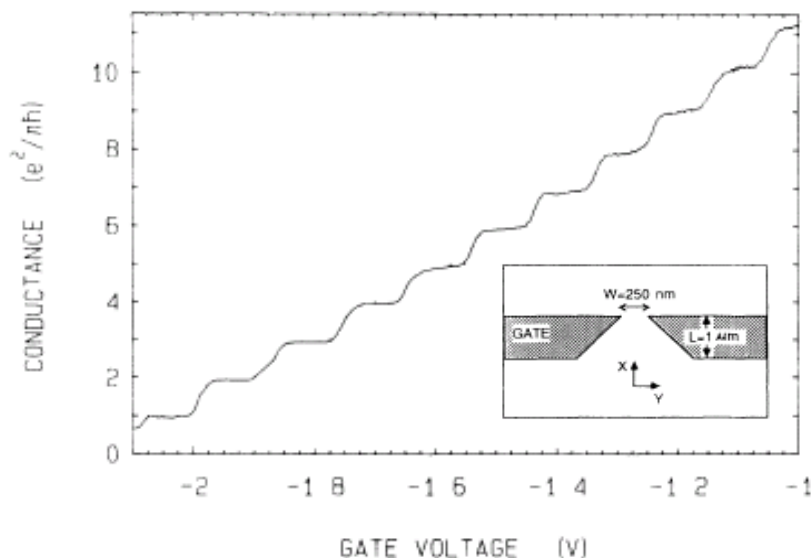
Figure 1.4: Point-contact conductance as a function of gate voltage. Inset is the point-contact layout [2].

tool for nano-surface science. Because, STM has been extending its versatility from the study of surface structural and electronic properties, toward the manipulations of adsorbates at the atomic scale. Various reactions induced by using STM for molecule adsorbed on metal surfaces have been reported, for example, the lateral hopping of carbon monoxide molecules on Pd(110) surface [3], the rotation of acetylene molecules on Cu(100) [4], chemical reaction of *trans*-2-butene molecule on Pd(110) [5], desorption of ammonia molecule on Cu(100) surface [6]. The mechanism of such reactions is that the inelastic current injected from STM tip excites the molecular vibrations and the excited vibrations induce various reactions. A theory of inelastic current which induces the molecular vibrations was first presented by Persson and Baraoff [7] on the basis of the so-called resonance model. It was shown that we can choose the molecular vibration induced by inelastic current by controlling of the magnitude of source-drain voltage applying to the molecule.

1.1.3 The quantum-wire-network or quantum-dot-array systems on semiconductor surfaces

Recent advances in the field of nanotechnology have made it possible to arrange semiconductor quantum wires/dots periodically on semiconductor substrates. In these systems, electrons or holes can move only along wire/dot directions; thus, these systems are sometimes called artificial lattices. The artificial lattices have two fascinating characteristics that are different from those of real crystals. One is the flexibility to design various lattice shapes. For example, using patterning techniques, Fukui and coworkers fabricated square, triangular, and Kagomé

(a)   (b)   (c)
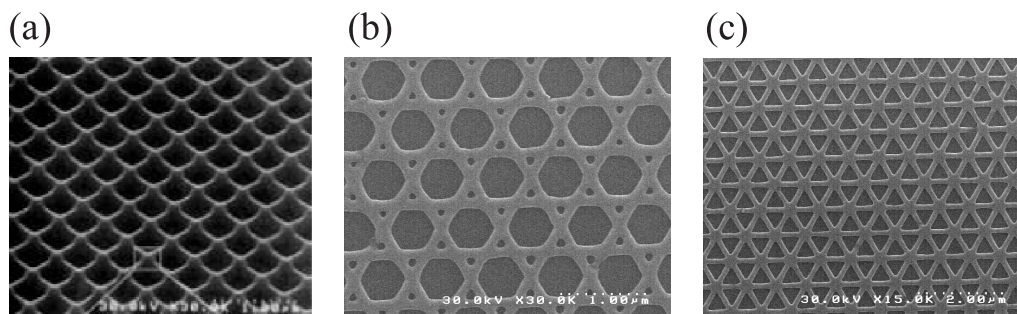
Figure 1.5: The TEM images of (a) the square lattice [8], (b) the Kagome lattice [9,10], and (c) the triangular lattices [11] made of semiconductors. The lattice constant of the Kagomé lattice is 0.72 μm.

(a)   (b)
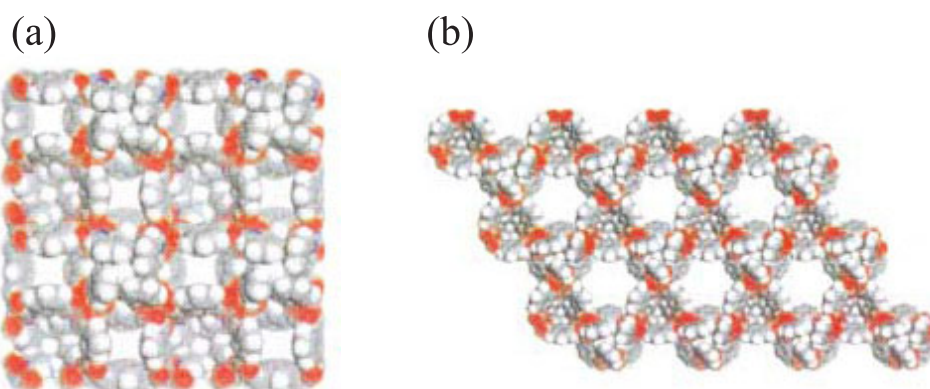
Figure 1.6: The schematic pictures of (a) the square molecular network and (b) the Kagomé molecular network [15].

lattices made of InAs wires on a GaAs substrate as shown in Figs.1.5(a)-(c), respectively [8–11]. Another one is the controllability of the number of electrons in a lattice without Jahn-Teller effect, which is realized by applying a gate voltage [12].

From these characteristics, the artificial lattices provide new stages to demonstrate exotic theoretical predictions for lattice systems. For example, in 1976, Hofstadter predicted theoretically that the two-dimensional lattice systems give fractal energy spectra when an external magnetic field is applied to the systems, by using tight-binding model [13]. In 2001, Albrecht and coworkers produced a two-dimensional square lattice using GaAs quantum wires and showed the existence of fractal energy spectra by applying an external magnetic field [14].

1.1.4   Organic molecular network systems

Remarkable progress in the production of artificial lattice systems is seen in a recent molecular science field [16]. The control of molecular bonding enables
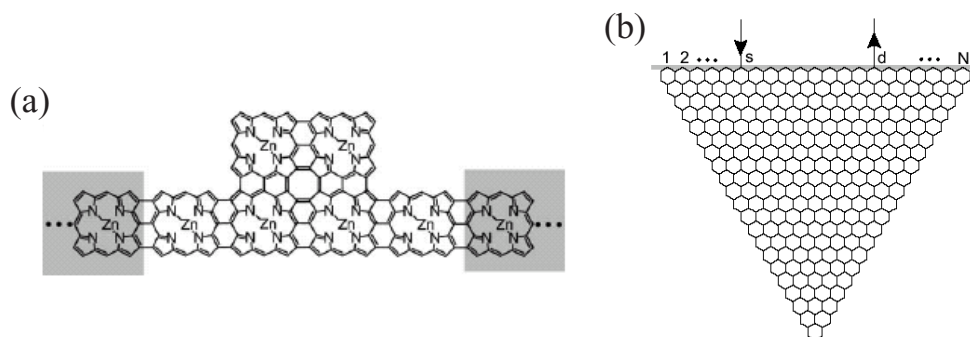
Figure 1.7: The Schematic pictures of (a) the T-shape tape-porphyrin molecular wire [20] and (b) the triangular nanographene molecules [21].
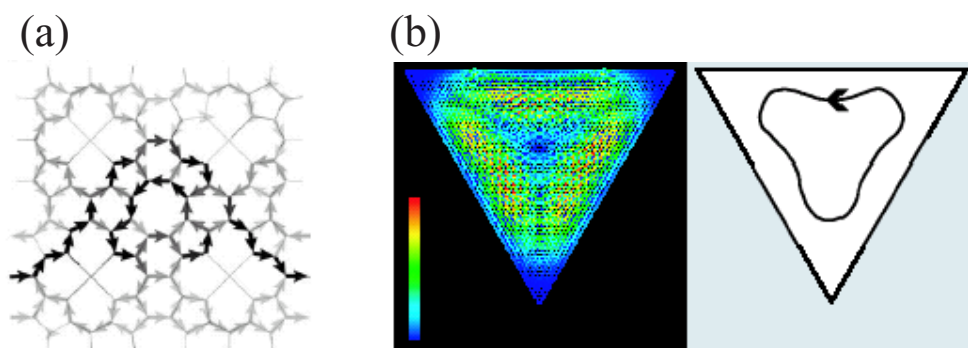
Figure 1.8: The calculated current distribution of (a) the T-shape tape-porphyrin molecular wire [20] and (b) the triangular nanographene molecules [21]. The right schematic picture in Fig. 1.8(b) illustrates the orientation of electronic-current flow.

the synthesis of supramolecules, which are made of simple molecules but have the designed bond networks with various shapes. For example, Moulton and coworkers built large square and Kagomé lattices from simple small molecular polygons by linking them together at vertices or edges as shown in Figs. 1.6(a) and 1.6(b), respectively [15, 17, 18]. Schmitt and coworkers synthesized hybrid organic-inorganic supramolecules, which have honeycomb structures [19]. In addition, many chemists are seeking the modulability of lattice-system's nature due to the incorporation of different guest molecules.

Tagami and Tsukada calculated the electronic transport properties of the T-shape tape-porphyrin molecular wires and triangular nanographene molecules as shown in Figs. 1.7(a) and 1.7(b), respectively [20, 21]. They clarified that the intra-loop current, whose magnitude is much larger than the source-drain-current magnitude, appeared in these systems as shown in Figs. 1.8(a) and 1.8(b). It is because the time-reversal symmetry between the doubly degenerate states of the isolated molecule is broken by contact with source and drain electrodes. Furthermore, they discussed the magnetic properties induced by intra-loop current.
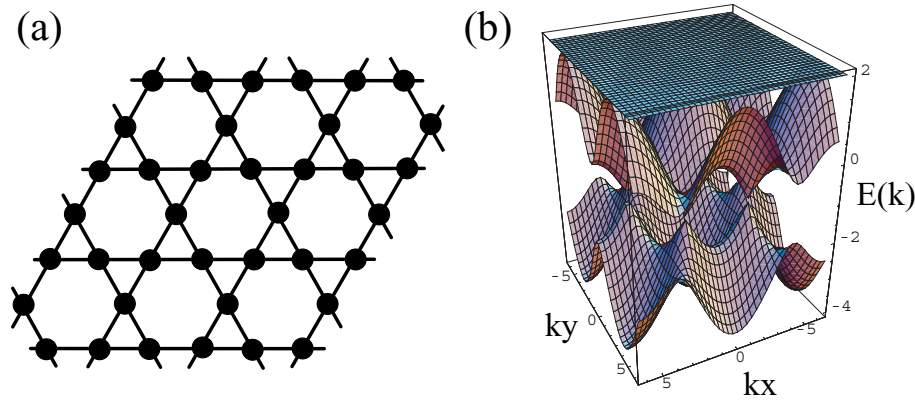
Figure 1.9: (a)The schematic picture of the Kagomé lattice under the tight-binding approximation. (b)The calculated electronic band structure of Kagomé lattice under the tight-binding approximation.

1.1.5   Flat-band systems

Among various lattices, the Kagomé lattice is unique because it has a complete flat band in an electronic band structure. The schematic picture of the Kagomé lattice under the tight-binding approximation is shown in Fig. 1.9(a). The electronic band structure calculated under the tight-binding approximation is shown in Fig. 1.9(b). A flat band appears at the top of the band structure. Mielke clarified that the origin of the flat band appearance is the interference of the electronic wavefunctions reflecting the spatial symmetry of Kagomé lattice [22–24]. The details about the characteristics of flat-band eigenstates are described in next section.

Mielke and Tasaki investigated the magnetic property of the Kagomé lattice by employing a Hubbard model, and showed that the Coulomb repulsive interaction between degenerate flat-band eigenstates induces ferromagnetism when the flat band is half filled with electrons [22–25]. The local spin-density functional calculation based on the effective-mass approximation also showed that the surface ferromagnetism appears on the InAs Kagomé quantum-wire system when the flat band is half filled [12,26]. These type of ferromagnetism is called as flat-band ferromagnetism.

1.2   Characteristics of flat-band eigenstates in electronic-band structures

When the lattice systems have flat bands in the electronic band structures, these flat bands are divided into the following two types.

(1) *The flat-band states originating from spatially localized electrons*

As an example, we consider the electronic band structure in the one-dimensional lattice by using the tight-binding model. Then, the Hamiltonian of electrons

is written as follows,

$$H = -t \sum_{i,j} \hat{a}_i^\dagger \hat{a}_j, \tag{1.13}$$

where t represents the electron transfer energy between nearest-neighbor sites, and $\hat{a}_i$ is an annihilation operator of electron at i-th site. We obtain the electronic band from diagonalization of the Hamiltonian as follows,

$$E(k) = -2t \cos ka, \tag{1.14}$$

where k and a represent the wave vectors and the lattice constant, respectively. This equation shows that when the electron transfer energy becomes zero, the flat band structure appears. That is to say, the electrons, which completely localize spatially at each site, produce the flat-band states. It is not expected that the interesting physical property is obtained in such systems.

(2) *The flat-band states originating from itinerant electrons*

Mielke, Lieb, and Tasaki found that although the conductive electrons run in the lattices, the flat bands appear in the electronic band structures by reflecting the unique spatial symmetry of the lattices [22–25, 27, 28]. These electronic flat-bands have following common characteristics [29].

(a) **localization characteristics:** One can choose eigenstates of a flat band completely localized around one unit cell such that they have no wave-function amplitude outside the unit cell. This occurs due to the specific geometry of the lattice and the interference of the electron wave function. As an example, the flat-band eigenstates in the Kagomé lattice under the tight-binding approximation are shown in Fig. 1.10. One of the flat-band eigenstates is completely localized at the hexagonal area, surrounded by orange solid line. We call the hexagonal area the "plaquette" in this paper. The numbers on the sites represent the wave-function amplitudes.

(b) **itinerant characteristics:** These localized eigenstates are nonorthogonal and have finite overlaps with each other. Thus, the Wannier functions of a flat band are extended over an entire system. On the basis of these facts, one can say that the flat-band electronic states have both localized and itinerant characteristics. In the case of Kagomé lattice, the localized flat-band eigenstate exists in each hexagonal area. Figure 1.10 shows that two localized flat-band eigenstates, surrounded by orange solid line and broken line, have the overlap.

(c) **degenerate characteristics:** Since each unit cell has a localized eigenstate, the sum of such eigenstates becomes a complete set of flat-band states having the same eigenenergy. This feature produces a macroscopic degree of energy degeneracy and becomes the origin of a flat band.
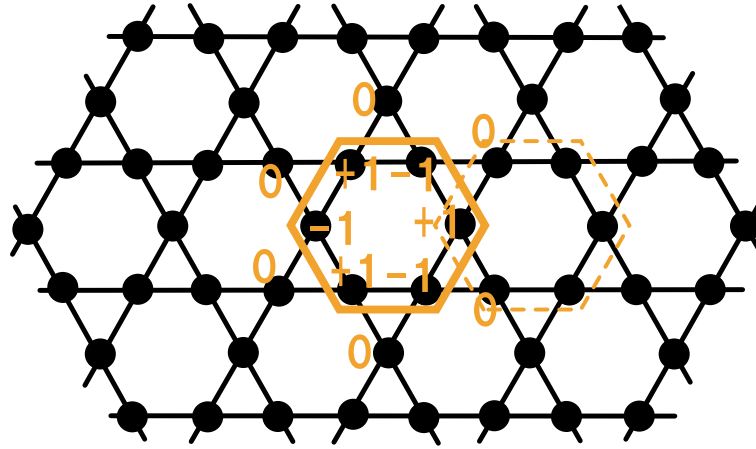
Figure 1.10: One of the localized flat-band eigenstates under the tight-binding approximation.

The reason of existence of flat band originating from itinerant electrons is explained like the following. Although the bandwidth of the flat band is zero, the bandwidth must be finite value in order to permit the electron transfer. To avoid this contradiction, the total bandwidth becomes finite value by having some dispersive bands. One of dispersive bands is changed to the flat band, which has the localized eigenstates by using the interference of the electron wavefunctions. These localized eigenstates have finite overlaps with each other; thus, electrons in a flat band are extended over the systems. The lattices with such flat bands are mainly classified into three types; Lieb type, Tasaki type, and Mielke type. The detailed explanation is described in appendix A.

1.3 Purpose

As shown in the previous sections, the several interesting physical properties which originate from quantum effects, such as interference and degeneracy, at the mesoscopic systems have been reported. In this thesis, therefore, we investigated the quantum transport and optical properties of the nanostructure network systems, which have the unique electronic states induced by the quantum effects.

In chapter 2, we theoretically investigated how quantum effects appear in the optical properties of nanostructure network systems. Concretely, we studied exciton states of the semiconductor Kagomé-lattice systems with flat electronic bands. It is because the flat-band systems have the multiple degenerate states originating from the quantum interference induced by the special symmetry. Furthermore, in chapter 3, we theoretically investigated whether the Kagomé-lattice systems show the conductive nature. Because the flat bands have both the localized and the itinerant characteristics. Recently, in experiments about conductive properties of mesoscopic systems, the energy dissipative process and the dynamics attract

attention. However, the calculation method of time development current has not yet been established. Thus, in chapter 4, we develop the calculation method of time-development current. Finally, we summarized this thesis in chapter 5.

Chapter 2

Optical properties of Flat-band systems

2.1 Purpose

Mielke and Tasaki showed that the Coulomb repulsive interaction between degenerate flat-band eigenstates induces ferromagnetism on the Kagomé lattice system when the flat band is half filled with electrons [22–25]. On the other hand, it is expected that the Coulomb attractive interaction between degenerate eigenstates induces the unique phenomena. Therefore, we investigate the exciton states, which are the bound states of an electron in the conduction band and a hole in the valence band, in the flat-band systems. Especially, we analyze the exciton binding energies and the exciton diameters from the view of the flat-band characteristics, i.e., multiple degenerate, itinerant, and localization characteristics.

The spatial-dimension dependence of exciton binding energies

In this study, we consider the exciton states in two-dimensional artificial lattice systems and one-dimensional quantum dot array made on the semiconductor surface. Before the starting discussions, we review the general characteristics of exciton binding energies [30]. The binding energies E_B of the Wannier excitons which are confined spatially in three, two, and quasi-one dimensional systems are written as follows,

- Three dimensional system

$$E_B \equiv E_0, \tag{2.1}$$

- Two dimensional system

$$E_B = 4E_0, \tag{2.2}$$

- Quasi-one dimensional system

$$E_B = \frac{E_0}{\lambda_0^2} \qquad (\lambda_0 \ll 1), \tag{2.3}$$

where, $E_0 \equiv \hbar^2/(2m_r a_0^2)$, and m_r represents the reduced mass of an electrons and a hole. a_0 is defined by $(\hbar^2 \varepsilon_0)/(m_r e^2)$, where ε_0 represents the vacuum dielectric constant. The quantity λ_0 is decided by the diameter of the quasi-one-dimensional system. When the diameter decreases to zero, λ_0 becomes zero; thus the binding energy of exciton diverges to infinity in the perfect one-dimensional systems.

It is the well-known fact that the binding energies of excitons in spatially high dimensional systems are smaller than those in spatially low dimensional systems.

2.2   Model and Calculation method of exciton states

We investigate the Kagomé quantum-wire system, where the quantum wires are made of InAs and surrounded by $In_{0.72}Ga_{0.28}As$ barrier regions. The width of quantum wires is 10.4 nm, and the lattice constant is 72 nm. A system of this size can be produced by recent nanotechnology [9, 10]. Figure 2.1(a) shows the electron density in the conduction band of this system calculated by the local density approximation [12, 26]. The electron densities at red regions are higher than those at yellow regions. Therefore, Figure 2.1(a) shows that the electron density localizes at the cross points of the quantum wires. A similar result is obtained for the hole density because InAs quantum wires also work to confine holes. Therefore, we assume that the electronic structures of electrons and holes in the lower conduction and higher valence bands are well described by employing the tight-binding model, where electrons and holes are located at the cross points of quantum wires and transfer along the wires. This situation is schematically shown in Fig. 2.1(b). Moreover, an electron and a hole are assumed to be other kinds of fermions, for simplicity [31]. Under these assumptions, the model Hamiltonian of the system becomes

$$\hat{\mathcal{H}} = \sum_{\langle i,j \rangle} t_{ij}^e \hat{a}_i^\dagger \hat{a}_j + \sum_{\langle i,j \rangle} t_{ij}^h \hat{b}_i^\dagger \hat{b}_j + \sum_{i,j} U(r_{ij}) \hat{a}_i^\dagger \hat{a}_i \hat{b}_j^\dagger \hat{b}_j, \qquad (2.4)$$

where $\hat{a}_i$ and $\hat{b}_i$, respectively, represent the annihilation operators of an electron and a hole at the i-th cross point of quantum wires. t_{ij}^e and t_{ij}^h are transfer energies of an electron and a hole from the i-th to the j-th cross points, respectively. The summation $\langle i, j \rangle$ runs over the entire nearest-neighbor cross-point pairs. $U(r_{ij})$ is the Coulomb attraction energy between an electron and a hole, for which we employ the form [31, 32];

$$U(r_{ij}) = \begin{cases} -U_0 & \text{for } i = j \\ -\frac{0.75 U_0}{(r_{ij}/a)} & \text{for } i \neq j, \end{cases} \qquad (2.5)$$

where r_{ij} is the distance between the i and j-th cross points; a represents the distance between the nearest-neighbor cross points of quantum wires evaluated as 36 nm. The employment of this form of Coulomb energy is equivalent to the introduction of the cut-off parameter in one-dimensional systems to avoid the divergence of the eigenvalue of the Hamiltonian (2.4) and corresponds to the screening
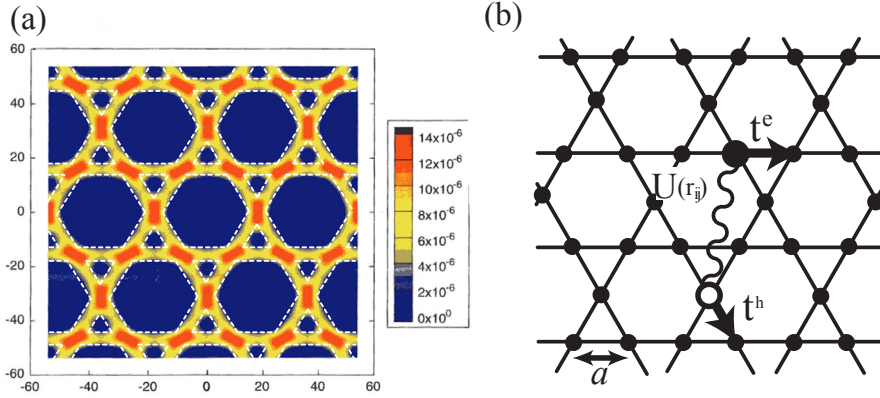
Figure 2.1: (a)A cross sectional view of LSDA-calculated total charge density is shown when five electrons are contained in each unit cell. The electron density localizes at the cross points of the quantum wires [12]. (b)Tight-binding model for exciton state in the Kagomé quantum-wire system. An electron in a conduction band (large solid circle) and a hole in the valence band (large open circle) locate at the cross points of quantum wires, and transfer between two nearest neighbor cross points as shown by arrows. The Coulomb attractive interaction $U(r_{ij})$ works between an electron and a hole.

around the on-site [31, 32]. The band-gap energy between the valence band and the conduction band has an arbitrary value in our model.

We must estimate the transfer energies, t^e and t^h, and the on-site Coulomb energy, U_0, for the InAs Kagomé lattice on the semiconductor surface to evaluate the exciton binding energy. The local density approximation calculation shows that the total width of the conduction bands is about 10 meV as shown in Fig. 2.2(a) [26], while the corresponding bandwidth by the present model is $6t^e$ as shown in Fig. 2.2(b). Therefore, we are able to take the electron transfer energy, t^e, as 1.67 meV. Note that since the lowest energy state at the cross point has the s-like orbital, the s-s coupling between the nearest sites gives a negative value to the electron transfer energy, t^e, in most cases. However, as shown in the subsection 2.3.4, the sign of t^e is easily changed by applying a magnetic field to the lattice system. Thus, in this work, we assume that t^e has a positive value. In this case, the flat band appears as the lowest conduction band. We approximate the hole transfer energy, t^h, equal to the electron transfer energy, t^e, for simplicity. This is because the reduced mass of an electron and a hole in InAs is almost equal to the effective mass of an electron. On the other hand, when an electron and a hole are located at nearest-neighbor sites, the Coulomb attraction energy between them is $-e^2/4\pi\varepsilon a$, where ε represents the relative dielectric constant of InAs, ε=12.4, and e is the elementary electric charge. Thus, the on-site Coulomb energy U_0 is estimated as 4.18 meV.

The wave functions of exciton states are written as follows, because we assume

(a)   (b)
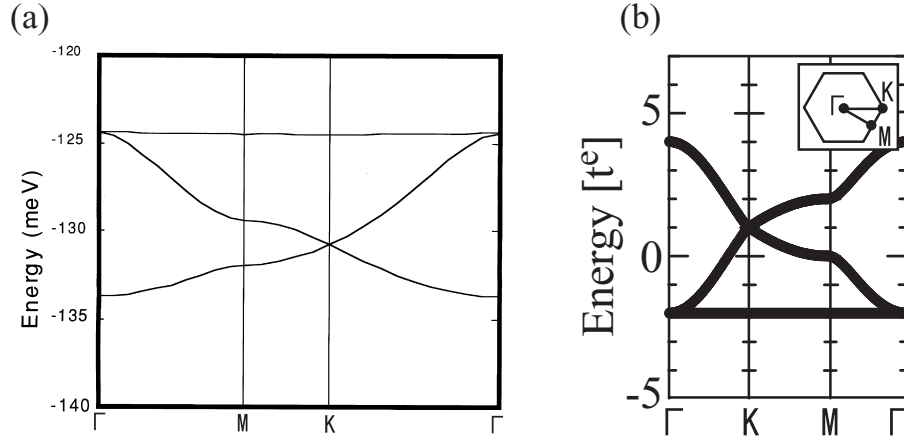
Figure 2.2: Electronic band structures of Kagomé lattice calculated by using (a) the LSDA [26] and (b) the tight-binding model. Insets are the Brillouin zones corresponding to the unit cells in Fig. 2.1(b).

that an electron and a hole are other kinds of fermions,

$$|\Psi\rangle = \sum_{i,j} C_{ij} |i^{(e)}\rangle |j^{(h)}\rangle, \tag{2.6}$$

where $|i^{(e)}\rangle$ represents the base function of electron on i-th site, $|j^{(h)}\rangle$ represents the base function of hole on j-th site. The coefficients $\{C_{ij}\}$ are obtained as the eigenvectors from the diagonalization of Hamiltonian.

The exciton states are obtained as the lowest-energy bound eigenstates of the Hamiltonian. The exciton binding energy, E_B, is calculated as

$$E_B = E(U_0 = 0) - E(U_0 \neq 0), \tag{2.7}$$

where $E(U_0 = 0)$ and $E(U_0 \neq 0)$ are the lowest eigenvalues of the Hamiltonian without and with the Coulomb attraction interaction, respectively. The Hamiltonian is numerically diagonalized by the Lanczos method for Kagomé lattices of finite size as large as 15×15 unit cells with periodic boundary conditions. To check the convergence of the calculated binding energy of exciton, we varied the size of the system and confirmed that the binding energy of an exciton is obtained with 1% accuracy in the present calculation.

2.3   Results and Discussion

2.3.1   Binding energies and radius of exciton

First, we consider the exciton binding energy in the Kagomé lattice. In order to clarify the characteristics of the Kagomé-lattice system, we compare binding energies among various lattice systems. Schematic diagrams of one-dimensional, two-dimensional Kagomé, triangle and square lattices are shown in Figs. 2.3(a) to
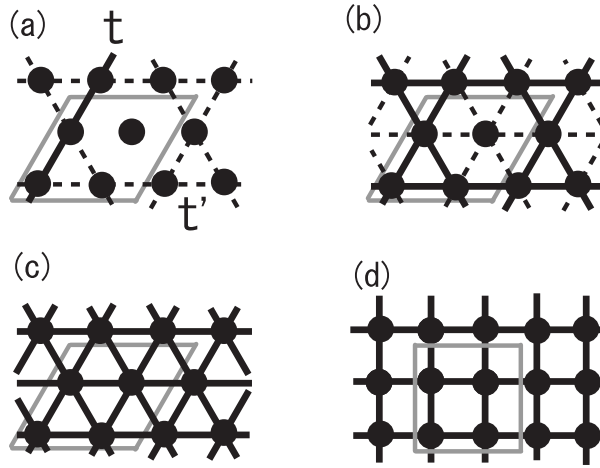
Figure 2.3: The lattice models adopted in this work: (a) one-dimensional, (b) Kagomé, (c) triangle and (d) square lattices. Unit cells of these lattices are shown in (a) to (d) by gray square frames. Kagomé and triangle lattices are obtained from one-dimensional and Kagomé lattices, respectively, by allowing the carrier transfer along broken lines in (a) and (b).

2.3(d) as solid lines, respectively. Unit cells of these lattices are also represented by gray square frames in Figs. 2.3(a) to 2.3(d). The calculated electron and hole band structures of these lattices are shown in Figs. 2.4(a) to 2.4(d). As shown in Fig. 2.4(b), the flat bands appear as the lowest conduction and the highest valence bands for the Kagomé lattice. It should be noted here that when we introduce another transfer energy, t', shown by broken lines in Figs. 2.3(a) and 2.3(b), the triangle and Kagomé lattices are obtained from the Kagomé and one-dimensional lattices, respectively, by changing t' from $t' = 0$ to $t' = t^e = t^h$. This treatment enables us to study the effect of the continuous dimensional change of a lattice from a one-dimensional lattice to a two-dimensional triangle lattice by way of a Kagomé lattice.

Figure 2.5 shows the calculated binding energies of excitons for various lattices. It is seen that the exciton binding energies in the one-dimensional lattice are larger than those in the triangle and square lattices, which is consistent with the familiar knowledge that the exciton binding energy increases as the spatial dimension of the system decreases. However, it should be emphasized that the binding energy in the two-dimensional Kagomé lattice is larger than that in the one-dimensional lattice.

We then consider the spatial localization feature of exciton states. The calculated exciton densities are shown in Figs. 2.6(a) to 2.6(d) for various lattices. In these figures, the electron is fixed on one specific site denoted by white arrows and the hole distribution is displayed. Apparently, all wave functions are s-like nodeless states. To evaluate the localization nature of excitons, the exciton Bohr radius is calculated by fitting the following distribution function to the exciton
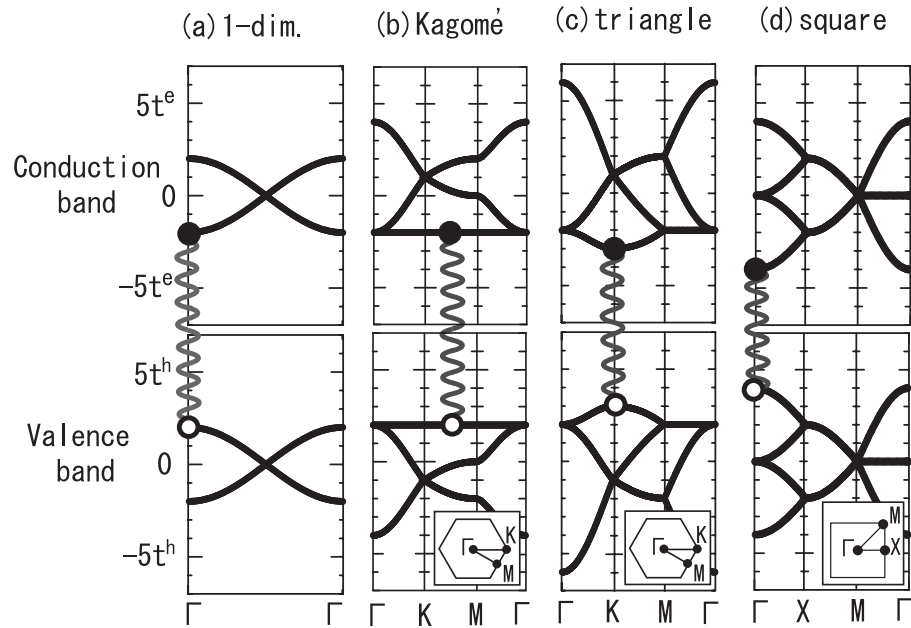
Figure 2.4: The electronic band structure of (a) one-dimensional, (b) Kagomé, (c) triangle and (d) square lattices. Solid and open circles represent an electron state at the bottom of the conduction band and a hole state at the top of the valence band, respectively, and the wavy lines schematically indicate the Coulomb attraction interactions. Insets are the Brillouin zones corresponding to the unit cells in Fig. 2.3.
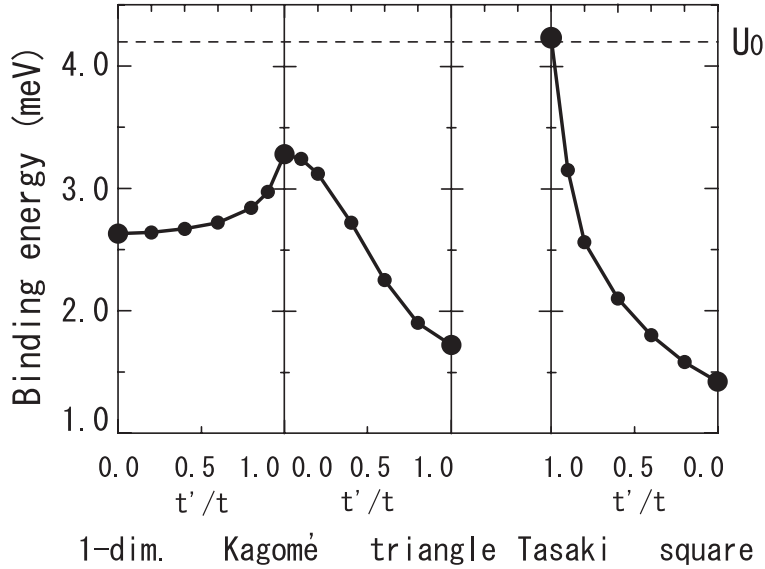
Figure 2.5: Calculated binding energies of excitons for various lattices. Transfer energy, t', which corresponds to the carrier transfer along broken lines shown in Figs. 2.3(a) and (b), is continuously changed from $t' = 0$ to $t' = t = t^e = t^h$, yielding the gradual modification from the one-dimensional and Kagomé lattices to the Kagomé and triangle lattices, respectively. Calculations are performed for the 15×15 unit cells.

density shown in Fig. 2.6,

$$P_h(\mathbf{r}) = P_0 \exp\left[-\frac{2|\mathbf{r} - \mathbf{r}_e|}{\xi} \right]. \tag{2.8}$$

Here, $\mathbf{r}_e$ is the coordinate of the fixed electron and ξ is the exciton radius.

The calculated exciton radiuses are 102, 42, 36, and 108 nm for the one-dimensional, Kagomé, triangle, and square lattices, respectively. Therefore, the excitons are localized in the Kagomé lattice as compared to the one-dimensional and square lattices, which is one of the reasons for the large exciton binding energy in the Kagomé lattice because the binding energy increases as the localization increases. However, excitons in the Kagomé and triangle lattices have almost the same radiuses. This result indicates that the localized nature of excitons alone cannot explain why the excitons in the Kagomé lattice have larger binding energy than those in the other lattices discussed here.

2.3.2 Another flat-band system: Tasaki lattice

Next, we consider the exciton states in another flat-band system, i.e., the Tasaki lattice, which is shown in Fig. 2.7(a) [33]. The electronic band structure of the Tasaki lattice is shown in Fig. 2.7(b). The flat bands appear at the bottom of conduction band and the top of valence band. The exciton state in the Tasaki lattice is calculated in a similar way to those in the other lattices given in the previous subsection. The calculated binding energy is also shown in Fig. 2.5.

Figure 2.6: Calculated exciton densities for various lattices. The electron is fixed on one specific site shown by white arrows and the hole spatial distribution is shown for (a) one-dimensional, (b) Kagomé, (c) triangle and (d) square lattices. White square frames in (a) to (d) are unit cells. Calculations are performed for the 6×6 unit cells.
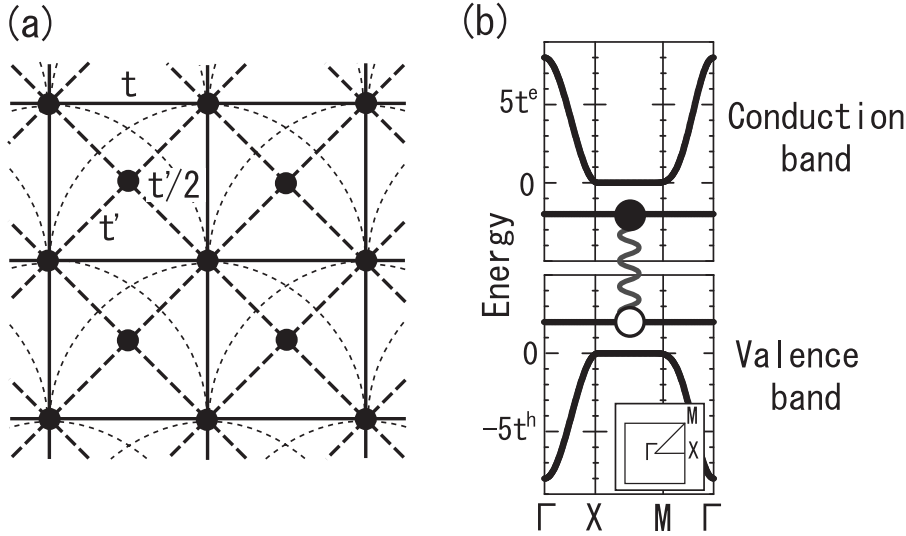
Figure 2.7: (a) Schematic diagram of the Tasaki lattice. In this lattice, the transfer energies of an electron and a hole are t between two sites, which are connected by straight solid lines, while the transfer energies are t' between two sites connected by straight broken lines. The transfer energies represented by broken circular lines are $t'/2$. When $t' = 0$, the lattice corresponds to the square lattice. On the other hand, when $t' = t$, the original Tasaki lattice is obtained. (b) The electronic band structure of the Tasaki lattice with $t' = t$.

It is seen that the exciton binding energy in the Tasaki lattice (4.2 meV) is much larger than that in the Kagomé lattice (3.3 meV). This is because, as shown in Fig. 2.7(b), the Tasaki lattice has the full band gaps between the flat bands and the other normal bands, and thus, the localizations of an electron and a hole state in the flat band are stronger compared to the case of the Kagomé lattice. The calculated exciton radius is shown in Fig. 2.8. It should be noted here that the exciton binding energy is larger than even the on-site Coulomb attraction energy of $U_0 = 4.18$ meV. Note that U_0 is the maximum value of the Coulomb attraction energy for the case of one-site localization of both an electron and a hole. This result clearly indicates that the localized nature of flat-band states is not the unique origin of larger exciton binding energy.

2.3.3 Perturbation analysis of flat-band exciton

To clarify the origin of the large binding energy of an exciton in the flat-band-lattice systems, we perform the perturbation calculations of exciton states using the finite and periodic system. The Coulomb attraction interaction, the third term in Eq. (2.4), is treated as the perturbation term, $\hat{W}$. For simplicity, we assume that the interaction is of short range and works only at the same site as $U(r_{ij}) = -U_0\delta_{ij}$. Moreover, the 2×2 finite Kagomé lattice with the periodic boundary condition is used, together with the corresponding-size square lattice for comparison.
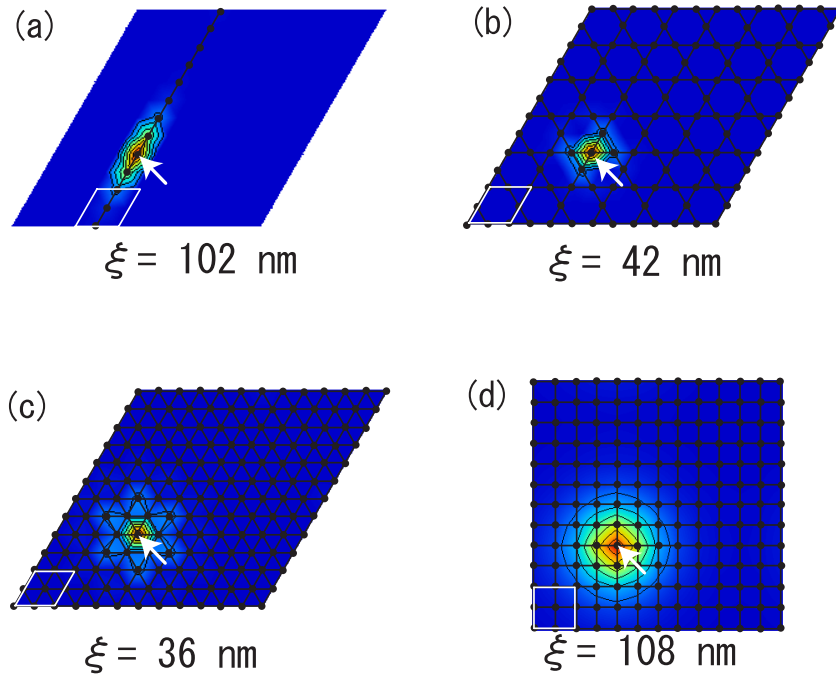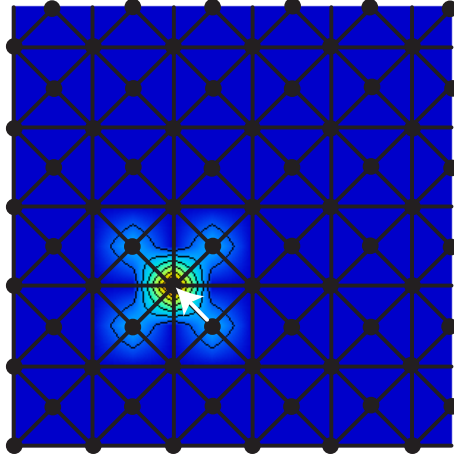
Figure 2.8: Calculated exciton densities for Tasaki lattices. The electron is fixed on one specific site shown by white arrows and the hole spatial distribution is shown. Calculations are performed for the 6×6 unit cells.

In the case of the square lattice, the lowest eigenstate of an electron $|\phi^{(e)}\rangle$ or a hole $|\phi^{(h)}\rangle$ is the linear combination of the i-site localized states, $|i\rangle$, with the same-magnitude coefficients, C_i, as $|\phi^{(e)}\rangle = \sum_i C_i |i\rangle$, where the sign of C_i is given as shown in Fig. 2.9(a). Remember that the electron and hole transfer energies have positive values in this paper, and thus, that coefficients of nearest-neighbor sites have different signs. The unperturbed exciton eigenstate is the tensor product of these states as

$$|\Psi^{(0)}\rangle = |\phi^{(e)}\rangle |\phi^{(h)}\rangle . \tag{2.9}$$

Then, the first-order perturbation gives the binding energy of exciton $E_B^{(1)}$ as

$$E_B^{(1)} = -\langle \Psi^{(0)}|\hat{W}|\Psi^{(0)}\rangle \tag{2.10}$$

$$= +\frac{1}{16} U_0 , \tag{2.11}$$

where the value of denominator, 16, corresponds to the number of the lattice points in Fig. 2.9(a), and reflects the extended nature of electron and hole band states.

In the case of the Kagomé lattice, it is well known that the lowest eigenstates of an electron $|\phi_i^{(e)}\rangle$ and a hole $|\phi_i^{(h)}\rangle$ are the linear combinations of the localized states around hexagonal plaquettes, respectively, as shown in Fig. 2.9(b) [22–24]. Namely, the site coefficients have the same magnitudes and possess the signs as shown in Fig. 2.9(b). Since there are four plaquettes in the present 2×2 lattice, both the eigenstates, $|\phi_i^{(e)}\rangle$ and $|\phi_i^{(h)}\rangle$, are fourfold degenerated with $i, j = 1$ to 4, which is the origin of flat-bands. Since these localized states produce complete sets of flat bands, the unperturbed eigenstates are given by

$$|\Psi_{(i,j)}^{(0)}\rangle = |\phi_i^{(e)}\rangle |\phi_j^{(h)}\rangle, \tag{2.12}$$
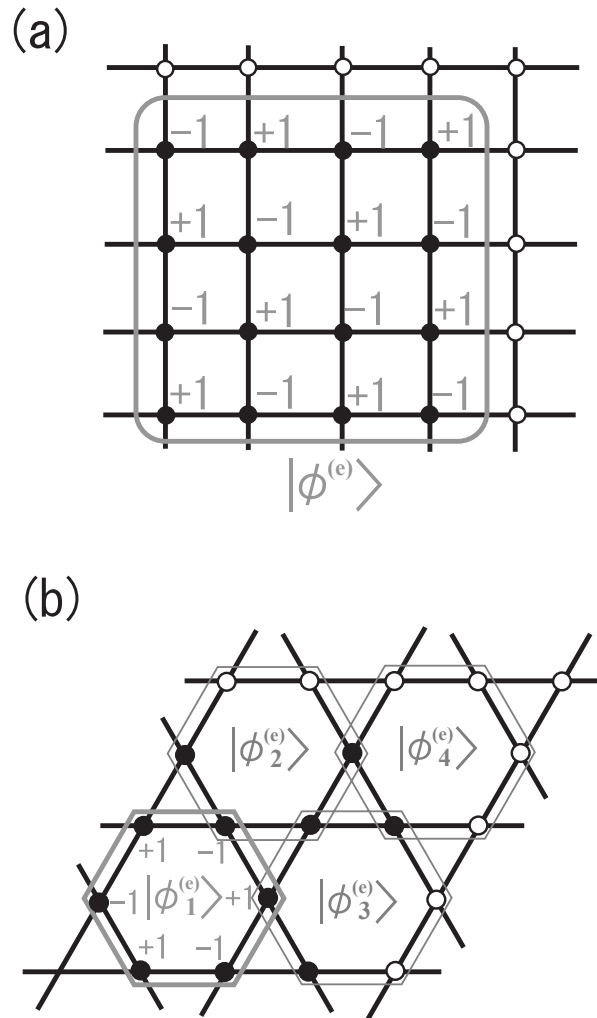
Figure 2.9: Schematic of the lowest eigenstates of a conduction-band electron or a valence-band hole: (a) square and (b) Kagomé lattices. The frames (gray lines) display the localization regions of eigenstates and the inserted numbers on the sites, $+1$ and -1, represent the amplitudes of eigenfunctions. In the case of the Kagomé lattice, the lowest eigenstates are degenerate as shown by $|\phi_1^{(e)}\rangle$ to $|\phi_4^{(e)}\rangle$.

which are 16-fold degenerated. Since these states are nonorthogonal, i.e., overlap each other, we have to apply the degenerate nonorthogonal first-order perturbation to estimate the exciton binding energy, $E_B^{(1)}$, as follows:

$$\sum_{\alpha=1}^{16} C_\alpha \langle \Psi_\beta^{(0)} | W | \Psi_\alpha^{(0)} \rangle = -E_B^{(1)} \sum_{\alpha=1}^{16} C_\alpha \langle \Psi_\beta^{(0)} | \Psi_\alpha^{(0)} \rangle . \tag{2.13}$$

Here, α denotes the basis pair, (i, j).

One can classify the matrix elements in Eq. (2.13) into three groups reflecting the physical characteristics of flat-band states: (i) The diagonal matrix elements of the left-hand side reflect the localized nature of flat-band eigenstates, because $\langle \Psi_\alpha^{(0)} | \hat{W} | \Psi_\alpha^{(0)} \rangle$ is the simple average of the Coulomb interaction by the single state, $|\Psi_\alpha^{(0)}\rangle$, similar to Eq. (2.10). (ii) The nonzero off-diagonal matrix elements have the values of $\pm U_0 / 18$ and appear due to the degeneracy of flat-band states, similar to the case of the usual degenerate perturbation. On the other hand, (iii) the off-diagonal matrix elements of the right-band side reflect the itinerant (nonorthogonal) nature of flat-band states. To clarify the contributions of these three groups of the matrix elements to the exotic exciton state, we multiply off-diagonal matrix elements of a group (ii) by the factor η and those of a group (iii) by the factor ξ. The solution of thus modified Eq. (2.13) gives the exciton binding energy as

$$E_B^{(1)} = \frac{2(2 + 2\eta + \sqrt{1 + 2\eta + 13\eta^2}\,)}{4(9 + 4\xi)} U_0. \tag{2.14}$$

In the case of $\eta = \xi = 0$, which corresponds to the case of neglecting both the itinerant nature and the degeneracy but considering only the localized nature of flat-band states, $E_B^{(1)} = 2U_0/12$. This value is larger than that of the square lattice, which indicates that the exciton in the Kagomé lattice is more localized than that in the square lattice and is consistent with the results of numerical calculation presented previously. We then switch on the factors, η and ξ, step by step as displayed in Fig. 2.10. When we change the value of ξ from 0 to 1, which corresponds to the case considering the itinerant and the localized nature of flat-band states, $E_B^{(1)}$ decreases to $U_0/12$. This is because the itinerant (nonorthogonal) nature induces the extension of the localized flat-band states and gives the loss of attractive Coulomb energy. When both η and ξ have the values of 1, corresponding to the case considering not only the localization and itinerant natures but also the degeneracy of flat-band states, $E_B^{(1)}$ again increases to $3U_0/12$. From this analysis, we can clearly conclude that not only the localization nature, but also the degeneracy of the flat-band eigenstates, is essential origin to enlarge the binding energy of flat-band exciton.

2.3.4   Magnetic field effect

Here, we consider the exciton binding-energy variation when the magnetic field is applied perpendicular to the lattice surface. In the tight-binding model,
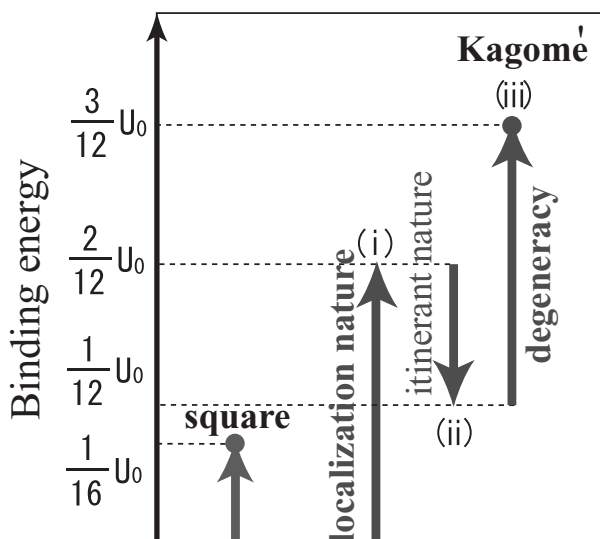
Figure 2.10: Schematic diagram representing contributions to exciton binding energy by the present step-by-step perturbation analysis. (i) localization contribution, (ii) itinerant (nonorthogonal) nature contribution, and (iii) degeneracy contribution. In case of square lattice, only the localization contribution exists.
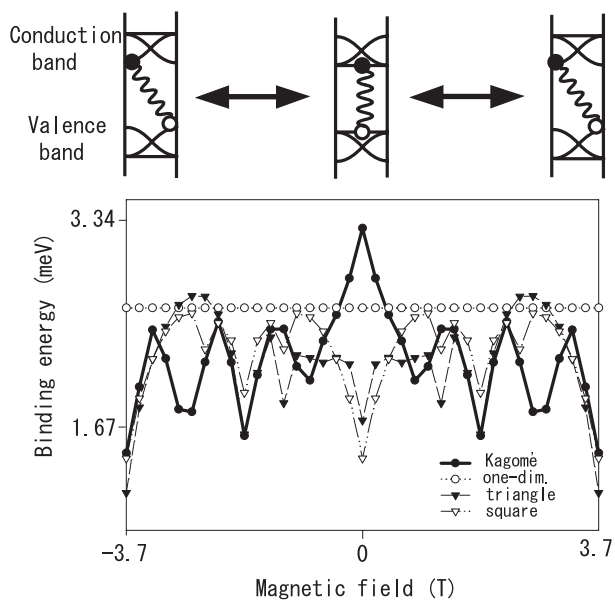
Figure 2.11: Calculated exciton binding energies of various lattices as a function of the magnetic field perpendicular to the lattice plane. Upper panels show the schematic band structures of the Kagomé lattice, in the cases of -3.7T, 0T and 3.7T from the left to the right. Calculations are performed for the 15×15 unit cells.

the magnetic field effect is introduced into the Hamiltonian by multiplying the transfer energy t_{ij} by the phase factor [34],

$$t_{ij} \cdot \exp\left[i\frac{2\pi e}{hc}\int_{\mathbf{r}_i}^{\mathbf{r}_j}\mathbf{A}(\mathbf{r})\,d\mathbf{r}\right], \tag{2.15}$$

where $\mathbf{A}(\mathbf{r})$ is the vector potential, and $\mathbf{r}_i$ is the position vectors of the i-th site.

Figure 2.11 shows the calculated exciton binding energies for various lattices as a function of the magnetic field. Here, in the case of 3.7T, fourfold unit magnetic fluxes are included in the unit cell of the Kagomé lattice. The schematic band structures in the cases of the magnetic fields of -3.7, 0, and 3.7T, without the Coulomb attraction interaction, are also shown in the upper panels of Fig. 2.11. In general, the magnetic field bends the flat-band dispersions and changes the position of flat bands. It is seen in Fig. 2.11 that the binding energy of an exciton in the Kagomé lattice suddenly decreases with applying the magnetic field and that its magnitude becomes comparable to those in other two-dimensional lattices. This result indicates that the large exciton binding energy is obtained only when the flat bands appears as the lowest-conduction and highest-valence bands. Moreover, from this result, we can say that in the Kagomé lattice, one can largely control the binding energy of excitons by applying a magnetic field.

Finally, we comment on the sign of electron and hole transfer energies. As shown in the upper pictures of Fig. 2.11, an electron and a hole transfer energies in the case of ±3.7T are $-t^e$ and $-t^h$, respectively, while those in the case of 0T are t^e and t^h. In this way, we can change the sign of carrier transfer energies by applying an external magnetic field. This is the reason why we take t^e and t^h as positive in section 2.2.

2.3.5   The lattice-constant dependence of exciton binding energies

In the subsection 2.3.1, the calculated exciton binding energy in the Kagomé lattice is 3.3 meV, which is larger than those in the square lattice (1.4 meV) and in bulk InAs (1.6 meV). Thus the difference of binding energy among these systems is observable in careful experiments. However if one produces the Kagomé quantum-wire lattice with small lattice constants, it is expected that the exciton binding energy in the Kagomé lattice becomes much larger. This is because the exciton is localized in one plaquette of the Kagomé lattice, on the other hand, the excitons in other lattices are sufficiently extended. Thus, it is expected that as the lattice size decreases, the exciton-energy difference between the Kagomé and other lattices increases. Therefore, we investigate that how the exciton binding energies change when the lattice constants decrease.

To calculate the lattice-constant dependence of the binding energies, we estimate the lattice-constant dependence of the electron and hole transfer energies by using the square lattice without energy degeneracy. The electronic band structure

of the conduction band bottom or the valence band top is written as,

$$E(\mathbf{k}) = -t\sqrt{4 + 2\cos k_x a + 2\cos k_y a + 4\sqrt{(1 + \cos k_x a)(1 + \cos k_y a)}},$$

(2.16)

where the (k_x, k_y) represents the wave vector. Because the electronic band has the minimum value at Γ point, the $E(\mathbf{k})$ is expanded around Γ point as follows,

$$
\begin{aligned}
E(k) &\simeq -2t\sqrt{2 + 2\cos\left(\frac{ka}{\sqrt{2}}\right)} \\
&\simeq -2t\sqrt{4 - \frac{a^2 k^2}{2}},
\end{aligned}
$$

(2.17)

where $k_x = k_y \simeq k$ has been used. The effective mass, m, at Γ point is defined as

$$\frac{1}{m} = \frac{1}{\hbar^2} \cdot \left.\frac{\partial^2 E(k)}{\partial k^2}\right|_{k=0}.$$

(2.18)

The following form is deduced as transfer energy by using Eq. (2.17) and Eq. (2.18),

$$t = \frac{2\hbar^2}{a^2 m} \propto \frac{1}{a^2}.$$

(2.19)

Equation (2.19) shows that the transfer energy is inverse proportional to the square of the distance, a. On the other hand, we already know that the on-site Coulomb attractive interaction, U_0, is inverse proportional to the distance, a. Thus, when the distance, a, is 18 nm, the transfer energy, t, is estimated as follows,

$$
\begin{aligned}
t &= \frac{1.67\ \text{meV}}{(18\ \text{nm}/36\ \text{nm})^2} \\
&= 6.68\ \text{meV}.
\end{aligned}
$$

(2.20)

The on-site Coulomb interaction attractive interaction is also estimated as

$$
\begin{aligned}
U_0 &= \frac{4.18\ \text{meV}}{(18\ \text{nm}/36\ \text{nm})} \\
&= 8.36\ \text{meV}.
\end{aligned}
$$

(2.21)

We obtain $t = 60.12$ meV and $U_0 = 25.08$ meV, similarly in case of $a = 6$ nm. The calculated binding energies of exciton in various lattice with different lattice constants are shown in Fig. 2.12. The binding energies of excitons in all lattices become larger when the lattice constants decrease. Especially, the binding energies of excitons in the Kagomé lattice are much larger than those of exciton in the other lattices in the case of the distance $a = 6$ nm. Then the binding energy of exciton in the Kagomé lattice reaches about 20 meV, which is observable easily by experiments.
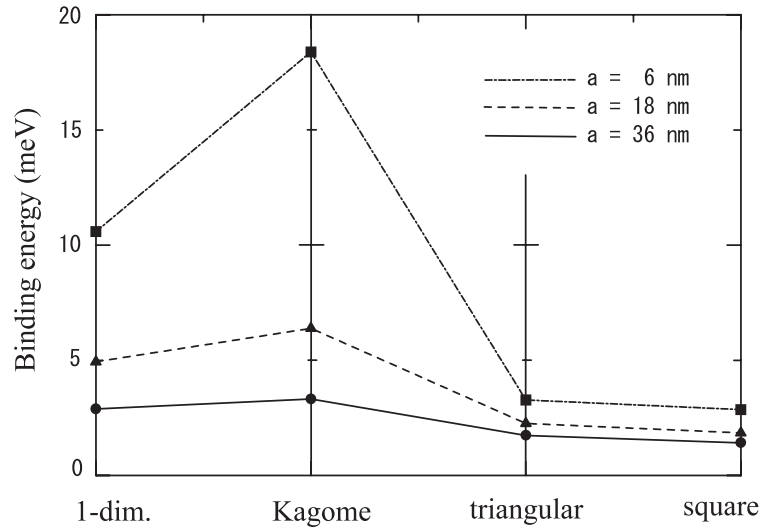
Figure 2.12: The lattice constant dependence of the binding energies of excitons in the one-dimensional, Kagomé, triangular, and square lattices.

2.4   Conclusions

The flat-band exciton in the InAs Kagomé quantum-wire system was studied employing a tight-binding model. We found that the binding energies of flat-band excitons in the Kagomé and Tasaki lattices are much larger than those in other two-dimensional lattices and even larger than that in the one-dimensional lattice. Furthermore, it was found that as the lattice size decreases, the exciton-energy difference between the Kagomé and other lattices becomes larger. By the perturbation analysis, it was shown that both the localized nature and the macroscopic degree of degeneracy of the flat-band eigenstates of electron and hole are the origins of large exciton binding energy. It was also found that when the magnetic field is applied, the binding energy of a flat-band exciton shows a large variation.

Chapter 3

Quantum electron transport properties of Kagomé-lattice-chain systems

3.1   Purpose

The motivation of the present work arises from the simple question whether we can observe the unique features originating from the flat-band states in transport properties. Especially, we note how the flat-band characteristics, i.e. localization and itinerant natures, contribute to the conductivity. Kimura and coworkers calculated the conductivity of the two-dimensional Kagomé lattice with periodic boundary condition using the Drude weights [35], and showed that the group velocity of conduction electrons is zero when the Fermi energy is located at the flat band; thus, the system becomes an insulator. On the other hand, in the presence of a magnetic field, the flat band has a finite dispersion and the group velocity becomes finite, resulting in a metallic behavior. However, in their study, it is not clear what relationship exists between the transport properties and the unique features of flat-band states, because applied magnetic fields are too strong and the flat band is completely broken. Furthermore, using an electric field to remove the degenerate flat-band states localized in each unit cell is more interesting than using a magnetic field, because an electric field has spatial directivity.

In this work, thus, we investigate how the degenerate flat-band states are removed and contribute to the transport properties when a magnitude or a direction of electric field applied to the systems is changed. To apply a finite-magnitude electric field to the Kagomé lattice, we employ the finite-size Kagomé-lattice chain shown in Fig. 3.1(b). From this viewpoint, we investigate the transport properties of the finite-size Kagomé-lattice system under external electric fields, by employing the simple tight-binding model and the nonequilibrium Green function method, and clarify the effects of unique features of flat-band states.

3.2   Model and Calculation method of quantum electron transport

3.2.1   Kagomé-lattice chain

We consider Kagomé-lattice chains shown in Fig. 3.1(b) made of semiconductor quantum-wire and molecular networks. The electrons in the former system are mainly localized at the cross points of wires and move along the wires as shown in Fig. 2.1(a) [12, 26], while those in the latter system are localized on cross-point atoms and transfer between them. Thus, we reasonably assume that the use of the simple tight-binding model to describe the electronic states of these systems is effective [36]. To simplify, we treat electrons as spinless fermions having no Coulomb repulsive interactions, and suppose that one lattice point has one single orbital. Then, the Hamiltonian of this chain is written as

$$\hat{\mathcal{H}}^C = - \sum_{1 \leq i,j \leq N} t\hat{c}_i^\dagger \hat{c}_j + \sum_{1 \leq i \leq N} V_i \hat{c}_i^\dagger \hat{c}_i, \tag{3.1}$$

where $\hat{c}_i^\dagger$ and $\hat{c}_i$ are the creation and annihilation operators of the electron at the i-th site, t the electron transfer energy between the nearest neighboring i- and j-th sites, and N the number of sites in the Kagomé-lattice chain, i.e. $N = 5 \times M + 1$. V_i describes the on-site energy of the i-th site, which represents the effects of external fields. We consider that the entire region of the Kagomé-lattice chain is attached to the gate electrode; thus, all the on-site energies are uniformly varied by applying the gate voltage. Moreover, we apply the external electric field along or perpendicular to the chain, thus changing the on-site energy individually depending on its position. In this case, V_i is written as

$$V_i = V^{\mathrm{G}} + V_i^{\mathrm{E}}, \tag{3.2}$$

where V^{G} is the applied gate voltage, and V_i^{E} represents the potential due to the external electric field whose detailed form is displayed in the following.

Relation between Kagomé-lattice chain and two-dimensional Kagomé lattice

We show that the electronic states of finite-size Kagomé-lattice chains are related to the electronic states of two-dimensional Kagomé lattices. Figure 3.1(a) schematically shows the tight-binding model of a two-dimensional Kagomé lattice, where electrons are localized at solid circles and transfer along the solid lines. As shown in this figure, one of the flat-band eigenstates in this lattice is localized completely in a hexagonal area surrounded by broken lines. We call this area the plaquette in this paper. The other flat-band eigenstates are localized in the other plaquettes, similarly.

When the Kagomé-lattice chain has an infinite length, $M = \infty$, the square region in Fig. 3.1(b) becomes a unit cell of periodicity and the electronic states have the band structure shown in Fig. 3.2(a). Here, we assume that the period equals to $2a$. The flat band appears at the energy of $2t$. On the other hand, in
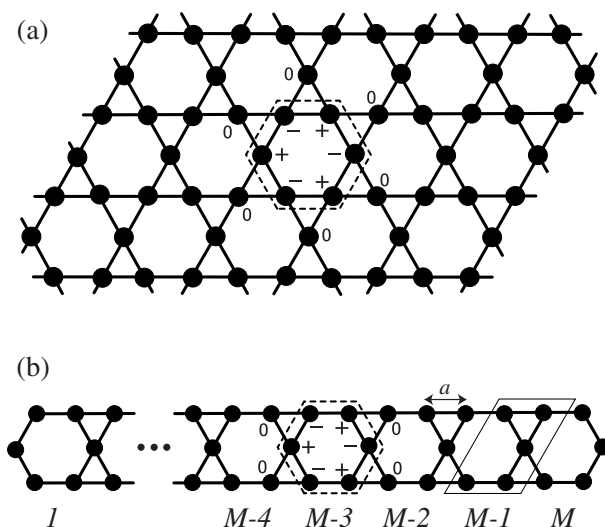
Figure 3.1: Schematic pictures of Kagomé-lattice systems. (a) Two-dimensional Kagomé lattice and (b) M-plaquette Kagomé-lattice chain. In both (a) and (b) lattices, flat-band eigenstates are localized in the hexagonal region surrounded by broken lines. Their wave functions have the same amplitude with alternative signs at every lattice point, while they have no amplitude outside the hexagonal region. The length between the nearest neighbor sites is defined as "a".
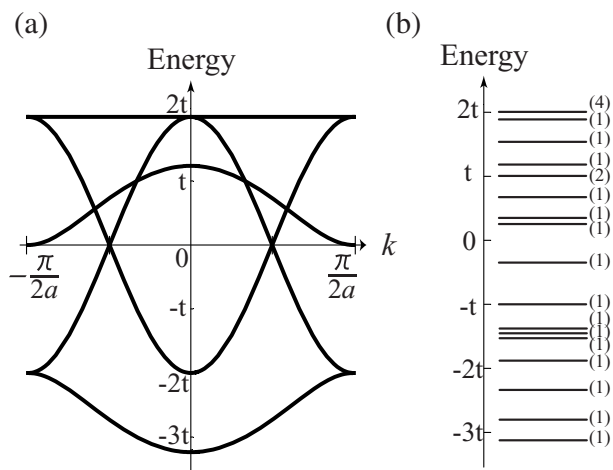
Figure 3.2: (a) Electronic band structure of one-dimensional Kagomé-lattice chain. As shown in Fig. 3.1(b), $2a$ is the periodicity of the lattice along the chain direction. (b) Energy levels of four-plaquette Kagomé-lattice chain. The numbers in parentheses indicate the degree of the energy degeneracy of individual energy levels.
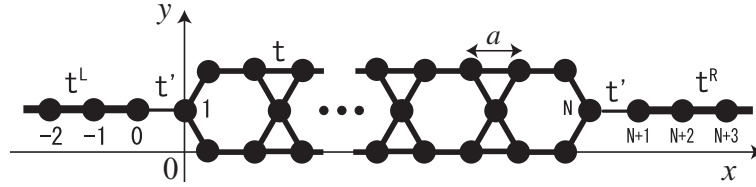
Figure 3.3: Schematic pictures of joint system of finite-size Kagomé-lattice chain and half-infinite electrodes. The transfer energies are shown by various t's. We adopt the x and y axes along and perpendicular to the chain direction.

the case of the Kagomé-lattice chain with a finite M plaquette length, M-fold degenerate states appear at the same energy. For example, Fig. 3.2(b) shows the energy spectra of a four-plaquette Kagomé-lattice chain. The wave functions of the flat-band state in Fig. 3.2(a) and the fourfold degenerate state in Fig. 3.2(b) are localized in one plaquette, as seen in Fig. 3.1(b), similar to the case of two-dimensional Kagomé lattice in Fig. 3.1(a). Here, $+$, $-$ and 0 represent the wave function amplitudes corresponding to $+1/\sqrt{6}$, $-1/\sqrt{6}$ and 0, respectively. Each plaquette in the Kagomé-lattice chain has this type of eigenstate, which produces the flat band in Fig. 3.2(a) or multiple degenerate energy levels in Fig. 3.2(b).

3.2.2   Source and Drain electrodes

To study the transport properties of electrons, the edges of the Kagomé-lattice chain are connected to the source and drain electrodes, as shown in Fig. 3.3. We assume that both electrodes are represented by the tight-binding models of one-dimensional lattices having a half-infinity length. Thus, the Hamiltonian of the electrode is written as

$$\hat{\mathcal{H}}^{\xi} = -\sum_{i,j} t^{\xi} \hat{c}_i^{\dagger} \hat{c}_j + \mu^{\xi} \sum_{i} \hat{c}_i^{\dagger} \hat{c}_i, \tag{3.3}$$

where ξ denotes either left (L) or right (R) electrode. When we number the sites in the electrodes, as shown in Fig. 3.3, the summation runs over the sites with $i \leq 0$ ($i \geq N+1$) for the $\xi = $ L (R) electrode. t^{ξ} is the electron transfer energy between the i- and j-th sites in the ξ electrode, and μ^{ξ} is the chemical potential of electrode. In this case, the electrode is half filled with electrons because the on-site energies are equal to the chemical potential.

3.2.3   Connection to electrode

To study the electron transport properties through the Kagomé-lattice chain, the edges of the chain are connected to the source and drain electrodes, as shown in Fig. 3.3. In order to connect the electrodes to the chain, the following Hamiltonian is introduced,

$$\hat{\mathcal{W}} = -t'(\hat{c}_0^{\dagger} \hat{c}_1 + \hat{c}_1^{\dagger} \hat{c}_0 + \hat{c}_N^{\dagger} \hat{c}_{N+1} + \hat{c}_{N+1}^{\dagger} \hat{c}_N), \tag{3.4}$$

where t' is an electron transfer energy between the Kagomé-lattice chain and electrodes. The total Hamiltonian of the joint system is represented as follows using above Hamiltonians,

$$\hat{\mathcal{H}} = \hat{\mathcal{H}}^L + \hat{\mathcal{H}}^C + \hat{\mathcal{H}}^R + \hat{\mathcal{W}}. \tag{3.5}$$

When the joint system is in the equilibrium state, the electronic states are filled with electrons up to the spatially uniform chemical potential μ, as shown in Fig. 3.4(a). In this equilibrium situation, the electrons can't flow effectively through the Kagome-lattice chain from the left electrode to the right electrode. Thus, we have to employ the nonequilibrium Green function method discussed in section 3.5.

3.2.4 Electronic current formula under the nonequilibrium Green function method

Figure 3.4(b) shows the schematic energy diagram of this joint system under the nonequilibrium state. The electrons transfer from the left electrode to the right electrode passing through the energy-level channels of the central Kagomé-lattice chain. The source-drain voltage V^{sd} is given as $eV^{\mathrm{sd}} = \mu^L - \mu^R$. To scan such channels, we apply the gate voltage V^{G} to the Kagomé-lattice chain to move the energy-level positions. The electronic steady current flowing along the Kagomé-lattice chain is calculated by employing the nonequilibrium Green function method [37,38]. In this method, the Green functions of the electrode and chain, $g(E)$, are separately calculated, assuming that these systems are isolated. Then, we connect the electrodes and chain to calculate the Green functions of the joint system, $G(E)$. The electronic current is obtained using these $G(E)$.

The electronic structure of the Kagomé-lattice chain is obtained by numerically diagonalizing the Hamiltonian (3.1). Using Eq. (3.226), the ij-th site component of the retarded Green function for the Kagomé-lattice chain is obtained as

$$g_{ij}^r(E) = \sum_\alpha \frac{\chi_i^\alpha \chi_j^{\alpha*}}{E - E_\alpha + i\delta}, \tag{3.6}$$

where i and j denote the site numbers from 1 to N, E_α is the eigenenergy of an α-th eigenstate, χ_i^α represents its wave function at the i-th site, and δ is the infinitesimal value. The sum in Eq. (3.6) runs over all the eigenstates of the Kagomé-lattice chain. The advanced Green function $g_{ij}^a(E)$ is obtained using the following relation: $g_{ij}^a(E) = (g_{ji}^r(E))^*$. Using Eq. (3.227), the Keldysh Green function is obtained as

$$g_{ij}^k(E) = (1 - 2f(E))(g_{ij}^r(E) - g_{ij}^a(E)), \tag{3.7}$$

where $f(E)$ shows the Fermi distribution function of the isolated Kagomé-lattice chain. As long as there is no interaction between electrons, the final results with respect to the current do not depend on the choice of this distribution function [39].

Due to the simple nature of one-dimensional terminated lattices, the Green functions for the isolated left and right electrodes are obtained in an analytic form.
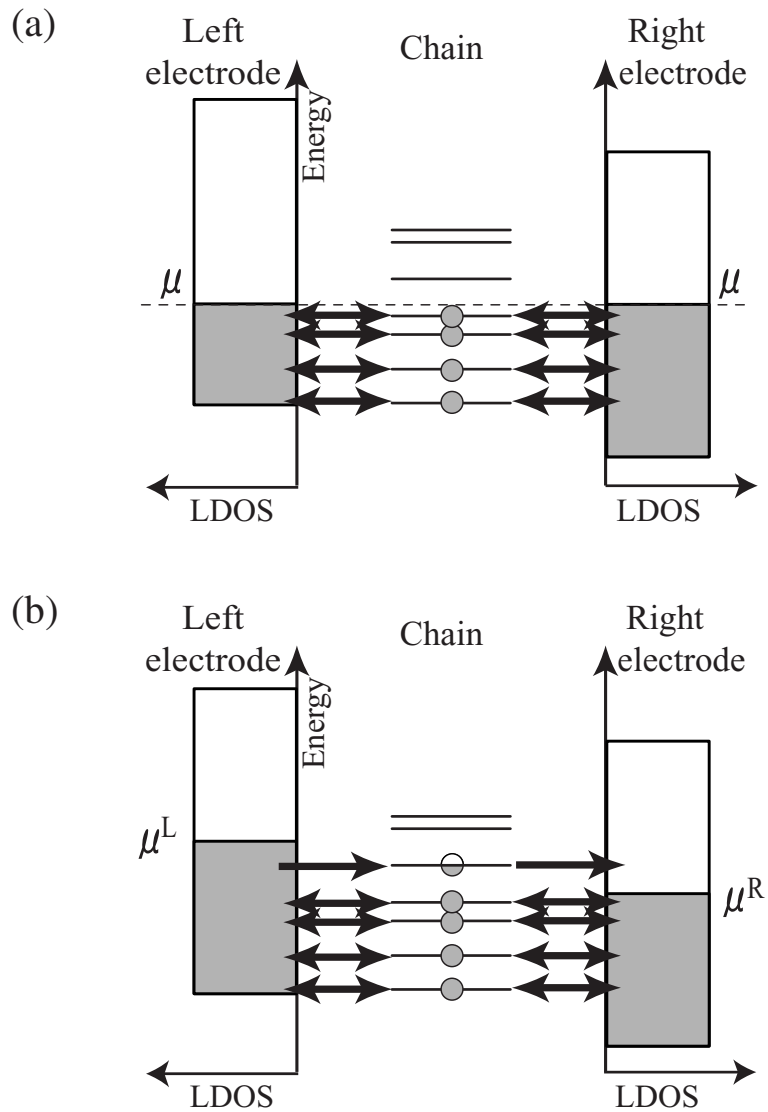
Figure 3.4: (a) Schematic energy diagram of joint system in the equilibrium state. (b) Schematic energy diagram of joint system in the nonequilibrium state. Electrons transfer from the left electrode to the right electrode passing through the energy levels of the center system, as shown by arrows.

For example, the edge components of the retarded Green functions, which will be used to solve the Dyson equation below, are written as (see Eq. (3.197))

$$g_{00}^{r}(E) = \frac{E - \mu^{L} - i\sqrt{4(t^{L})^{2} - (E - \mu^{L})^{2}}}{2(t^{L})^{2}}, \tag{3.8}$$

$$g_{N+1,N+1}^{r}(E) = \frac{E - \mu^{R} - i\sqrt{4(t^{R})^{2} - (E - \mu^{R})^{2}}}{2(t^{R})^{2}}. \tag{3.9}$$

The advanced and Keldysh Green functions are obtained using a formula similar to that in the case of the Kagomé-lattice chain.

Next, we consider the Green functions for the joint system of the Kagomé-lattice chain and two electrodes. First, we introduce the self-energy Σ to connect two electrodes to the Kagomé-lattice chain (see Subsec. 3.5.4). In case shown in Fig. 3.3, the self-energy Σ $(\equiv \Sigma^{r} = \Sigma^{a})$ can be written as

$$\Sigma_{ij} = -t'(\delta_{i,0}\delta_{j,1} + \delta_{i,1}\delta_{j,0} + \delta_{i,N}\delta_{j,N+1} + \delta_{i,N+1}\delta_{j,N}), \tag{3.10}$$

where t' is the transfer energy between an electrode and a Kagomé-lattice chain. Then, we obtain the retarded, advanced, and Keldysh Green functions of the joint system, $\boldsymbol{G}^{r}$, $\boldsymbol{G}^{a}$, and $\boldsymbol{G}^{k}$, by solving the following Dyson equations

$$\boldsymbol{G}^{r}(E) = \boldsymbol{g}^{r}(E) + \boldsymbol{g}^{r}(E)\,\boldsymbol{\Sigma}\,\boldsymbol{G}^{r}(E), \tag{3.11}$$

$$\boldsymbol{G}^{a}(E) = \boldsymbol{g}^{a}(E) + \boldsymbol{g}^{a}(E)\,\boldsymbol{\Sigma}\,\boldsymbol{G}^{a}(E), \tag{3.12}$$

$$\boldsymbol{G}^{k}(E) = \boldsymbol{g}^{k}(E) + \boldsymbol{g}^{k}(E)\,\boldsymbol{\Sigma}\,\boldsymbol{G}^{a}(E) + \boldsymbol{g}^{r}(E)\,\boldsymbol{\Sigma}\,\boldsymbol{G}^{k}(E), \tag{3.13}$$

where we used the matrix representation for the Green functions and the self-energy. Since the self-energy has only a few off-diagonal components, these equations are easily solved.

It is noted that the electronic current at left contact is the same as that at right contact due to charge conservation. Therefore, using the Green functions, the electronic current flowing along the Kagomé-lattice chain is calculated using the current at the left contact as

$$\begin{aligned}
\langle I \rangle &= -\frac{e}{i\hbar}\, t' \langle \hat{c}_{0}^{\dagger}\hat{c}_{1} - \hat{c}_{1}^{\dagger}\hat{c}_{0} \rangle \\
&= -\frac{e}{2h}\, t' \int_{-\infty}^{+\infty} \left(G_{01}^{k}(E) - G_{10}^{k}(E)\right) dE,
\end{aligned} \tag{3.14}$$

where h is a Planck constant [38].

Here, we deduce shortly the analytic forms of the Keldysh Green functions, G_{01}^{k} and G_{10}^{k}, in Eq. (3.14). Using Eqs. (3.11) and (3.12), equation (3.13) is formally solved as follows,

$$\boldsymbol{G}^{k}(E) = \boldsymbol{G}^{r}(E)\boldsymbol{g}^{r}(E)^{-1}\boldsymbol{g}^{k}(E)\boldsymbol{g}^{a}(E)^{-1}\boldsymbol{G}^{a}(E). \tag{3.15}$$

In the case of no Coulomb interaction between electrons, Keldysh Green functions can be written using advanced and retarded Green functions,

$$
\begin{aligned}
G_{01}^k = {}& (1 - 2f^L)G_{00}^r \left(\frac{1}{g_{00}^a} - \frac{1}{g_{00}^r} \right) G_{01}^a \\
& + (1 - 2f^R)G_{0,N+1}^r \left(\frac{1}{g_{N+1,N+1}^a} - \frac{1}{g_{N+1,N+1}^r} \right) G_{N+1,1}^a,
\end{aligned}
\tag{3.16}
$$

$$
\begin{aligned}
G_{10}^k = {}& (1 - 2f^L)G_{10}^r \left(\frac{1}{g_{00}^a} - \frac{1}{g_{00}^r} \right) G_{00}^a \\
& + (1 - 2f^R)G_{1,N+1}^r \left(\frac{1}{g_{N+1,N+1}^a} - \frac{1}{g_{N+1,N+1}^r} \right) G_{N+1,0}^a,
\end{aligned}
\tag{3.17}
$$

where f^L and f^R represent the Fermi distribution functions of electrons in the left and right electrodes, respectively. We can confirm that the current is independent of the Fermi distribution function of the isolated Kagomé-lattice chains. Solving the Dyson equations (3.11), the retarded Green functions are obtained by using the unperturbed Green functions as follows,

$$
G_{00}^r = g_{00}^r \frac{1 - g_{NN}^r t' g_{N+1,N+1}^r t'}{\Gamma^r},
\tag{3.18}
$$

$$
G_{01}^r = \frac{1}{t'} \left(-1 + \frac{1 - g_{NN}^r t' g_{N+1,N+1}^r t'}{\Gamma^r} \right),
\tag{3.19}
$$

$$
G_{0,N+1}^r = \frac{g_{00}^r t' g_{1N}^r t' g_{N+1,N+1}^r}{\Gamma^r},
\tag{3.20}
$$

$$
G_{N+1,1}^r = \frac{g_{N+1,N+1}^r t' g_{N1}^r}{\Gamma^r},
\tag{3.21}
$$

where

$$
\begin{aligned}
\Gamma^r = {}& 1 - g_{00}^r t' g_{11}^r t' - g_{NN}^r t' g_{N+1,N+1}^r t' \\
& + g_{00}^r t' g_{11}^r t' g_{NN}^r t' g_{N+1,N+1}^r t' \\
& - g_{00}^r t' g_{1N}^r t' g_{N+1,N+1}^r t' g_{N1}^r t'.
\end{aligned}
\tag{3.22}
$$

We can obtain similarly the advanced Green functions. Using the charge conservation law, i.e., $(G_{01}^k - G_{10}^k) = (G_{N,N+1}^k - G_{N+1,N}^k)$, the formula (3.14) can be transformed into a more understandable one:

$$
\begin{aligned}
\langle I \rangle = {}& 4 \frac{e}{h} t'^4 \int_{-\infty}^{+\infty} dE \, (f^L(E) - f^R(E)) \\
& \mathrm{Im}[g_{00}^a(E)] \, G_{1N}^r(E) \, G_{1N}^a(E) \, \mathrm{Im}[g_{N+1,N+1}^a(E)],
\end{aligned}
\tag{3.23}
$$

where the Green function G_{1N}^r is defined by g_{1N}^r / Γ^r. The Green function G_{1N}^a is defined similarly. In this formula, t' indicates the coupling between the Kagomé-lattice chain and two electrodes, while $\mathrm{Im}[g_{00}^a]$ and $\mathrm{Im}[g_{N+1,N+1}^a]$ are the electron densities of states of the left and right electrodes. The part $G_{1N}^r G_{1N}^a$ is the transport probability from the left edge to the right edge of the Kagomé-lattice chain. The local densities of states (LDOS) at various site of left electrode are shown in
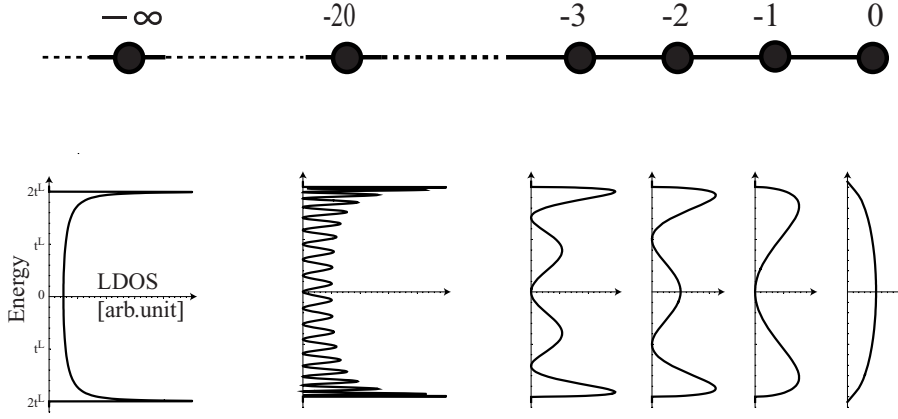
Figure 3.5: The calculated electron local densities of states at 0-, -1-, -2-, -3-, -20-, and -∞-th site of the left electrode.

Fig. 3.5. The electronic band structure of infinite one-dimensional lattice diverges at the band edge. However, in case of a half-infinity-length electrode, the local density of state at the edge of the electrode doesn't have divergence. The electron number density at the i-th site is similarly calculated as

$$\langle n_i \rangle = \langle \hat{c}_i^\dagger \hat{c}_i \rangle$$
$$= -\frac{i}{4\pi} \int_{-\infty}^{+\infty} \left(-G_{ii}^r(E) + G_{ii}^a(E) + G_{ii}^k(E) \right) dE. \tag{3.24}$$

We calculate the current vs gate-voltage spectra using Eq. (3.14), while we analyze such spectra using Eq. (3.23).

3.2.5   Calculation parameters

In the calculation of the current passing through the Kagomé-lattice chain, one has to determine relevant energy parameters. We first choose the transfer energy in the Kagomé-lattice chain, t, as an energy unit standard. t' is the coupling between the electrode and the Kagomé-lattice chain, which induces the changes in electronic states in the Kagomé-lattice chain when the connection is realized. To observe the characteristic features of electronic states in the Kagomé-lattice chain, a small value is desirable for t'; thus, we adopt $t' = 0.1t$. On the other hand, the transfer energies t^L and t^R determines the bandwidths of the electrodes. To avoid the singularity of a one-dimensional band, a large $60t$ is used for both t^L and t^R.

The difference in chemical potential between the left and right electrodes, $\mu^L - \mu^R$, corresponds to the applied source-drain voltage V^{sd}. The every discrete energy levels under the Fermi energies of the left or right electrodes contribute to the electronic current. However, in the case of no Coulomb interaction between electrons, the energy levels under the both μ^L and μ^R don't contribute effectively to the current, because the current flowing from the left to right electrodes is equal to one from right to left electrodes when the energy level locate under the both μ^L and μ^R. As a result, the only energy levels located between two Fermi energies

contribute to the electronic current. Actually, using Eq. (3.24), we have confirmed that the energy levels under the two Fermi energies are filled with electrons as shown in Fig. 3.4(b). Thus, as seen in Fig. 3.4(b), the energy difference between two Fermi energies determines the width of energy window, which is used to scan the current channels in the Kagomé-lattice chain and determine the spectral resolution. For example, if we increase $\mu^L - \mu^R$, the number of current channels between the chemical potentials increases and the current spectra become broad. The source-drain voltage dependence of the current vs gate-voltage characteristics is shown in Figs. 3.21(a)-(c) in Sec. 3.6. To observe each channel separately, V^{sd} should be smaller than various t's, thus a value of $V^{sd} = 0.05t$ is adopted.

On the other hand, the inverse temperature, $\beta = 1/k_B T$, appearing in the Fermi distribution functions of the electrodes represents the broadening of the electron occupation around the chemical potentials, thus simply promoting the broadening of the current spectra. The temperature dependence of the current vs gate-voltage characteristics is shown in Fig. 3.22 in Sec. 3.6. Since we are not interested in such broadening, a small value of $\beta^{-1} = 0.01t$ is used in this work.

The imaginary part of the denominator of the Green function in Eq. (3.6), δ, denotes the inverse of the lifetime of the electronic states in the Kagomé-lattice chain reflecting the scatterings of electrons by other freedoms such as lattice vibrations. We assume that there is no scattering and use an infinitesimal value, $\delta = 10^{-8}t$. This small value is sufficient in maintaining the charge conservation in the numerical calculation. The current passing through the Kagomé-lattice chain is calculated numerically using the formula (3.14). In the integration of Eq. (3.14), we adopt the energy mesh having the interval of $10^{-9}t$. By varying the values, we found that the above values ensure the numerical accuracy of the calculated current with a relative error of 10^{-6}.
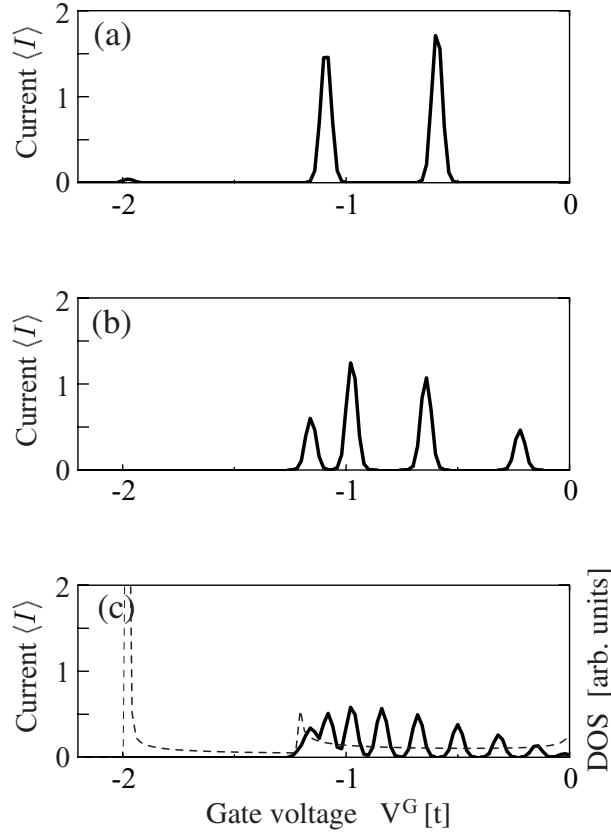
Figure 3.6: Calculated current vs gate-voltage characteristics of (a) two-, (b) four-, and (c) ten-plaquette Kagomé-lattice chains in case of without external electric field. The unit of current is $10^{-4}|t|^2 e/h$. The broken line in (c) denotes the density of states of the Kagomé-lattice chain with an infinite length.

3.3 Results and Discussion

3.3.1 Current vs gate-voltage spectra

We first study the general features of the electronic current flowing through the Kagomé-lattice chain in the case when there is no external electric field. Figures 3.6(a)-3.6(c) show the calculated currents of the Kagomé-lattice chains with two, four, and ten plaquettes, respectively, as a function of the applied gate voltage. The broken line in Fig. 3.6(c) represents the density of states of the Kagomé-lattice chain having an infinite length.

In these figures, the flat-band channel is located at $V^G = -2t$, which is recognized by observing the energy spectra in Figs. 3.2(a) and 3.2(b) or the density of states in Fig. 3.6(c). It is seen that the currents through the flat-band channel are almost zero for the chains with $M = 4$ and 10 plaquettes, being in agreement with the calculation by Kimura *et al.* [35]. This result occurs because of the infinite effective mass, i.e., localized nature, of the flat-band states, the details of which are discussed later. On the other hand, a small peak appears at $V^G = -2t$ in Fig.

3.6(a) due to the finite-size effect of the Kagomé-lattice chain.

The other current peaks seen in the region from $V^G = -1.3t$ to 0 originate from normal-band channels. As the length of the chain increases, the number of peaks increases in this region and the magnitude of each peak decreases. These changes occur due to the formation of an electronic band structure; the number of electronic states in one band increases in proportion to the length of the Kagomé-lattice chain. On the other hand, since the electronic states in such a normal band are extended and the amplitude of their wave functions at the edges, i.e., at $n = 1$ and N sites, is proportional to the inverse of the system size, the transfer probability of electrons from the left edge to the right edge of the chain decreases as the length of the chain increases.

The current-peak magnitude of normal-band channel can be estimated in an analytic form using approximate Green functions. For the isolated Kagomé-lattice chain, when the α-th eigenstate has the energy E_α with no degeneracy, the Green function around $E = E_\alpha$ is approximately given as

$$g_{ij}^r(E \sim E_\alpha) \simeq \frac{\chi_i^\alpha \chi_j^\alpha}{E - E_\alpha + i\delta}. \tag{3.25}$$

For the isolated left electrode, since the bandwidth is large such as $|t^L| \gg |E - \mu^L|$, we can approximate the Green function as

$$g_{00}^r \simeq -i\frac{1}{t^L}. \tag{3.26}$$

Similar formulas can be used for $g_{N+1,N+1}^r$ of the right electrode. Using these Green functions and solving the Dyson equation, the Green function G_{1N}^r of the joint system is written as

$$G_{1N}^r(E \sim E_\alpha) = \frac{g_{1N}^r}{\Gamma^r} \tag{3.27}$$

$$\simeq \frac{\frac{\chi_1^\alpha \chi_N^\alpha}{E - E_\alpha + i\delta}}{1 + it'^2 \left(\frac{1}{t^L}\frac{\chi_1^\alpha \chi_1^\alpha}{E - E_\alpha + i\delta} + \frac{1}{t^R}\frac{\chi_N^\alpha \chi_N^\alpha}{E - E_\alpha + i\delta}\right)} \tag{3.28}$$

$$\simeq \frac{\chi_1^\alpha \chi_N^\alpha}{E - E_\alpha + i\Delta}, \tag{3.29}$$

where Δ represents the broadening of the energy level due to the contact to the electrodes and is given by

$$\Delta = \delta + \frac{t'^2}{t^L}\chi_1^\alpha \chi_1^\alpha + \frac{t'^2}{t^R}\chi_N^\alpha \chi_N^\alpha. \tag{3.30}$$

Noting that δ is infinitely small. Using above approximated Green functions, when the temperature is zero, the current formula (3.23) can be rewritten as

$$\langle I \rangle \sim 4\,\frac{e}{h}\,\frac{t'^4}{t^L t^R}\int_{\mu^R}^{\mu^L} dE\; G_{1N}^r\, G_{1N}^a. \tag{3.31}$$

After carrying out the integration of above equation, the current magnitude is obtained as follows,

$$\langle I \rangle \sim 4\frac{e}{h}\frac{t'^4}{t^L t^R}\sum_{\alpha}\int_{\mu^R}^{\mu^L} dE \frac{(\chi_1^\alpha \chi_N^\alpha)^2}{(E - E_\alpha + i\Delta)(E - E_\alpha - i\Delta)}, \tag{3.32}$$

$$\sim 4\frac{e}{h}\frac{t'^4}{t^L t^R}\sum_{\alpha}\frac{\pi(\chi_1^\alpha \chi_N^\alpha)^2}{\Delta}, \tag{3.33}$$

where the summation in Eq. (3.33) runs over the discrete energy levels between two Fermi energies of the electrodes. We assume that every χ^α is roughly given as $1/\sqrt{N}$, because the normal state expands in the whole chain system. Then, the current magnitude is obtained as

$$\langle I \rangle = \sum_{\alpha}\langle I_\alpha \rangle, \tag{3.34}$$

where

$$\langle I_\alpha \rangle = 2\pi\frac{e}{h}\frac{t'^2}{t^L N}. \tag{3.35}$$

Here, $t^L = t^R$ has been used. $\langle I_\alpha \rangle$ is the current magnitude through the α-th eigenstate. This equation clearly shows that the current peak intensities in the normal-band channels decrease with increasing size of the Kagomé-lattice chain.

As seen in Figs. 3.2(a) and 3.2(b), normal-band electronic states also exist in the energy region from $+1.3t$ to $+2t$. However, one cannot see any current peaks in the region from $V^G = -2t$ to $-1.3t$ in Figs. 3.6(a)-3.6(c). This result is related to the symmetry of the present joint system. The Kagomé-lattice chain has a reflection symmetry along the y direction in Fig. 3.3. The normal-band electronic states in the region from $1.3t$ to $2t$ have an *ungerade* symmetry and the amplitudes of their wave functions are exactly zero at the $n = 1$ and N sites, where the connection to the electrodes is realized. Thus, the transport of electrons is inhibited through these channels. In fact, when we change the contact sites to the electrode, the current peaks are revealed. As an example, an *ungerade* eigenstates of four-plaquette length Kagomé-lattice chain is shown in Fig. 3.7. This state locates at the neighbor of the flat-band states.

Finally, we briefly comment on the width of current peaks. There are three factors that broaden the spectra; the finite source-drain voltage V^{sd}, the temperature β^{-1}, and the contact broadening Δ. In our present calculation, their values are $0.05t$, $0.01t$, and $\sim 0.0005t$, respectively; thus, the V^{sd} factor is relevant. In fact, as seen in Figs. 3.6(a)-3.6(c), every peak has a width of about $0.05t$.

3.3.2 Electric field effects

We then study how the current spectra change when a small external electric field is applied to the Kagomé-lattice chain. Two cases are considered: the uniform electric field along the chain and that perpendicular to the chain, i.e., the x

-0.5   0.5
Wave function amplitude
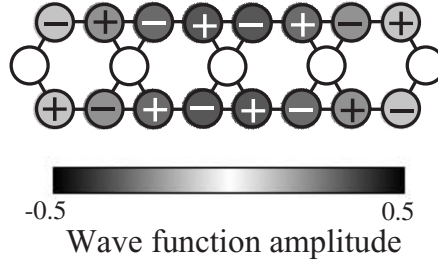
Figure 3.7: *Ungerade* eigenfunction of four-plaquette Kagomé-lattice chain. $+$ and $-$ in circles are the signs of wave function amplitudes, while the tone represents the magnitude of amplitude.
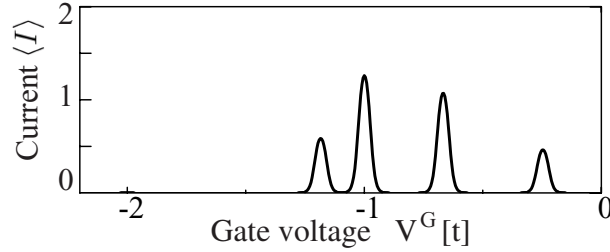
Figure 3.8: Calculated current vs gate-voltage characteristics of four-plaquette Kagomé-lattice chain when electric field is applied along chain, *i.e.*, along x direction, with $V^{\mathrm{x}} = 0.05t$. The unit of current is $10^{-4}|t|^2 e/h$.

and y directions in Fig. 3.3, respectively. In the former case, we assume that the on-site potential is given by

$$V_i^{\mathrm{E}} = V^x(2Ma - x_i)/(2Ma), \qquad (3.36)$$

where x_i is the x coordinate of the i-th site in a chain and V^x represents the electric-field magnitude. Figure 3.8 shows the calculated current spectra of the four-plaquette Kagomé-lattice chain as a function of gate voltage, where the value of $V^x = 0.05t$ is adopted. It is seen that the overall spectra are similar to those in the case with no electric field shown in Fig. 3.6(b). We found that this result does not change when the V^x value is changed.

In the case of the electric field along the y direction, we assume the on-site potential as

$$V_i^{\mathrm{E}} = V^y y_i/(\sqrt{3}a), \qquad (3.37)$$

where y_i is the y coordinate of the i-th site in a chain and V^y represents the electric-field magnitude. Figures 3.9(a)-3.9(c) show the calculated current vs gate-voltage spectra for the two-, four-, and ten-plaquette Kagomé-lattice chains, respectively, where $V^y = 0.05t$ is employed. Since the electric field is small, the currents through the normal-band channels have almost the same position and spectral magnitude as those in Figs. 3.6(a)-3.6(c). On the other hand, it is noteworthy that a large current peak appears at $V^{\mathrm{G}} = -2t$, *i.e.*, at the position of the flat-band channel.
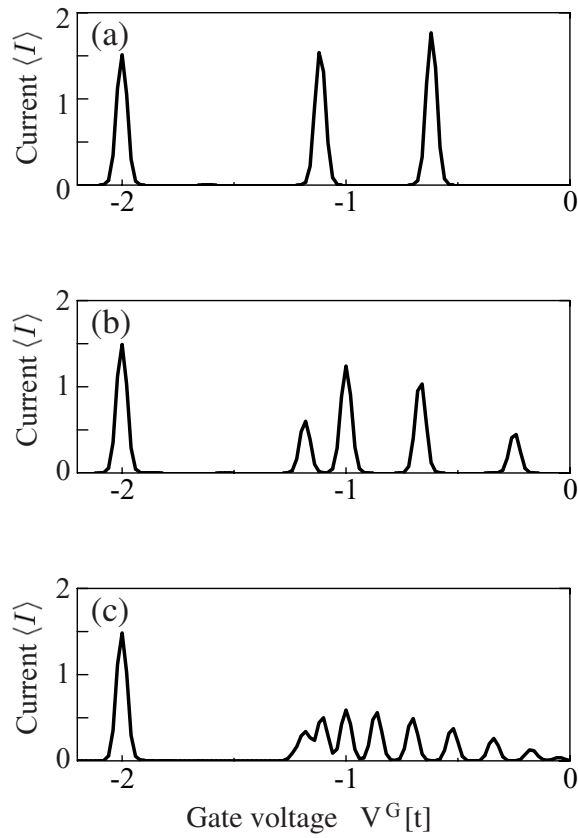
Figure 3.9: Calculated current vs gate-voltage characteristics of (a) two-, (b) four-, and (c) ten-plaquette Kagomé-lattice chains when electric field is applied perpendicular to chain, i.e., along y direction, with $V^y = 0.05t$. The unit of current is $10^{-4}|t|^2 e/h$.

The application of the external small electric fields removes the energy degeneracy of the flat-band states in the Kagomé lattices. To understand what changes occur for these states, we investigate their wave functions. In the case of the four-plaquette Kagomé-lattice chain, for example, fourfold degenerate flat-band states change to have different energies. Figures 3.10(a)-3.10(d) show the wave functions of these states in the case corresponding to Fig. 3.8. In these figures, $+$ and $-$ are the signs of the wave functions, while the tone represents their amplitude. It is seen that all these states are localized around one of the plaquettes in the Kagomé-lattice chain. This is because each plaquette has a different on-site energy when the electric field is along the chain direction. In fact, four eigenstates have energies in the order from (a) to (d) in Fig. 3.10. Reflecting such a localized nature of the wave functions, the electron transport probability of these channels is considerably small. Therefore, one cannot see current peaks around the flat-band channel in Fig. 3.8.

When the electric field is applied perpendicular to the chain, fourfold-degenerate eigenstates change to have different energies and have wave functions shown in Figs. 3.11(a)-3.11(d). It is seen that all these states are extended over the Kagomé-lattice chain. Thus, several current channels originating from these states are opened and induce the sudden appearance of large current peaks at $V^{\mathrm{G}} = -2t$, as shown in Fig. 3.9(b). On the basis of these results, one can observe the multiple energy degeneracy of the flat-band states by applying the electric field perpendicular to the chain. Noting that the flat-band states have both localized and itinerant characteristics, one can say that the electric field along the chain direction promotes the emergence of the localized characteristic of these states and thus induces no current. On the other hand, the electric field perpendicular to the chain promotes the emergence of the itinerant characteristic and produces the large current.

3.3.3   Current spectral variation

We note in Figs. 3.9(a)-3.9(c) that the current peaks through the flat-band channel have almost the same magnitude, which is independent of the size of the Kagome-lattice chain [40]. Moreover, although the application of the electric field removes the energy degeneracy of the flat-band states to produce several different energies, one can see only a single current peak around the flat-band channel. To understand these features, we study how the current spectra vary as the magnitude of the electric field, V^{y}, changes.

Figure 3.12 shows the current spectra of the four-plaquette Kagomé-lattice chain around the flat-band channel for various values of V^{y}. The spectral variation is categorized into three regimes depending on the magnitude of the electric field. In regime I ($V^{y} < 0.05t$), one can see a single peak in the flat-band channel at around $V^{\mathrm{G}} = -2t$. With increasing V^{y} from zero to $0.05t$, this peak slightly shifts its every position and sharply increases its magnitude from zero to a maximum value. In regime II ($0.05t < V^{y} < 0.1t$), the peak gradually shifts its energy position as V^{y} increases but maintains almost the same maximum magnitude, which dose not depend on the V^{y} values. Then, in regime III ($0.1t < V^{y}$), the peak

Figure 3.10: Eigenfunctions of four-plaquette Kagomé-lattice chain correspond-ing to flat-band states, when electric field is applied along chain, *i.e.*, along x direction. $+$ and $-$ in circles are the signs of wave functions, while the tone represents their amplitude.
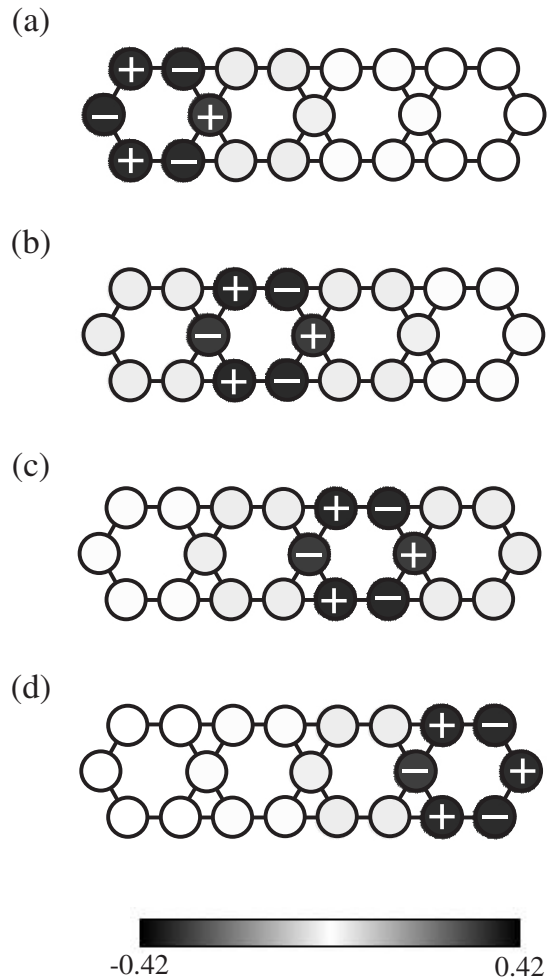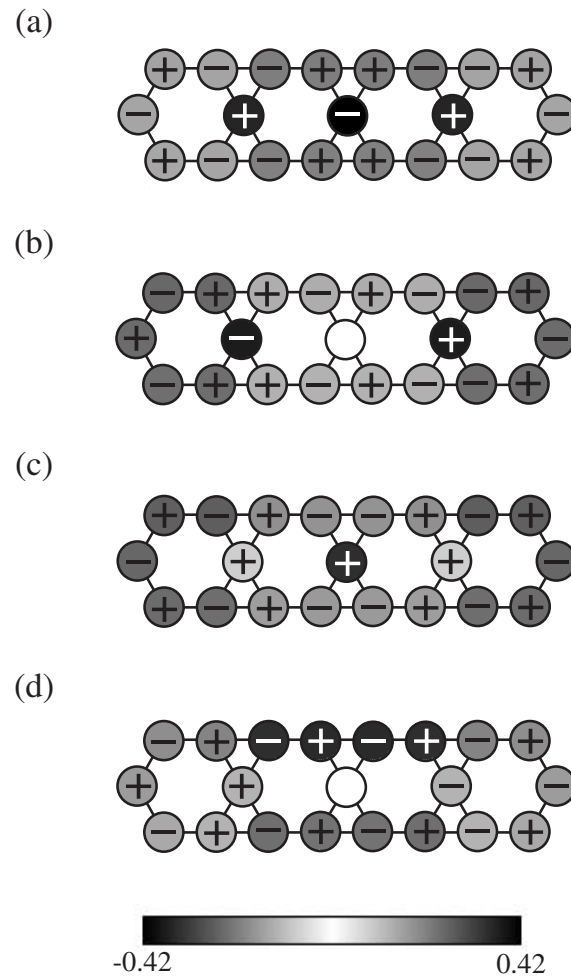
Figure 3.11: Eigenfunctions of four-plaquette Kagomé-lattice chain correspond-ing to flat-band states, when electric field is applied perpendicular to chain, *i.e.*, along y direction.
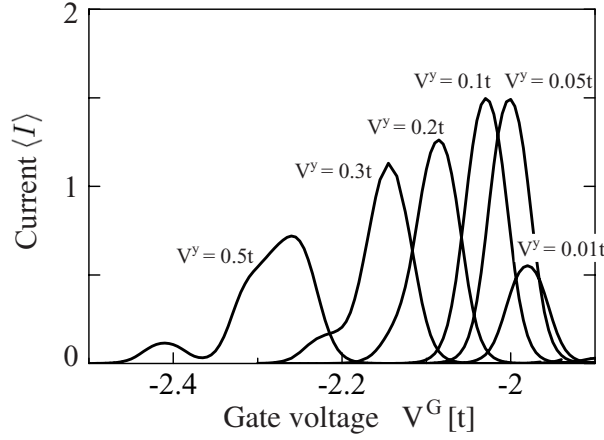
Figure 3.12: Calculated current vs gate-voltage characteristics of four-plaquette Kagomé-lattice chain around flat-band channel, for various values of electric field along y direction. The unit of current is $10^{-4}|t|^2 e/h$.

shifts its energy position and broadens to split into several peaks with increasing V^y. The mechanism of these variations is explained as follows.

We first consider regime III. In this regime, since the electric field is large, the energy degeneracy of flat-band states is broken and each electronic state exists separately in energy. Thus, one can use the Green function in Eq. (3.29) to describe the current channel corresponding to each electronic state. Moreover, if we denote the representative energy separation between such states as δE^α, δE^α increases with increasing V^y and becomes larger than the difference in chemical potential between the left and right electrodes, such as $\delta E^\alpha > \mu^L - \mu^R$. This situation is schematically displayed in Fig. 3.13(a), where only a single channel is scanned at each gate-voltage value and we have many peaks in the current spectra. In this sense, we can say that the flat-band channels in regime III behave like the normal-state channels.

When we decrease the electric field and enter regime II, the energy separation decreases such as $\mu^L - \mu^R > \delta E^\alpha$, which is shown in Fig. 3.13(b). In this case, all the flat-band channels are scanned simultaneously at a single gate-voltage value, and the sum of these channels produces a large single current peak. This is why the peak has almost the same magnitude in regime II, which does not depend on the V^y values. On the other hand, since the electronic states are extended over the entire system as in Fig. 3.11, the current magnitude originating from a single channel is proportional to the inverse of the number of sites, $N(= 5 \times M + 1)$, as described by Eq. (3.35). However, M channels simultaneously contribute to the current spectra. Thus, the current peak has also a constant magnitude, which is independent of the system size. On the basis of these results, we can observe the multiple energy freedom of flat-band states as a large single current peak in regime II.

When we further decrease the electric field and enter regime I, the energy separation becomes smaller than the broadening of the respective energy level as

$\Delta > \delta E^\alpha$. This situation is shown in Fig. 3.13(c). In this regime, in stead of Eq. (3.29), one can approximate the Green function as

$$G^r_{1N}(E \sim E_{\text{flat}}) \simeq \frac{\chi^1_1 \chi^1_N + \chi^2_1 \chi^2_N + \cdots + \chi^M_1 \chi^M_N}{E - E_{\text{flat}} + i\Delta}, \qquad (3.38)$$

where E_{flat} represents the average energy of the flat-band states. As seen in Figs. 3.11(a)-3.11(d), the sign of the product of wave function amplitude, $\chi^\alpha_1 \chi^\alpha_N$, of the α-th eigenstate is opposite to those of the nearest $(\alpha - 1)$- and $(\alpha + 1)$-th states. This sign alternation reflects the number of nodal planes in the wave function of the eigenstate along the chain direction. Therefore, the sum in the numerator cancels out one another among the flat-band states and produces a small current peak. Figure 3.14(a) shows the calculated imaginary parts of the $G^a_{1N}(E)$ at $V^y = 0.01t$ in regime I. For the comparison, the Green function at $V^y = 0.05t$ in regime II is shown in Fig. 3.14(b). The positive and negative peaks observed in Fig. 3.14(a) overlap with each other and decrease the magnitude. Such cancellation occurs apparently due to the quantum interference between the wave functions of flat-band states. Thus, we can say that the quantum interference dominates regime I and promotes the abrupt variation in current-peak magnitude.

Here, we reconsider why the current is zero for the flat-band channel when there is no electric field applied, using Eq. (3.38). In the localized picture of the flat-band states, since the electronic state is localized in a certain plaquette, each product of two different sites, $\chi^\alpha_1 \chi^\alpha_N$, is zero and produces no current. On the other hand, in the itinerant picture of the flat-band states, such products alternatively have different signs and their sums cancel one another in the numerator of Eq. (3.38) to produce no current.

Finally, the conditions for observing the large current are discussed. To scan all the flat-band channels, as discussed above, the energy separation, which occurs due to the application of an electric field, must be smaller than the difference in chemical potential between the left and right electrodes; thus, $\mu^L - \mu^R > \delta E^\alpha$ is required. On the other hand, to prevent the quantum interference between flat-band states, such separation should be larger than the broadening of the respective energy level; thus, $\delta E^\alpha > \Delta$ is required. In the regime of a moderate electric field satisfying both conditions, one can observe a large current originating from the large energy freedom of flat-band states.

3.3.4   Degeneracy breaking

We have shown in previous subsections that the application of an electric field removes the energy degeneracy of flat-band states. In particular, the localized characteristic emerges in wave functions when the electric field is applied along the chain direction, while the itinerant characteristic emerges when the electric field is applied perpendicular to the chain direction. To understand why such different characteristics appear depending on the direction of the electric field, we simultaneously apply the electric fields of both directions to the Kagomé-lattice chain and study how the current peak through the flat-band channel changes.
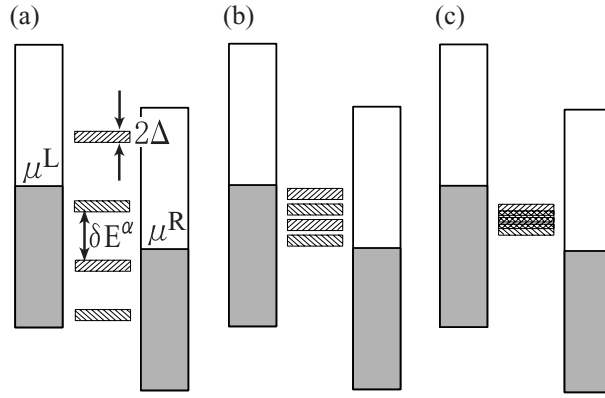
Figure 3.13: Schematic energy diagrams representing relative positions of flat-band states and two electrodes. Bars in the center denote the energy levels of flat-band states. These states have the energy separation of δE^α and the energy broadening of Δ. (a) Regime III: $\delta E^\alpha > (\mu^L - \mu^R) > \Delta$; (b) regime II: $(\mu^L - \mu^R) > \delta E^\alpha > \Delta$; and (c) regime I: $(\mu^L - \mu^R) > \Delta > \delta E^\alpha$.
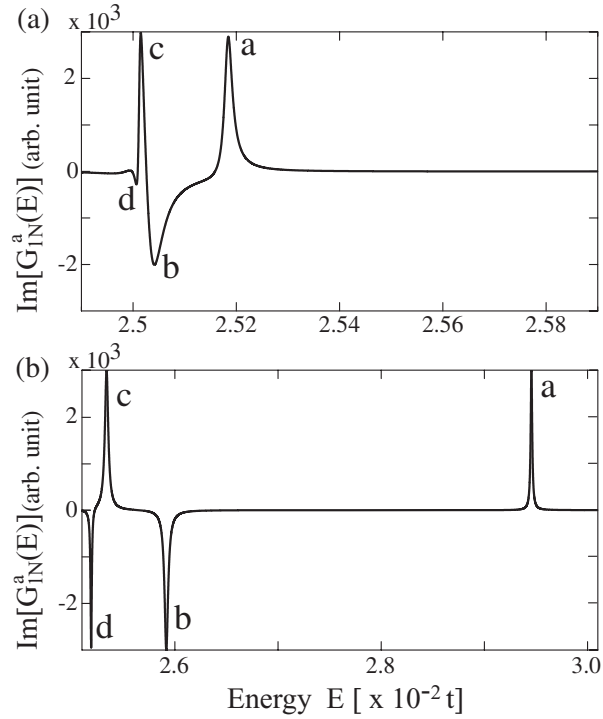
Figure 3.14: Calculated imaginary parts of the Green function G_{1N}^a at (a) $V^y = 0.01t$ and (b) $V^y = 0.05t$. The peaks numbered from "a" to "d" corresponding to the flat-band channels shown in Figs. 3.11(a) to 3.11(d), respectively.
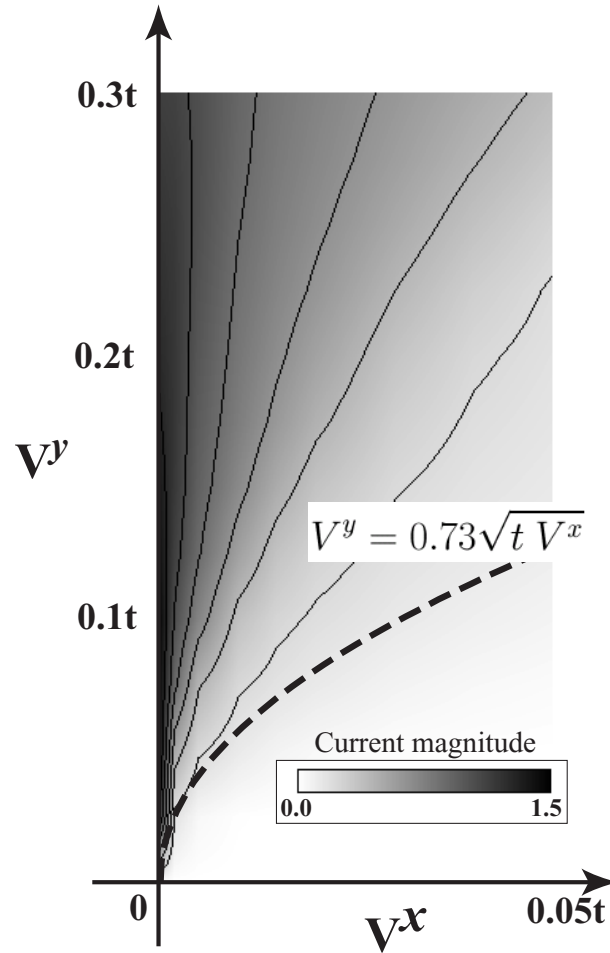
Figure 3.15: Contour-map plot of current-peak magnitude of flat-band channel for four-plaquette Kagomé-lattice chain, as a function of two-dimensional components of electric field, V^x and V^y. The current shown has a unit of $10^{-4}|t|^2 e/h$.
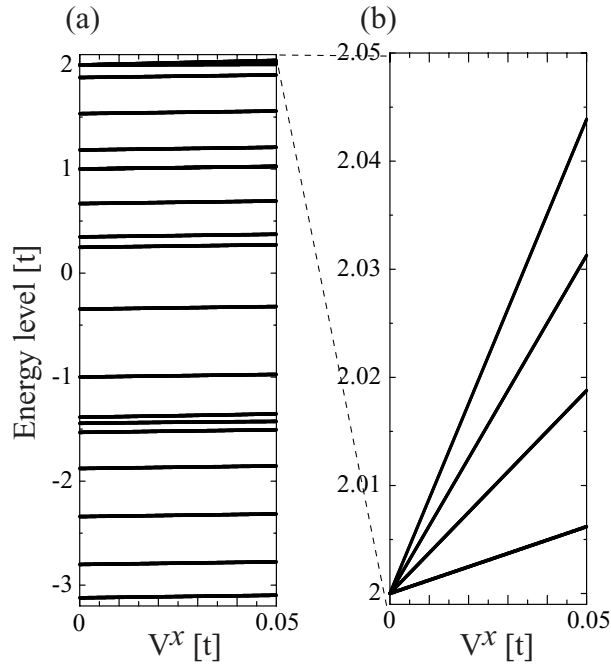
Figure 3.16: Energy levels of four-plaquette Kagomé-lattice chain as a function of electric field, V^x. (a) All energy-level spectra and (b) extended picture around flat-band energy levels.

Figure 3.15 shows the contour-map plot of the current-peak magnitude of the flat-band channel for the four-plaquette Kagomé-lattice chain, as a function of the two-dimensional components of the electric field, V^x and V^y. One notes that the current can be obtained roughly in the region of $V^y > 0.73\sqrt{t\,V^x}$. This feature reflects the difference of energy-degeneracy breaking between two directions as follows. When a small electric field is applied along the chain, the degenerate flat-band states couple with each other to become localized states having different energies, as shown in Fig. 3.10. This recoupling is caused by the first-order perturbation by the electric field, V^x as shown in Figs. 3.16; thus, the energy separation between the states is proportional to V^x.

On the other hand, when a small electric field is applied perpendicular to the chain, the degenerate flat-band states couple with each other to become extended states, as shown in Fig. 3.11. In this case, however, such recoupling does not break the energy degeneracy. This is because the flat-band states in the Kagomé-lattice chain have a *gerade* symmetry with respect to the reflection-symmetry operation along the y direction and thus have no interactions with each other when the electric field is applied along the y direction. The breaking of energy degeneracy is realized by the second-order perturbation between the flat-band state and the normal-band states. This feature can be confirmed by examining the energy level variation by changing the V^y value, which is shown in Figs. 3.17(a) and 3.17(b). It is apparent that the energy separation is proportional to the square of the electric field, V^y. Considering the difference in perturbation between two directions,
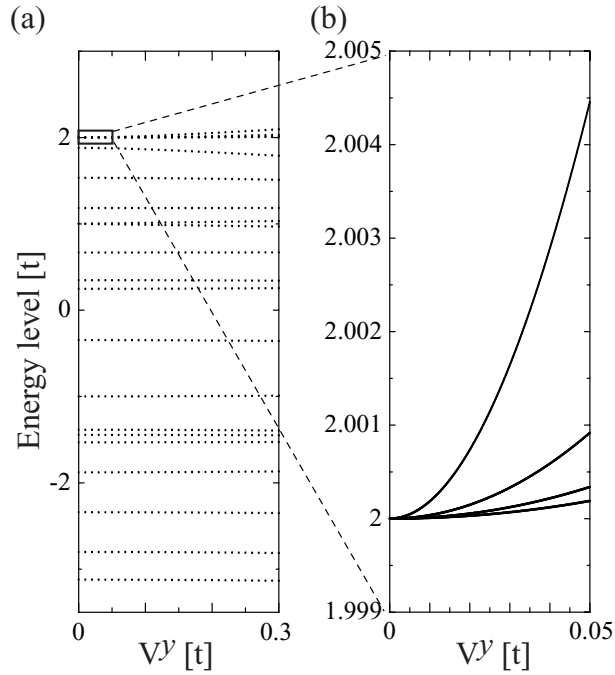
Figure 3.17: Energy levels of four-plaquette Kagomé-lattice chain as a function of electric field, V^y. (a) All energy-level spectra and (b) extended picture around flat-band energy levels.

we can expect that the large current is dominated by the itinerant characteristic of flat-band states in the region of $V^y > \sqrt{t\,V^x}$, which well explains the feature in Fig. 3.15.

Finally, we briefly comment on the observation of the flat-band-channel current in experiments. As seen in Fig. 3.15, the flat-band channel suddenly opens when a small electric field is applied perpendicular to the Kagomé-lattice chain. Thus, the simplest method of confirming the present results is to apply an electric field and observe the sudden appearance of a current peak. Moreover, we expect that the present anisotropic feature of electron transport may be used to produce unique devices by fabricating the Kagomé-lattice network systems.

3.4   Conclusions

Electron transport properties are investigated in the Kagomé-lattice-chain systems, using the simple tight-binding model and nonequilibrium Green function method. We found that the current through the flat-band channel is sensitive to the direction of the applied electric field; a large current is observed to flow along the chain when the electric field is applied perpendicular to the chain, while no current is observed to flow along the chain when the electric field is applied along the chain. By analyzing how the flat-band degeneracy is broken, this strange anisotropy is shown to originate from the unique feature of the flat-band states, that is, they have both itinerant and localized characteristics. Moreover, we found that the transport characteristic changes from the quantum interference to noninterference regimes with increasing electric field, and the current magnitude becomes nearly independent of the size of the Kagomé-lattice chain at the boundary of both regimes. The conditions for observing the flat-band current were also determined.

3.5   Appendix I; Nonequilibrium Green function method

In this section, we show how to calculate the electronic current by using the nonequilibrium Green function method. Caroli and coworkers treated the electronic current using the following way [38]. At initial time $t = -\infty$, the two electrodes and the Kagomé-lattice chain are separated each other. In other words, the electrode $\xi \ (= L, R)$ and the chain C are equilibrium state with chemical potential μ^ξ and μ^C, respectively. Then, we connect the electrodes and the chain at $t = t_0$, and physical quantity is observed at time $t(> t_0)$. One of the advantages of their method is that the three different chemical potentials μ^L, μ^R, and μ^C can be introduced through the initial condition.

3.5.1   Schrödinger, Heisenberg and interaction pictures

Schrödinger picture

For the later discussions, we summarize the Schrödinger, Heisenberg and interaction pictures for following Hamiltonian [41],

$$
\begin{aligned}
\hat{\mathcal{H}}(t) &= \hat{\mathcal{H}}^L + \hat{\mathcal{H}}^C + \hat{\mathcal{H}}^R + \hat{\mathcal{W}}(t) \\
&= \hat{\mathcal{H}}_0 + \hat{\mathcal{W}}(t),
\end{aligned}
\tag{3.39}
$$

where $\hat{\mathcal{H}}_0 \equiv \hat{\mathcal{H}}^L + \hat{\mathcal{H}}^C + \hat{\mathcal{H}}^R$ and

$$
\hat{\mathcal{W}}(t) \equiv \hat{\mathcal{W}}\,\theta(t - t_0) \equiv
\begin{cases}
\hat{\mathcal{W}} & \text{for } t > t_0, \\
0 & \text{for } t \leq t_0.
\end{cases}
\tag{3.40}
$$

Each Hamiltonian has been already defined in Eqs. (3.1)-(3.4). In the Schrödinger picture, well-known equation of motion

$$
i\hbar \frac{\partial |\psi(t)\rangle}{\partial t} = \hat{\mathcal{H}}(t)|\psi(t)\rangle,
\tag{3.41}
$$

is satisfied. Here, $|\psi(t)\rangle$ is the state vector. We write the operator in the Schödinger picture as $\hat{\mathcal{O}}$. The expectation value of the operator $\langle \mathcal{O}(t) \rangle$ in the state $|\psi(t)\rangle$ is obtained by $\langle \psi(t)|\hat{\mathcal{O}}|\psi(t)\rangle$. Let consider the time-evolution operator $\hat{S}(t, t_0)$ in the Schrödinger picture, which satisfies the relation $(t > t_0)$,

$$
|\psi(t)\rangle = \hat{S}(t, t_0)|\psi(t_0)\rangle.
\tag{3.42}
$$

To calculate the nonequilibrium state, we need the $|\psi(t)\rangle$. However, we know only the initial equilibrium state $|\psi(t_0)\rangle$. Thus, we must calculate the time-evolution operator $\hat{S}(t, t_0)$. Inserting Eq. (3.42) to Eq. (3.41), we obtain

$$
i\hbar \frac{\partial \hat{S}(t, t_0)}{\partial t} = \hat{\mathcal{H}}(t)\hat{S}(t, t_0).
\tag{3.43}
$$

Heisenberg picture

Using the time-evolution operator, we define the operator $\hat{\mathcal{O}}_H(t)$ and the state vector $|\psi_H\rangle$ in the Heisenberg picture as

$$\hat{\mathcal{O}}_H(t) = \hat{S}^\dagger(t, t_0)\hat{\mathcal{O}}\hat{S}(t, t_0), \tag{3.44}$$

and

$$|\psi_H\rangle = |\psi(t_0)\rangle, \tag{3.45}$$

respectively. The expectation value is obtained as

$$\langle \mathcal{O}(t)\rangle = \langle \psi_H|\hat{\mathcal{O}}_H(t)|\psi_H\rangle. \tag{3.46}$$

Using Eq. (3.42), we can confirm that the expectation value in the Schrödinger picture is equal to that in the Heisenberg picture. The operator $\hat{\mathcal{O}}_H(t)$ satisfies what we call Heisenberg equation of motion,

$$\begin{aligned}
i\hbar\frac{d\hat{\mathcal{O}}_H(t)}{dt} &= i\hbar\frac{d(\hat{S}^\dagger(t, t_0)\hat{\mathcal{O}}\hat{S}(t, t_0))}{dt} \\
&= i\hbar\frac{d\hat{S}^\dagger(t, t_0)}{dt}\hat{\mathcal{O}}\hat{S}(t, t_0) + i\hbar\hat{S}^\dagger(t, t_0)\hat{\mathcal{O}}\frac{\hat{S}(t, t_0)}{dt} \\
&= -\hat{S}^\dagger(t, t_0)\hat{\mathcal{H}}(t)\hat{\mathcal{O}}\hat{S}(t, t_0) + \hat{S}^\dagger(t, t_0)\hat{\mathcal{O}}\hat{\mathcal{H}}(t)\hat{S}(t, t_0) \\
&= -\hat{S}^\dagger(t, t_0)\hat{\mathcal{H}}(t)\hat{S}(t, t_0)\hat{S}^\dagger(t, t_0)\hat{\mathcal{O}}\hat{S}(t, t_0) \\
&\quad + \hat{S}^\dagger(t, t_0)\hat{\mathcal{O}}\hat{S}(t, t_0)\hat{S}^\dagger(t, t_0)\hat{\mathcal{H}}(t)\hat{S}(t, t_0) \\
&= \left[\hat{\mathcal{O}}_H(t), \hat{\mathcal{H}}_H(t)\right]
\end{aligned} \tag{3.47}$$

interaction picture

The operator in the interaction picture $\hat{\mathcal{O}}_I(t)$ is related to that in the Schrödinger picture as a unitary transformation

$$\hat{\mathcal{O}}_I(t) = e^{i\frac{\hat{\mathcal{H}}_0}{\hbar}(t-t_0)}\hat{\mathcal{O}}e^{-i\frac{\hat{\mathcal{H}}_0}{\hbar}(t-t_0)}. \tag{3.48}$$

On the other hand, the relation between the interaction picture and the Heisenberg picture satisfies the following equation,

$$\hat{\mathcal{O}}_H(t) = \hat{S}_I^\dagger(t, t_0)\hat{\mathcal{O}}_I(t)\hat{S}_I(t, t_0), \tag{3.49}$$

where we define the time-evolution operator $\hat{S}_I(t, t_0)$ in the interaction picture,

$$\hat{S}_I(t, t_0) = e^{i\frac{\hat{\mathcal{H}}_0}{\hbar}(t-t_0)}\hat{S}(t, t_0). \tag{3.50}$$

The state vector in the interaction picture is defined as

$$|\psi_I(t)\rangle = e^{i\frac{\hat{\mathcal{H}}_0}{\hbar}(t-t_0)}|\psi(t)\rangle, \tag{3.51}$$

because the expectation value has to be the same in any pictures. In other words, the expectation value can be written as follows,

$$\langle \mathcal{O}(t) \rangle = \langle \psi_I(t) | \hat{\mathcal{O}}_I(t) | \psi_I(t) \rangle = \langle \psi(t) | \hat{\mathcal{O}} | \psi(t) \rangle. \tag{3.52}$$

We note that $|\psi(t_0)\rangle = |\psi_H\rangle = |\psi_I(t_0)\rangle$. Using Eq. (3.42), we obtain the time-evolution of the state vector in the interaction picture,

$$
\begin{aligned}
|\psi_I(t)\rangle &= e^{i\frac{\hat{\mathcal{H}}_0}{\hbar}(t-t_0)} |\psi(t)\rangle \\
&= e^{i\frac{\hat{\mathcal{H}}_0}{\hbar}(t-t_0)} \hat{S}(t,t_0) |\psi(t_0)\rangle \\
&= e^{i\frac{\hat{\mathcal{H}}_0}{\hbar}(t-t_0)} \hat{S}(t,t_0) |\psi_I(t_0)\rangle \\
&= \hat{S}_I(t,t_0) |\psi_I(t_0)\rangle.
\end{aligned}
\tag{3.53}
$$

For the practical applications it is quite important to derive an explicit formula of $\hat{S}_I(t,t_0)$ in terms of $\hat{\mathcal{W}}_I(t)$. Let first derive an equation of motion for $\hat{S}_I(t,t_0)$ from Eq. (3.43) and Eq. (3.50),

$$
\begin{aligned}
i\hbar \frac{\partial \hat{S}_I(t,t_0)}{\partial t} &= i\hbar \Big[i\frac{\hat{\mathcal{H}}_0}{\hbar} e^{i\frac{\hat{\mathcal{H}}_0}{\hbar}(t-t_0)} \hat{S}(t,t_0) + e^{i\frac{\hat{\mathcal{H}}_0}{\hbar}(t-t_0)} \frac{\partial \hat{S}(t,t_0)}{\partial t} \Big] \tag{3.54} \\
&= -\hat{\mathcal{H}}_0 e^{i\frac{\hat{\mathcal{H}}_0}{\hbar}(t-t_0)} \hat{S}(t,t_0) + e^{i\frac{\hat{\mathcal{H}}_0}{\hbar}(t-t_0)} \hat{\mathcal{H}}(t) \hat{S}(t,t_0) \tag{3.55} \\
&= e^{i\frac{\hat{\mathcal{H}}_0}{\hbar}(t-t_0)} \hat{\mathcal{W}}(t) \hat{S}(t,t_0) \tag{3.56} \\
&= e^{i\frac{\hat{\mathcal{H}}_0}{\hbar}(t-t_0)} \hat{\mathcal{W}}(t) e^{-i\frac{\hat{\mathcal{H}}_0}{\hbar}(t-t_0)} e^{i\frac{\hat{\mathcal{H}}_0}{\hbar}(t-t_0)} \hat{S}(t,t_0) \tag{3.57} \\
&= \hat{\mathcal{W}}_I(t) \hat{S}_I(t,t_0). \tag{3.58}
\end{aligned}
$$

We now convert it to an integral equation by integrating from t_0 to t and taking the initial condition $\hat{S}(t_0,t_0) = 1$,

$$\hat{S}_I(t,t_0) = 1 + \frac{1}{i\hbar} \int_{t_0}^{t} d\tau \, \hat{\mathcal{W}}_I(\tau) \hat{S}_I(\tau,t_0). \tag{3.59}$$

Successive iterative substitution yields

$$
\begin{aligned}
\hat{S}_I(t,t_0) &= 1 + \frac{1}{i\hbar} \int_{t_0}^{t} d\tau_1 \hat{\mathcal{W}}_I(\tau) + \frac{1}{2!} \Big(\frac{1}{i\hbar}\Big)^2 \int_{t_0}^{t} d\tau_1 \int_{t_0}^{t} d\tau_2 \mathrm{T}[\hat{\mathcal{W}}_I(\tau_1) \hat{\mathcal{W}}_I(\tau_2)] + \cdots \\
&= \sum_{n=0}^{+\infty} \frac{1}{n!} \Big(\frac{-i}{\hbar}\Big)^n \int_{t'}^{t} d\tau_1 \cdots \int_{t'}^{t} d\tau_n \, \mathrm{T} [\hat{\mathcal{W}}_I(\tau_1) \cdots \hat{\mathcal{W}}_I(\tau_n)] \\
&= \mathrm{T} \exp \Big[-\frac{i}{\hbar} \int_{t_0}^{t} d\tau \hat{\mathcal{W}}_I(\tau) \Big],
\end{aligned}
\tag{3.60}
$$

where T is the time-ordering operator. The Hermitian conjugate of $\hat{S}_I(t,t_0)$ is written as

$$\hat{S}_I^\dagger(t,t_0) = \hat{S}_I(t_0,t) = \tilde{\mathrm{T}} \exp \Big[\frac{i}{\hbar} \int_{t'}^{t} d\tau \hat{\mathcal{W}}_I(\tau) \Big], \tag{3.61}$$

where $\tilde{\mathrm{T}}$ represents the $\tilde{\mathrm{T}}$-product operator, which arranges the time-dependent operators in inverse chronological order.

3.5.2 The expectation value in the mixed state

So far we have considered the expectation value in the pure state. In order to calculate the expectation value in the mixed state, the statistical (density) operator $\hat{\rho}(t)$ is introduced,

$$\hat{\rho}(t) = \sum_n P_n |\psi_n(t)\rangle\langle\psi_n(t)|, \tag{3.62}$$

where P_n is the statistical probability that the system is to be in state $|\psi_n(t)\rangle$. We can relate $\hat{\rho}(t)$ to initial density operator $\hat{\rho}(t_0)$ in terms of $\hat{S}$,

$$\hat{\rho}(t) = \sum_n P_n \hat{S}(t,t_0)|\psi_n(t_0)\rangle\langle\psi_n(t_0)|\hat{S}^\dagger(t,t_0) = \hat{S}(t,t_0)\hat{\rho}(t_0)\hat{S}^\dagger(t,t_0). \tag{3.63}$$

By use of $\hat{\rho}(t)$ we can calculate the expectation value $\langle\mathcal{O}(t)\rangle$ in the statistical ensemble,

$$\langle\mathcal{O}(t)\rangle \equiv \sum_n P_n \langle\psi_n(t)|\hat{\mathcal{O}}(t)|\psi_n(t)\rangle \tag{3.64}$$

$$= \text{Tr}[\hat{\rho}(t)\hat{\mathcal{O}}]$$

$$= \text{Tr}[\hat{S}(t,t_0)\hat{\rho}(t_0)\hat{S}^\dagger(t,t_0)\hat{\mathcal{O}}]$$

$$= \text{Tr}[\hat{\rho}(t_0)\hat{S}^\dagger(t,t_0)\hat{\mathcal{O}}\hat{S}(t,t_0)]$$

$$= \text{Tr}[\hat{\rho}(t_0)\hat{\mathcal{O}}_H(t)] \tag{3.65}$$

$$= \langle\hat{\mathcal{O}}_H(t)\rangle_0, \tag{3.66}$$

where $\text{Tr}[\hat{X}\hat{Y}] = \text{Tr}[\hat{Y}\hat{X}]$ is applied and $\langle\cdots\rangle_0 \equiv \text{Tr}[\hat{\rho}(t_0)\cdots]$. For the practical purpose, it is convenient to write it in the interaction picture with aid of Eq. (3.49),

$$\langle\mathcal{O}(t)\rangle = \langle\hat{S}_I^\dagger(t,t_0)\hat{\mathcal{O}}_I(t)\hat{S}_I(t,t_0)\rangle_0 \tag{3.67}$$

$$= \langle(\hat{S}_I(t,+\infty)\hat{S}_I(+\infty,t_0))^\dagger\hat{\mathcal{O}}_I(t)\hat{S}_I(t,t_0)\rangle_0 \tag{3.68}$$

$$= \langle\hat{S}_I(t_0,+\infty)\hat{S}_I(+\infty,t)\hat{\mathcal{O}}_I(t)\hat{S}_I(t,t_0)\rangle_0, \tag{3.69}$$

where $\hat{S}_I(t,t_0) = \hat{S}_I(t,+\infty)\hat{S}_I(+\infty,t_0)$ is used.

3.5.3 Path-ordered Green function

The equation (3.69) shows that the initial equilibrium state develops to the nonequilibrium state under the operator $\hat{S}_I(t,t_0)$, and then the physical quantity $\mathcal{O}(t)$ is observed at time t, after that, the state develops from time t to time $+\infty$. Finally, the state returns from time $+\infty$ to time t_0 under the $\hat{S}_I(t_0,+\infty)$. Thus, the time-evolution path consists of the chronological-order path (- branch) and the inverse-chronological-order path (+ branch). This path is called as the time loop. The time loop is shown in Fig. 3.18.
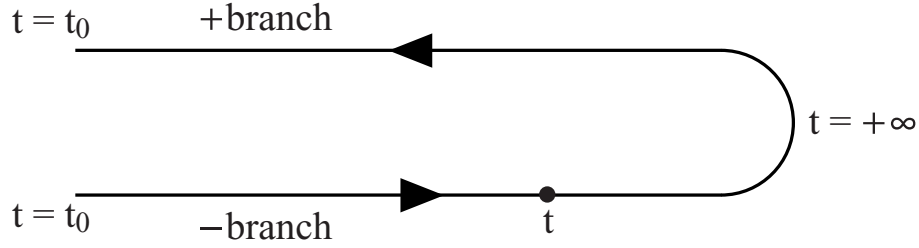
Figure 3.18: Schematic picture of the time loop. the time loop consists of the chronological-order path (- branch) and the inverse-chronological-order path (+ branch).

When we calculate Eq. (3.69) concretely, we need to expand the time-evolution operators $\hat{S}_I$ by using Eq. (3.60) and Eq. (3.61).

$$\langle \mathcal{O}(t) \rangle = \sum_{n=0}^{+\infty} \sum_{m=0}^{+\infty} \frac{1}{n!} \left(\frac{i}{\hbar} \right)^n \frac{1}{m!} \left(\frac{-i}{\hbar} \right)^m \int_{t_0}^{+\infty} d\tau_1' \cdots \int_{t_0}^{+\infty} d\tau_n' \int_{t_0}^{+\infty} d\tau_1 \cdots \int_{t_0}^{+\infty} d\tau_m$$

$$\langle \tilde{T}[\hat{\mathcal{W}}_I(\tau_1') \cdots \hat{\mathcal{W}}_I(\tau_n')] \, T[\hat{\mathcal{W}}_I(\tau_1) \cdots \hat{\mathcal{W}}_I(\tau_m) \hat{\mathcal{O}}_I(t)] \rangle_0. \tag{3.70}$$

We can obtain the statistical averages $\langle \mathcal{O}(t) \rangle$ by solving the Eq. (3.70). For example, when the operator $\hat{\mathcal{O}}$ is the electron number at i-th site, we set $\hat{\mathcal{O}}$ as $\hat{c}_i^\dagger \hat{c}_i$. The statistical average $\langle \cdots \rangle_0$ in Eq. (3.70) is resolved into the products of the pair-correlation functions such as $\langle \hat{c}_{Ii}^\dagger(\tau_1) \hat{c}_{Ij}(\tau_2) \rangle_0$ when we apply the Wick's theorem to the statistical average. The pair-correlation functions are classified into four types dependent on whether the operator is in the $+$ branch or in the $-$ branch of the time loop. The four nonequilibrium Green functions are defined as follows,

$$i\hbar \, G_{ij}^{--}(t_1, t_2) \equiv \langle T[\hat{c}_{Hi}(t_1) \hat{c}_{Hj}^\dagger(t_2)] \rangle, \tag{3.71}$$

$$i\hbar \, G_{ij}^{++}(t_1, t_2) \equiv \langle \tilde{T}[\hat{c}_{Hi}(t_1) \hat{c}_{Hj}^\dagger(t_2)] \rangle, \tag{3.72}$$

$$i\hbar \, G_{ij}^{+-}(t_1, t_2) \equiv \langle \hat{c}_{Hi}(t_1) \hat{c}_{Hj}^\dagger(t_2) \rangle, \tag{3.73}$$

$$i\hbar \, G_{ij}^{-+}(t_1, t_2) \equiv -\langle \hat{c}_{Hj}^\dagger(t_2) \hat{c}_{Hi}(t_1) \rangle. \tag{3.74}$$

Here $\hat{c}_{Hi}$ and $\hat{c}_{Hi}^\dagger$ represent the annihilation and creation operators of electron at i-th site in the Heisenberg picture, respectively. In the case of $G_{ij}^{ss'}(t_1, t_2)$, the operator $\hat{c}_{Hi}(t_1)(\hat{c}_{Hj}^\dagger(t_2))$ is in $s(s')$ branch of the time loop. For convenience, we introduce the retarded Green functions G_{ij}^r and the advanced Green functions G_{ij}^a,

$$i\hbar \, G_{ij}^r(t_1, t_2) \equiv \langle \hat{c}_{Hi}(t_1) \hat{c}_{Hj}^\dagger(t_2) + \hat{c}_{Hj}^\dagger(t_2) \hat{c}_{Hi}(t_1) \rangle \theta(t_1 - t_2), \tag{3.75}$$

$$i\hbar \, G_{ij}^a(t_1, t_2) \equiv -\langle \hat{c}_{Hi}(t_1) \hat{c}_{Hj}^\dagger(t_2) + \hat{c}_{Hj}^\dagger(t_2) \hat{c}_{Hi}(t_1) \rangle \theta(t_2 - t_1). \tag{3.76}$$

We readily have the following useful relations [42]:

$$G_{ij}^{--}(t_1, t_2) + G_{ij}^{++}(t_1, t_2) = G_{ij}^{-+}(t_1, t_2) + G_{ij}^{+-}(t_1, t_2), \qquad (3.77)$$

$$G_{ij}^r(t_1, t_2) = G_{ij}^{--}(t_1, t_2) - G_{ij}^{-+}(t_1, t_2), \qquad (3.78)$$

$$= G_{ij}^{+-}(t_1, t_2) - G_{ij}^{++}(t_1, t_2), \qquad (3.79)$$

$$G_{ij}^a(t_1, t_2) = G_{ij}^{--}(t_1, t_2) - G_{ij}^{+-}(t_1, t_2), \qquad (3.80)$$

$$= G_{ij}^{-+}(t_1, t_2) - G_{ij}^{++}(t_1, t_2), \qquad (3.81)$$

$$G_{ij}^{--}(t_1, t_2) = -(G_{ji}^{++}(t_2, t_1))^*, \qquad (3.82)$$

$$G_{ij}^{-+}(t_1, t_2) = -(G_{ji}^{-+}(t_2, t_1))^*, \qquad (3.83)$$

$$G_{ij}^{+-}(t_1, t_2) = -(G_{ji}^{+-}(t_2, t_1))^*, \qquad (3.84)$$

$$G_{ij}^a(t_1, t_2) = (G_{ji}^r(t_2, t_1))^*, \qquad (3.85)$$

where $(\cdots)^*$ means the complex conjugate.

3.5.4 Dyson equation

Our aim in this subsection is to obtain the equation of motion for the Green functions. First, we differentiate Green functions $G_{ij}^{ss'}(t_1, t_2)$ with respect to the time t_1,

$$
\begin{aligned}
i\hbar\frac{\partial}{\partial t_1}G_{ij}^{--}(t_1, t_2) = &-\sum_m t_{im}G_{mj}^{--}(t_1, t_2) \\
&- t'(t_1)\{\delta_{i0}G_{1j}^{--}(t_1, t_2) + \delta_{i1}G_{0j}^{--}(t_1, t_2)\} \\
&- t'(t_1)\{\delta_{iN}G_{N+1,j}^{--}(t_1, t_2) + \delta_{i,N+1}G_{0j}^{--}(t_1, t_2)\} \\
&+ \delta_{ij}\delta(t_1 - t_2),
\end{aligned}
\qquad (3.86)
$$

$$
\begin{aligned}
i\hbar\frac{\partial}{\partial t_1}G_{ij}^{++}(t_1, t_2) = &-\sum_m t_{im}G_{mj}^{++}(t_1, t_2) \\
&- t'(t_1)\{\delta_{i0}G_{1j}^{++}(t_1, t_2) + \delta_{i1}G_{0j}^{++}(t_1, t_2)\} \\
&- t'(t_1)\{\delta_{iN}G_{N+1,j}^{++}(t_1, t_2) + \delta_{i,N+1}G_{0j}^{++}(t_1, t_2)\} \\
&- \delta_{ij}\delta(t_1 - t_2),
\end{aligned}
\qquad (3.87)
$$

$$
\begin{aligned}
i\hbar\frac{\partial}{\partial t_1}G_{ij}^{-+}(t_1, t_2) = &-\sum_m t_{im}G_{mj}^{-+}(t_1, t_2) \\
&- t'(t_1)\{\delta_{i0}G_{1j}^{-+}(t_1, t_2) + \delta_{i1}G_{0j}^{-+}(t_1, t_2)\} \\
&- t'(t_1)\{\delta_{iN}G_{N+1,j}^{-+}(t_1, t_2) + \delta_{i,N+1}G_{0j}^{-+}(t_1, t_2)\},
\end{aligned}
\qquad (3.88)
$$

$$
\begin{aligned}
i\hbar\frac{\partial}{\partial t_1}G_{ij}^{+-}(t_1, t_2) = &-\sum_m t_{im}G_{mj}^{+-}(t_1, t_2) \\
&- t'(t_1)\{\delta_{i0}G_{1j}^{+-}(t_1, t_2) + \delta_{i1}G_{0j}^{+-}(t_1, t_2)\} \\
&- t'(t_1)\{\delta_{iN}G_{N+1,j}^{+-}(t_1, t_2) + \delta_{i,N+1}G_{0j}^{+-}(t_1, t_2)\},
\end{aligned}
\qquad (3.89)
$$

where we have used the Heisenberg equation,

$$
\begin{aligned}
i\hbar\frac{\partial}{\partial t_1}\hat{c}_{Hi}(t_1) &= [\hat{c}_{Hi}(t_1), \hat{\mathcal{H}}(t_1)] \\
&= -\sum_m t_{im}\hat{c}_{Hm}(t_1) - t'(t_1)(\delta_{i0}\hat{c}_{H1}(t_1) + \delta_{i1}\hat{c}_{H0}(t_1)) \\
&\quad - t'(t_1)(\delta_{iN}\hat{c}_{HN+1}(t_1) + \delta_{i,N+1}\hat{c}_{HN}(t_1)).
\end{aligned}
\tag{3.90}
$$

Here, we define $t'(t)$ as $t' \cdot \theta(t-t_0)$. If the electrodes are connected to the Kagomé-lattice chain at $t_0 = -\infty$, we can suppose that the joint system has reached the steady state at any time t. Under the steady state, the Green function $G(t_1, t_2)$ depend on only time difference between t_1 and t_2. We define the Fourier transform,

$$
G(\tau) = \frac{1}{2\pi\hbar}\int_{-\infty}^{+\infty} dE\, G(E)e^{-i\frac{E}{\hbar}\tau},
\tag{3.91}
$$

where $\tau \equiv t_1 - t_2$. When the Fourier transform is applied to Eqs. (3.86)-(3.89), we obtain the following equations,

$$
\begin{aligned}
EG_{ij}^{--}(E) = &-\sum_m t_{im}G_{mj}^{--}(E) \\
&- t'\{\delta_{i0}G_{1j}^{--}(E) + \delta_{i1}G_{0j}^{--}(E)\} \\
&- t'\{\delta_{iN}G_{N+1,j}^{--}(E) + \delta_{i,N+1}G_{0j}^{--}(E)\} \\
&+ \delta_{ij},
\end{aligned}
\tag{3.92}
$$

$$
\begin{aligned}
EG_{ij}^{++}(E) = &-\sum_m t_{im}G_{mj}^{++}(E) \\
&- t'\{\delta_{i0}G_{1j}^{++}(E) + \delta_{i1}G_{0j}^{++}(E)\} \\
&- t'\{\delta_{iN}G_{N+1,j}^{++}(E) + \delta_{i,N+1}G_{0j}^{++}(E)\} \\
&- \delta_{ij},
\end{aligned}
\tag{3.93}
$$

$$
\begin{aligned}
EG_{ij}^{-+}(E) = &-\sum_m t_{im}G_{mj}^{-+}(E) \\
&- t'\{\delta_{i0}G_{1j}^{-+}(E) + \delta_{i1}G_{0j}^{-+}(E)\} \\
&- t'\{\delta_{iN}G_{N+1,j}^{-+}(E) + \delta_{i,N+1}G_{0j}^{-+}(E)\},
\end{aligned}
\tag{3.94}
$$

$$
\begin{aligned}
EG_{ij}^{+-}(E) = &-\sum_m t_{im}G_{mj}^{+-}(E) \\
&- t'\{\delta_{i0}G_{1j}^{+-}(E) + \delta_{i1}G_{0j}^{+-}(E)\} \\
&- t'\{\delta_{iN}G_{N+1,j}^{+-}(E) + \delta_{i,N+1}G_{0j}^{+-}(E)\}.
\end{aligned}
\tag{3.95}
$$

The matrix Green function is defined as

$$
\mathbf{G}_{ij}(E) \equiv \begin{bmatrix} G_{ij}^{--}(E) & G_{ij}^{-+}(E) \\ G_{ij}^{+-}(E) & G_{ij}^{++}(E) \end{bmatrix}.
\tag{3.96}
$$

Using the matrix Green functions, we rewrite the equations (3.92)-(3.95) as follows,

$$\sum_m \{E\delta_{im} - (-t_{im})\}\mathbf{G}_{mj}(E) - \sum_m \Sigma_{im}\mathbf{G}_{mj}(E) = \delta_{ij}\tau_z, \qquad (3.97)$$

where

$$\Sigma_{im} \equiv -t'\{\delta_{i0}\delta_{m1} + \delta_{i1}\delta_{m0}\} - t'\{\delta_{iN}\delta_{mN+1} + \delta_{iN+1}\delta_{mN}\}, \qquad (3.98)$$

and

$$\tau_z \equiv \begin{bmatrix} 1 & 0 \\ 0 & -1 \end{bmatrix}. \qquad (3.99)$$

When the perturbation term $\hat{\mathcal{W}}$ becomes zero, we rewrite the Green functions $\mathbf{G}(E)$ to the nonperturbative Green functions $\mathbf{g}(E)$. Thus, we obtain the following equation from Eq. (3.97),

$$\sum_m g_{im}^{-1}(E)\mathbf{g}_{mj}(E) = \delta_{ij}\tau_z, \qquad (3.100)$$

where $g_{im}^{-1}(E)$ is defined as

$$g_{im}^{-1}(E) \equiv E\delta_{im} - (-t_{im}). \qquad (3.101)$$

Using Eq. (3.101), the equation (3.97) is rewritten as

$$\sum_m g_{im}^{-1}(E)\mathbf{G}_{mj}(E) - \sum_m \Sigma_{im}\mathbf{G}_{mj}(E) = \delta_{ij}\tau_z. \qquad (3.102)$$

Then we use the relation $\tau_z\tau_z = 1$, and we have

$$\sum_m g_{im}^{-1}(E)\mathbf{G}_{mj}(E) - \sum_m \tau_z\mathbf{\Sigma}_{im}\mathbf{G}_{mj}(E) = \delta_{ij}\tau_z, \qquad (3.103)$$

where $\mathbf{\Sigma}_{im}$ called the matrix self-energy is defined as follows,

$$\mathbf{\Sigma}_{im} \equiv \begin{bmatrix} \Sigma_{im}^{--} & \Sigma_{im}^{-+} \\ \Sigma_{im}^{+-} & \Sigma_{im}^{++} \end{bmatrix} \equiv \tau_z\Sigma_{im} = \begin{bmatrix} \Sigma_{im} & 0 \\ 0 & -\Sigma_{im} \end{bmatrix}. \qquad (3.104)$$

Furthermore, equation (3.103) is rewritten as

$$\sum_m g_{im}^{-1}(E)\mathbf{G}_{mj}(E) - \sum_{lm} \tau_z\delta_{il}\mathbf{\Sigma}_{lm}\mathbf{G}_{mj}(E) = \delta_{ij}\tau_z, \qquad (3.105)$$

where we have used the relation $\Sigma_{im} = \sum_l \delta_{il}\Sigma_{lm}$. Inserting Eq. (3.100) to Eq. (3.105), we obtain

$$\sum_n g_{in}^{-1}(E)\Big\{\mathbf{G}_{nj}(E) - \sum_{lm} \mathbf{g}_{nl}(E)\mathbf{\Sigma}_{lm}\mathbf{G}_{mj}(E)\Big\} = \sum_n g_{in}^{-1}(E)\mathbf{g}_{nj}(E). \quad (3.106)$$

Thus we yield the equation of motion for the nonequilibrium Green functions

$$\mathbf{G}_{ij}(E) = \mathbf{g}_{ij}(E) + \sum_{lm} \mathbf{g}_{il}(E)\boldsymbol{\Sigma}_{lm}\mathbf{G}_{mj}(E), \tag{3.107}$$

where

$$\mathbf{G}_{ij}(E) \equiv \begin{bmatrix} G_{ij}^{--}(E) & G_{ij}^{-+}(E) \\ G_{ij}^{+-}(E) & G_{ij}^{++}(E) \end{bmatrix}, \tag{3.108}$$

$$\mathbf{g}_{ij}(E) \equiv \begin{bmatrix} g_{ij}^{--}(E) & g_{ij}^{-+}(E) \\ g_{ij}^{+-}(E) & g_{ij}^{++}(E) \end{bmatrix}, \tag{3.109}$$

$$\boldsymbol{\Sigma}_{lm} \equiv \begin{bmatrix} \Sigma_{lm}^{--} & 0 \\ 0 & \Sigma_{lm}^{++} \end{bmatrix}. \tag{3.110}$$

As you know, Equation (3.77) shows that the four Green functions, G^{--}, G^{++}, G^{-+}, and G^{+-}, are not independent each other. Thus, we can transform the four Green functions into the three Green functions, G^a, G^r, and G^k with aid of the transform matrix $\mathbf{P}$,

$$\mathbf{P} \equiv \frac{1}{\sqrt{2}} \begin{bmatrix} 1 & 1 \\ -1 & 1 \end{bmatrix}. \tag{3.111}$$

We introduce the Keldysh Green function, G^k, which is defined as

$$G_{ij}^k(E) \equiv G_{ij}^{--}(E) + G_{ij}^{++}(E). \tag{3.112}$$

Actually, using Eq. (3.111), the matrix Green function $\mathbf{G}_{ij}$ is transformed as follows,

$$\mathbf{P}^{-1}\mathbf{G}_{ij}\mathbf{P} = \frac{1}{2}\begin{bmatrix} G_{ij}^{--} - G_{ij}^{+-} - G_{ij}^{-+} + G_{ij}^{++} & G_{ij}^{--} - G_{ij}^{+-} + G_{ij}^{-+} - G_{ij}^{++} \\ G_{ij}^{--} + G_{ij}^{+-} - G_{ij}^{-+} - G_{ij}^{++} & G_{ij}^{--} + G_{ij}^{+-} + G_{ij}^{-+} + G_{ij}^{++} \end{bmatrix}$$
$$= \begin{bmatrix} 0 & G_{ij}^a \\ G_{ij}^r & G_{ij}^k \end{bmatrix}, \tag{3.113}$$

where we have used the equations (3.77)-(3.81). The matrix self-energy is transformed similarly,

$$\mathbf{P}^{-1}\boldsymbol{\Sigma}_{ij}\mathbf{P} = \frac{1}{2}\begin{bmatrix} \Sigma_{ij}^{--} + \Sigma_{ij}^{++} & \Sigma_{ij}^{--} - \Sigma_{ij}^{++} \\ \Sigma_{ij}^{--} - \Sigma_{ij}^{++} & \Sigma_{ij}^{--} + \Sigma_{ij}^{++} \end{bmatrix}$$
$$= \begin{bmatrix} 0 & \Sigma_{ij}^r \\ \Sigma_{ij}^a & 0 \end{bmatrix}, \tag{3.114}$$

where the retarded self-energy and the advanced self-energy are defined respectively as follows,

$$\Sigma_{ij}^r \equiv \frac{1}{2}(\Sigma_{ij}^{--} - \Sigma_{ij}^{++}), \tag{3.115}$$

$$\Sigma_{ij}^a \equiv \frac{1}{2}(\Sigma_{ij}^{--} - \Sigma_{ij}^{++}). \tag{3.116}$$

Using Eqs. (3.113) and (3.114), the transformed equation of motion for $\mathbf{G}_{ij}$ is written as

$$\mathbf{P}^{-1}\mathbf{G}_{ij}\mathbf{P} = \mathbf{P}^{-1}\mathbf{g}_{ij}\mathbf{P} + \sum_{lm}\mathbf{P}^{-1}\mathbf{g}_{il}\mathbf{P}\mathbf{P}^{-1}\mathbf{\Sigma}_{lm}\mathbf{P}\mathbf{P}^{-1}\mathbf{G}_{mj}\mathbf{P}, \qquad (3.117)$$

$$\begin{bmatrix} 0 & G_{ij}^a \\ G_{ij}^r & G_{ij}^k \end{bmatrix} = \begin{bmatrix} 0 & g_{ij}^a \\ g_{ij}^r & g_{ij}^k \end{bmatrix} + \sum_{lm} \begin{bmatrix} 0 & g_{il}^a \\ g_{il}^r & g_{il}^k \end{bmatrix} \begin{bmatrix} 0 & \Sigma_{lm}^r \\ \Sigma_{lm}^a & 0 \end{bmatrix} \begin{bmatrix} 0 & G_{mj}^a \\ G_{mj}^r & G_{mj}^k \end{bmatrix}.$$

$$(3.118)$$

As a result, we obtain the following equation of motion for the nonequilibrium Green functions,

$$G_{ij}^a(E) = g_{ij}^a(E) + \sum_{lm} g_{il}^a(E)\Sigma_{lm}^a G_{mj}^a(E), \qquad (3.119)$$

$$G_{ij}^r(E) = g_{ij}^r(E) + \sum_{lm} g_{il}^r(E)\Sigma_{lm}^r G_{mj}^r(E), \qquad (3.120)$$

$$G_{ij}^k(E) = g_{ij}^k(E) + \sum_{lm} \left\{ g_{il}^r(E)\Sigma_{lm}^r G_{mj}^k(E) + g_{il}^k(E)\Sigma_{lm}^a G_{mj}^a(E) \right\}. \qquad (3.121)$$

We introduce the following Green functions and self-energies of the matrix form,

$$\mathbf{G}^a = \begin{bmatrix} \ddots & \vdots & \vdots & & \vdots & & \vdots & & \ddots \\ \cdots & G_{00}^a & G_{01}^a & \cdots & G_{0N}^a & G_{0\,N+1}^a & \cdots \\ \cdots & G_{10}^a & G_{11}^a & \cdots & G_{1N}^a & G_{1\,N+1}^a & \cdots \\ & \vdots & \vdots & \ddots & \vdots & & \vdots & \\ \cdots & G_{N0}^a & G_{N1}^a & \cdots & G_{NN}^a & G_{N\,N+1}^a & \cdots \\ \cdots & G_{N+1\,0}^a & G_{N+1\,1}^a & \cdots & G_{N+1\,N}^a & G_{N+1\,N+1}^a & \cdots \\ \ddots & \vdots & \vdots & & \vdots & & \vdots & & \ddots \end{bmatrix}, \qquad (3.122)$$

$$\mathbf{g}^a = \begin{bmatrix} \ddots & \vdots & \vdots & & \vdots & & \vdots & & \ddots \\ \cdots & g_{00}^a & 0 & \cdots & 0 & 0 & \cdots \\ \cdots & 0 & g_{11}^a & \cdots & g_{1N}^a & 0 & \cdots \\ & \vdots & \vdots & \ddots & \vdots & & \vdots & \\ \cdots & 0 & g_{N1}^a & \cdots & g_{NN}^a & 0 & \cdots \\ \cdots & 0 & 0 & \cdots & 0 & g_{N+1\,N+1}^a & \cdots \\ \ddots & \vdots & \vdots & & \vdots & & \vdots & & \ddots \end{bmatrix}, \qquad (3.123)$$

$$\mathbf{\Sigma}^a = \begin{bmatrix} \ddots & \vdots & \vdots & & \vdots & & \vdots & & \ddots \\ \cdots & 0 & -t' & \cdots & 0 & 0 & \cdots \\ \cdots & -t' & 0 & \cdots & 0 & 0 & \cdots \\ & \vdots & \vdots & \ddots & \vdots & & \vdots & \\ \cdots & 0 & 0 & \cdots & 0 & -t' & \cdots \\ \cdots & 0 & 0 & \cdots & -t' & 0 & \cdots \\ \ddots & \vdots & \vdots & & \vdots & & \vdots & & \ddots \end{bmatrix}. \qquad (3.124)$$
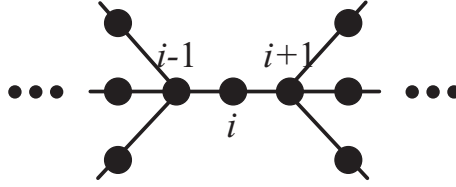
Figure 3.19: Schematic picture of the system.

The matrix forms of the other Green functions and self-energies are similarly introduced, and then we can rewrite the Dyson equations as follows,

$$\mathbf{G}^a = \mathbf{g}^a + \mathbf{g}^a \mathbf{\Sigma}^a \mathbf{G}^a, \tag{3.125}$$

$$\mathbf{G}^r = \mathbf{g}^r + \mathbf{g}^r \mathbf{\Sigma}^r \mathbf{G}^r, \tag{3.126}$$

$$\mathbf{G}^k = \mathbf{g}^k + \mathbf{g}^r \mathbf{\Sigma}^r \mathbf{G}^k + \mathbf{g}^k \mathbf{\Sigma}^a \mathbf{G}^a. \tag{3.127}$$

3.5.5   Electric current formula

We consider the electronic current flowing through the i-th site as shown in Fig. 3.19. We assume that the electronic current between $(i-1)$-th site and i-th site is represented by $\hat{I}_l$. Similarly, the current between i-th site and $(i+1)$-th site is written by $\hat{I}_r$. We write the continuity equation around i-th site under the tight-binding approximation,

$$\hat{I}_{rH}(t) - \hat{I}_{lH}(t) = -\frac{\partial \hat{\rho}_{Hi}(t)}{\partial t}, \tag{3.128}$$

where the electron charge at i-th site is written as

$$\hat{\rho}_{Hi}(t) = -e\hat{c}^\dagger_{Hi}(t)\hat{c}_{Hi}(t). \tag{3.129}$$

The electronic current between i-th site and $(i+1)$-th site is the difference between the flow of electrons from left to right and right to left. We thus expect the current operator $\hat{I}_r$ of the form

$$\hat{I}_{rH}(t) = A_{i+1,i}\hat{c}^\dagger_{Hi+1}(t)\hat{c}_{Hi}(t) - A_{i,i+1}\hat{c}^\dagger_{Hi}(t)\hat{c}_{Hi+1}(t). \tag{3.130}$$

The electronic current operator $\hat{I}_l$ between $(i-1)$-th site and i-th site is similarly written,

$$\hat{I}_{lH}(t) = A_{i,i-1}\hat{c}^\dagger_{Hi}(t)\hat{c}_{Hi-1}(t) - A_{i-1,i}\hat{c}^\dagger_{Hi-1}(t)\hat{c}_{Hi}(t). \tag{3.131}$$

Using the Heisenberg equation, we find

$$\frac{\partial \hat{\rho}_{Hi}(t)}{\partial t} = \frac{1}{i\hbar}[\hat{\rho}_{Hi}(t), \hat{\mathcal{H}}_H(t)] \tag{3.132}$$

$$= \frac{1}{i\hbar}\left\{\hat{\rho}_{Hi}(t)\hat{\mathcal{H}}_H(t) - \hat{\mathcal{H}}_H(t)\hat{\rho}_{Hi}(t)\right\} \tag{3.133}$$

$$= \frac{e}{i\hbar}\left\{\sum_m t_{im}\hat{c}^\dagger_{Hi}(t)\hat{c}_{Hm}(t) - \sum_l t_{li}\hat{c}^\dagger_{Hl}(t)\hat{c}_{Hi}(t)\right\} \tag{3.134}$$

As shown in Fig. 3.19, i-th site is connected to only both $(i-1)$-th site and $(i+1)$-th site. Therefore, we have

$$\frac{\partial \hat{\rho}_{Hi}(t)}{\partial t} = \frac{e}{i\hbar} \left\{ t_{i,i-1} \hat{c}_{Hi}^{\dagger}(t) \hat{c}_{Hi-1}(t) + t_{i,i+1} \hat{c}_{Hi}^{\dagger}(t) \hat{c}_{Hi+1}(t) \right.$$
$$\left. - t_{i-1,i} \hat{c}_{Hi-1}^{\dagger}(t) \hat{c}_{Hi}(t) - t_{i+1,i} \hat{c}_{Hi+1}^{\dagger}(t) \hat{c}_{Hi}(t) \right\}. \tag{3.135}$$

A comparison of equations (3.128) and (3.135) yields

$$A_{lm} = \frac{e}{i\hbar} t_{lm}. \tag{3.136}$$

When we assume $t_{lm} = t_{ml}$, the electronic current is written as follows

$$\langle I_r(t) \rangle = \frac{e}{i\hbar} t_{i,i+1} \langle \hat{c}_{Hi+1}^{\dagger}(t) \hat{c}_{Hi}(t) - \hat{c}_{Hi}^{\dagger}(t) \hat{c}_{Hi+1}(t) \rangle \tag{3.137}$$

$$= e t_{i,i+1} \{ G_{i+1,i}^{-+}(t,t) - G_{i,i+1}^{-+}(t,t) \}, \tag{3.138}$$

where Eq. (3.74) has been used. In a steady state, using the Fourier transform (3.91), we have

$$\langle I_r \rangle = \frac{e t_{i,i+1}}{2\pi\hbar} \int_{-\infty}^{+\infty} dE \left\{ G_{i+1,i}^{-+}(E) - G_{i,i+1}^{-+}(E) \right\} \tag{3.139}$$

$$= \frac{e}{2h} t_{i,i+1} \int_{-\infty}^{+\infty} dE \left\{ G_{i+1,i}^{k}(E) - G_{i,i+1}^{k}(E) \right\}. \tag{3.140}$$

Here, to obtain Eq. (3.140) we have used the following relations,

$$G_{ij}^{-+} = \frac{1}{2} (-G_{ij}^{r} + G_{ij}^{a} + G_{ij}^{k}). \tag{3.141}$$

In case of the joint system shown in Fig. 3.3, the electronic current between the left electrode and the Kagomé-lattice chain is written as

$$\langle I \rangle = \frac{e}{2h} t' \int_{-\infty}^{+\infty} dE \left\{ G_{10}^{k}(E) - G_{01}^{k}(E) \right\}. \tag{3.142}$$

Similarly, we can obtain the electron number density at i-th site,

$$\langle n_i \rangle = -e \langle \hat{c}_i^{\dagger} \hat{c}_i \rangle \tag{3.143}$$

$$= \frac{e}{2\pi} \int_{-\infty}^{+\infty} dE G_{ii}^{-+}(E) \tag{3.144}$$

$$= \frac{e}{4\pi} \int_{-\infty}^{+\infty} dE (-G_{ii}^{r}(E) + G_{ij}^{a}(E) + G_{ij}^{k}(E)). \tag{3.145}$$

3.5.6   Green functions for the isolated systems

In this subsection, we produce the Green functions $\mathbf{g}(E)$ of the isolated electrodes and the Kagomé-lattice chains.

(a)

(b)

(c)
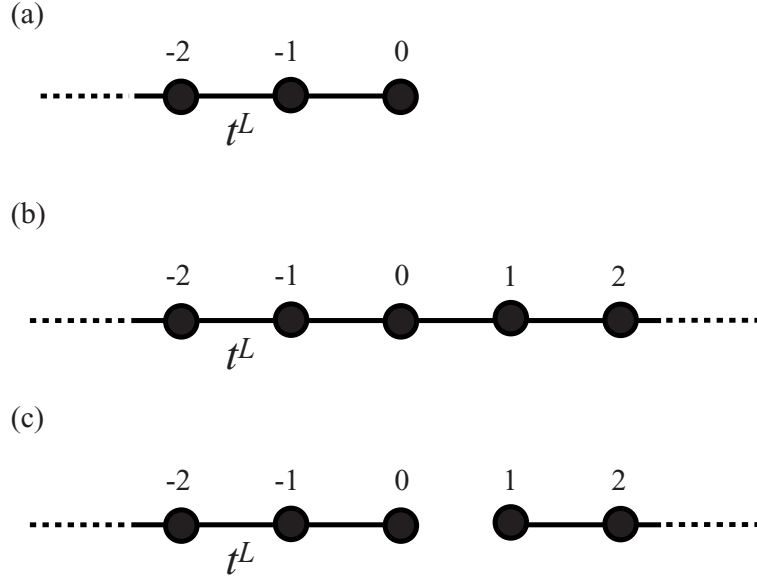
Figure 3.20: (a) One-dimensional lattices having a half-infinity length under the tight-binding approximation. (b) Infinite length one-dimensional lattice. (c) Half infinite length one-dimensional lattices produced by removing the electron transfer between 0-th site and 1-st site.

Green functions for the electrodes

In this paper, we assume that both source and drain electrodes are represented by the tight-binding models of one-dimensional lattices having a half-infinity length as shown in Fig. 3.20(a). The Hamiltonian of an electrode is written as follows,

$$\hat{\mathcal{H}}^L = -\sum_{ij \leq 0} t^L \hat{c}_i^\dagger \hat{c}_j. \tag{3.146}$$

To produce the half-infinity length one-dimensional lattice, we remove the transfer between 0-th site and 1-st site from the infinite length one-dimensional lattice. The situation is shown in Figs. 3.20(b) and 3.20(c). Therefore, we rewrite the Hamiltonian of the electrode as follows,

$$\hat{\mathcal{H}}^L = \hat{\mathcal{H}}_0^L + \hat{\mathcal{H}}_1^L, \tag{3.147}$$

where

$$\hat{\mathcal{H}}_0^L = -\sum_{ij} t^L \hat{c}_i^\dagger \hat{c}_j, \tag{3.148}$$

$$\hat{\mathcal{H}}_1^L = +t^L (\hat{c}_0^\dagger \hat{c}_1 + \hat{c}_1^\dagger \hat{c}_0). \tag{3.149}$$

$\hat{\mathcal{H}}_0^L$ represents the Hamiltonian of the infinite length one-dimensional lattice. In the previous subsections, we have already obtained the Dyson equations (3.119)-(3.121) from the Hamiltonian (3.39). In the similar way with this process, we

obtain the following Dyson equations from the Hamiltonian (3.147),

$$g_{ij}^a(E) = g_{ij}^{0a}(E) + \sum_{lm} g_{il}^{0a}(E)\sigma_{lm}^a g_{mj}^a(E), \tag{3.150}$$

$$g_{ij}^r(E) = g_{ij}^{0r}(E) + \sum_{lm} g_{il}^{0r}(E)\sigma_{lm}^r g_{mj}^r(E), \tag{3.151}$$

$$g_{ij}^k(E) = g_{ij}^{0k}(E) + \sum_{lm} \left\{ g_{il}^{0r}(E)\sigma_{lm}^r g_{mj}^k(E) + g_{il}^{0k}(E)\sigma_{lm}^a g_{mj}^a(E) \right\}, \tag{3.152}$$

where the self-energies are defined as

$$\sigma_{lm}^a = \sigma_{lm}^r = t^L(\delta_{l0}\delta_{m1} + \delta_{l1}\delta_{m0}). \tag{3.153}$$

Here $g_{ij}(E)$ and $g_{ij}^0(E)$ are the Green functions for the half-infinite length electrode and the infinite length one-dimensional lattice, respectively. Inserting Eq. (3.153) to Eq. (3.150), we obtain

$$g_{ij}^a(E) = g_{ij}^{0a}(E) + t^L \sum_{lm} g_{il}^{0a}(E)(\delta_{l0}\delta_{m1} + \delta_{l1}\delta_{m0})g_{mj}^a(E)$$
$$= g_{ij}^{0a}(E) + t^L g_{i0}^{0a}(E)g_{1j}^a(E) + t^L g_{i1}^{0a}(E)g_{0j}^a(E). \tag{3.154}$$

Both i and j are zero or less, because g_{ij}^a is the Green function of the left-side half infinite length one-dimensional lattice shown in Fig. 3.20(c). Thus, the Green function g_{1j}^a becomes zero, because electrons in the left-side lattice can not transfer to the right-side lattice. Thus, we yield following equation from Eq. (3.154),

$$g_{ij}^a(E) = g_{ij}^{0a}(E) + t^L g_{i1}^{0a}(E)g_{0j}^a(E). \tag{3.155}$$

When $i = 0$, we obtain the Green function g_{0j}^a as follows,

$$g_{0j}^a(E) = \frac{g_{0j(E)}^{0a}}{1 - t^L g_{01}^{0a}(E)}. \tag{3.156}$$

Inserting Eq. (3.156) to Eq. (3.155), we have advanced Green functions for electrodes,

$$g_{ij}^a(E) = g_{ij}^{0a}(E) + t^L \frac{g_{i1}^{0a}(E)g_{0j}^{0a}(E)}{1 - t^L g_{01}^{0a}(E)}. \tag{3.157}$$

In the same way, we obtain the retarded Green functions,

$$g_{ij}^r(E) = g_{ij}^{0r}(E) + t^L \frac{g_{i1}^{0r}(E)g_{0j}^{0r}(E)}{1 - t^L g_{01}^{0r}(E)}. \tag{3.158}$$

The Green functions for the infinite length one-dimensional lattice $g_{ij}^{0a}(g_{ij}^{0r})$ are necessary to calculate the Green functions $g_{ij}^a(g_{ij}^r)$.

The Green function $g_{ij}^{0--}(t_1, t_2)$ for the infinite length one-dimensional lattice is defined as

$$g_{ij}^{0--}(t_1, t_2) = \frac{1}{i\hbar}\langle \mathrm{T}[\hat{c}_{Hi}(t_1)\hat{c}_{Hj}^\dagger(t_2)]\rangle$$
$$= \frac{1}{i\hbar}\left\{ \langle \hat{c}_{Hi}(t_1)\hat{c}_{Hj}^\dagger(t_2)\rangle\theta(t_1 - t_2) - \langle \hat{c}_{Hj}^\dagger(t_2)\hat{c}_{Hi}(t_1)\rangle\theta(t_2 - t_1) \right\}, \tag{3.159}$$

where $\hat{c}_{Hi}(t) = \exp\left[-\frac{\hat{\mathcal{H}}_0^L}{i\hbar}t\right]\hat{c}_i \exp\left[\frac{\hat{\mathcal{H}}_0^L}{i\hbar}t\right]$. When there is no interaction between electrons in the periodic system, we can develop the operator $\hat{c}_i$ in the plane wave,

$$\hat{c}_{Hi}(t) = \exp\left[-\frac{\hat{\mathcal{H}}_0^L}{i\hbar}t\right]\hat{c}_i \exp\left[+\frac{\hat{\mathcal{H}}_0^L}{i\hbar}t\right] \tag{3.160}$$

$$= \frac{1}{\sqrt{N}}\sum_k \exp\left[ik\cdot(ia)\right]\exp\left[-\frac{\hat{\mathcal{H}}_0^L}{i\hbar}t\right]\hat{c}_k \exp\left[+\frac{\hat{\mathcal{H}}_0^L}{i\hbar}t\right], \tag{3.161}$$

where k is the wavevector and $\hat{c}_k$ represents the annihilation operator of an electron with a wavevector k. Here we put the distance between nearest neighbor sites with a. Applying the operator $\hat{c}_{Hi}(t)$ to the state $|I\rangle$, we obtain

$$\hat{c}_{Hi}(t)|I\rangle = \frac{1}{\sqrt{N}}\sum_k \exp\left[ik\cdot(ia)\right]\exp\left[-\frac{\hat{\mathcal{H}}_0^L}{i\hbar}t\right]\hat{c}_k \exp\left[+\frac{\hat{\mathcal{H}}_0^L}{i\hbar}t\right]|I\rangle, \tag{3.162}$$

$$= \frac{1}{\sqrt{N}}\sum_k \exp\left[ik\cdot(ia)\right]\exp\left[-\frac{\hat{\mathcal{H}}_0^L}{i\hbar}t\right]\hat{c}_k \exp\left[+\frac{\mathcal{E}_{0I}^L}{i\hbar}t\right]|I\rangle, \tag{3.163}$$

$$= \frac{1}{\sqrt{N}}\sum_k \exp\left[ik\cdot(ia)\right]\exp\left[-\frac{\mathcal{E}_{0F}^L}{i\hbar}t\right]\exp\left[+\frac{\mathcal{E}_{0I}^L}{i\hbar}t\right]|F\rangle, \tag{3.164}$$

$$= \frac{1}{\sqrt{N}}\sum_k \exp\left[ik\cdot(ia)\right]\exp\left[+\frac{\mathcal{E}_{0I}^L - \mathcal{E}_{0F}^L}{i\hbar}t\right]\hat{c}_k|I\rangle, \tag{3.165}$$

where we have defined $|F\rangle = \hat{c}_k|I\rangle$. $\mathcal{E}_{0I}^L$ and $\mathcal{E}_{0F}^L$ are represent the eigenenergies of $\hat{\mathcal{H}}_0^L$ for the states $|I\rangle$ and $|F\rangle$, respectively. The energy difference $\mathcal{E}_{0I}^L - \mathcal{E}_{0F}^L$ corresponds to the energy of an electron with wavevector k, thus we define

$$\mathcal{E}_k \equiv \mathcal{E}_{0I}^L - \mathcal{E}_{0F}^L. \tag{3.166}$$

Therefore, we have the following equation,

$$\hat{c}_{Hi}(t_1) = \frac{1}{\sqrt{N}}\sum_k \exp\left[ik\cdot(ia)\right]\exp\left[-i\frac{\mathcal{E}_k}{\hbar}t_1\right]\hat{c}_k, \tag{3.167}$$

$$\hat{c}_{Hj}^\dagger(t_2) = \frac{1}{\sqrt{N}}\sum_k \exp\left[-ik\cdot(ja)\right]\exp\left[+i\frac{\mathcal{E}_k}{\hbar}t_2\right]\hat{c}_k^\dagger. \tag{3.168}$$

Inserting Eqs. (3.167) and (3.168) to Eq. (3.159), the Green function $g_{ij}^{0--}(t_1, t_2)$ is rewritten as

$$g_{ij}^{0--}(t_1, t_2) = \frac{1}{i\hbar}\frac{1}{N}\Bigg\{\sum_{kk'}\langle\hat{c}_k\hat{c}_{k'}^\dagger\rangle e^{ik(ia)-i\frac{\mathcal{E}_k}{\hbar}t_1}e^{-ik'(ja)+i\frac{\mathcal{E}_{k'}}{\hbar}t_2}\theta(t_1 - t_2)$$

$$- \sum_{kk'}\langle\hat{c}_{k'}^\dagger\hat{c}_k\rangle e^{-ik'(ja)+i\frac{\mathcal{E}_{k'}}{\hbar}t_2}e^{ik(ia)-i\frac{\mathcal{E}_k}{\hbar}t_1}\theta(t_2 - t_1)\Bigg\}. \tag{3.169}$$

To calculate the pair-correlation functions, we introduce the Fermi distribution function f_k.

$$\langle\hat{c}_{k'}^\dagger\hat{c}_k\rangle = \delta_{kk'}f_k, \tag{3.170}$$

$$\langle \hat{c}_k \hat{c}_{k'}^\dagger \rangle = \langle \delta_{kk'} - \hat{c}_{k'}^\dagger \hat{c}_k \rangle = \delta_{kk'} - \langle \hat{c}_{k'}^\dagger \hat{c}_k \rangle = \delta_{kk'}(1 - f_k). \tag{3.171}$$

Using Eqs. (3.170) and (3.171), we have

$$
\begin{aligned}
g_{ij}^{0--}(t_1, t_2) = \frac{1}{i\hbar}\frac{1}{N}\Bigg\{ &\sum_k e^{ik(i-j)a} e^{-i\frac{\mathcal{E}_k}{\hbar}(t_1-t_2)}(1 - f_k)\theta(t_1 - t_2) \\
&- \sum_k e^{ik(i-j)a} e^{-i\frac{\mathcal{E}_k}{\hbar}(t_1-t_2)} f_k\theta(t_2 - t_1)\Bigg\}.
\end{aligned}
\tag{3.172}
$$

This equation depends on only time deference $\tau \equiv (t_1 - t_2)$. Therefore we obtain the following equation by performing the Fourier transform,

$$
\begin{aligned}
g_{ij}^{0--}(E) &= \int_{-\infty}^{+\infty} d\tau \, g_{ij}^{0--}(\tau)e^{+i\frac{E}{\hbar}\tau} \\
&= \frac{1}{i\hbar}\frac{1}{N}\Bigg\{ \sum_k e^{ik(i-j)a}(1 - f_k)\int_0^{+\infty} d\tau \, e^{i\frac{E-\mathcal{E}_k}{\hbar}\tau} \\
&\quad - \sum_k e^{ik(i-j)a} f_k \int_{-\infty}^0 d\tau \, e^{i\frac{E-\mathcal{E}_k}{\hbar}\tau}\Bigg\} \\
&= \frac{1}{i\hbar}\frac{1}{N}\Bigg\{ \sum_k e^{ik(i-j)a}(1 - f_k)\left[\frac{e^{i(\frac{E-\mathcal{E}_k}{\hbar}+i\delta)\tau}}{i(\frac{E-\mathcal{E}_k}{\hbar} + i\delta)}\right]_{\tau=0}^{\tau=+\infty} \\
&\quad - \sum_k e^{ik(i-j)a} f_k \left[\frac{e^{i(\frac{E-\mathcal{E}_k}{\hbar}-i\delta)\tau}}{i(\frac{E-\mathcal{E}_k}{\hbar} - i\delta)}\right]_{\tau=-\infty}^{\tau=0}\Bigg\} \\
&= \frac{1}{N}\sum_k e^{ik(i-j)a}\left\{\frac{1 - f_k}{E - \mathcal{E}_k + i\delta} + \frac{f_k}{E - \mathcal{E}_k - i\delta}\right\}.
\end{aligned}
\tag{3.173}
$$

We have the other Green functions similarly,

$$g_{ij}^{0++}(E) = \frac{1}{N}\sum_k e^{ik(i-j)a}\left\{\frac{-1 + f_k}{E - \mathcal{E}_k + i\delta} + \frac{-f_k}{E - \mathcal{E}_k - i\delta}\right\}, \tag{3.174}$$

$$g_{ij}^{0+-}(E) = \frac{1}{i\hbar}\frac{1}{N}\sum_k e^{ik(i-j)a}(1 - f_k)2\pi\delta(\mathcal{E}_k - E), \tag{3.175}$$

$$g_{ij}^{0-+}(E) = -\frac{1}{i\hbar}\frac{1}{N}\sum_k e^{ik(i-j)a} f_k 2\pi\delta(\mathcal{E}_k - E). \tag{3.176}$$

Using Eqs. (3.173)-(3.176), we obtain the Green functions $g_{ij}^{0r}(E)$, $g_{ij}^{0a}(E)$, and

$g_{ij}^{0k}(E)$, as follows,

$$g_{ij}^{0r}(E) = g_{ij}^{0--}(E) - g_{ij}^{0-+}(E) \tag{3.177}$$

$$= \frac{1}{N}\sum_k \frac{e^{ik(i-j)a}}{E - \mathcal{E}_k + i\delta}, \tag{3.178}$$

$$g_{ij}^{0a}(E) = g_{ij}^{0--}(E) - g_{ij}^{0+-}(E) \tag{3.179}$$

$$= \frac{1}{N}\sum_k \frac{e^{ik(i-j)a}}{E - \mathcal{E}_k - i\delta}, \tag{3.180}$$

$$g_{ij}^{0k}(E) = g_{ij}^{0-+}(E) + g_{ij}^{0+-}(E) \tag{3.181}$$

$$= (1 - 2f(E))(g_{ij}^{0r}(E) - g_{ij}^{0a}(E)), \tag{3.182}$$

where the relation $\frac{1}{x-i\delta} = \mathrm{P}\frac{1}{x} + i\pi\delta(x)$ has been used. Note that the electron distribution function $f(E)$ is included in only the Keldysh Green function. Because $\mathcal{E}_k$ is the eigenenergy of the infinite length one-dimensional lattice, $\mathcal{E}_k$ is written as

$$\mathcal{E}_k = -2t^L \cos ka. \tag{3.183}$$

Thus, we obtain the following retarded Green function $g_{ij}^{0r}(E)$,

$$g_{ij}^{0r}(E) = \frac{1}{N}\sum_k \frac{e^{ik(i-j)a}}{E + 2t^L \cos ka + i\delta} \tag{3.184}$$

$$= \frac{1}{N}\frac{Na}{2\pi}\int_{-\frac{\pi}{a}}^{+\frac{\pi}{a}} dk \frac{e^{ik(i-j)a}}{E + 2t^L \cos ka + i\delta}. \tag{3.185}$$

The Green function g_{ij}^{0r} depends on only site difference $m \equiv i - j$. We can rewrite Eq. (3.185) as follows,

$$g_{|m|}^{0r}(E) = \frac{a}{2\pi}\int_{-\frac{\pi}{a}}^{+\frac{\pi}{a}} dk \, \frac{e^{ik|m|a}}{E + 2t^L \cos ka + i\delta} \tag{3.186}$$

$$= \frac{1}{2\pi}\int_{-\pi}^{+\pi} d\theta \, \frac{(e^{i\theta})^{|m|}}{E + 2t^L \cos\theta + i\delta} \qquad (\theta = ka) \tag{3.187}$$

$$= \frac{1}{2\pi}\oint_{|z|=1} dz \, \frac{1}{iz}\frac{z^{|m|}}{E + t^L(z + z^{-1}) + i\delta} \qquad (z = e^{i\theta}) \tag{3.188}$$

$$= \frac{1}{2\pi i}\oint_{|z|=1} dz \, \frac{z^{|m|}}{t^L\{z^2 - \frac{E+i\delta}{t^L}z + 1\}}. \tag{3.189}$$

The integrand has the following poles.

$$z_{pole} = \frac{E \pm \sqrt{E^2 - 4(t^L)^2} + i\delta \cdot \left(1 \pm E\frac{\sqrt{E^2-4(t^L)^2}}{E^2-4(t^L)^2}\right)}{2t^L} \tag{3.190}$$

Using the residue theorem, the Green function $g_{|m|}^{0r}$ is obtained as follows.

- For $-2t^L < E < 2t^L$,

  we have

  $$g_{|m|}^{0r}(E) = -\frac{i}{\sqrt{4(t^L)^2 - E^2}}\left(\frac{E - i\sqrt{4(t^L)^2 - E^2}}{2t^L}\right)^{|m|}. \qquad (3.191)$$

  In the same way, we have

  $$g_{|m|}^{0a}(E) = +\frac{i}{\sqrt{4(t^L)^2 - E^2}}\left(\frac{E + i\sqrt{4(t^L)^2 - E^2}}{2t^L}\right)^{|m|}. \qquad (3.192)$$

  The absolute values of Green functions, $|g_{|m|}^{0r}|$ and $|g_{|m|}^{0a}|$, are independent of the distance $|m|$. It means that electrons in the energy band of the one-dimensional lattice can propagate without damping.

- For $E < -2t^L$,

  we have following form,

  $$g_{|m|}^{0r}(E) = -\frac{1}{\sqrt{E^2 - 4(t^L)^2}}\left(\frac{E + \sqrt{E^2 - 4(t^L)^2}}{2t^L}\right)^{|m|}, \qquad (3.193)$$

  $$g_{|m|}^{0a}(E) = -\frac{1}{\sqrt{E^2 - 4(t^L)^2}}\left(\frac{E + \sqrt{E^2 - 4(t^L)^2}}{2t^L}\right)^{|m|}. \qquad (3.194)$$

- For $E > 2t^L$,

  we have following form,

  $$g_{|m|}^{0r}(E) = \frac{1}{\sqrt{E^2 - 4(t^L)^2}}\left(\frac{E - \sqrt{E^2 - 4(t^L)^2}}{2t^L}\right)^{|m|}, \qquad (3.195)$$

  $$g_{|m|}^{0a}(E) = \frac{1}{\sqrt{E^2 - 4(t^L)^2}}\left(\frac{E - \sqrt{E^2 - 4(t^L)^2}}{2t^L}\right)^{|m|}. \qquad (3.196)$$

  When electrons are in the outside of the energy band of the one-dimensional lattice, the absolute values of Green functions, $|g_{|m|}^{0r}|$ and $|g_{|m|}^{0a}|$, decrease proportional to the distance $|m|$. It means that electrons can not propagate without damping.

Inserting Eqs. (3.191)-(3.196) to Eqs. (3.157) and (3.158), we can obtain the Green functions for electrodes. Especially, the Green function at the edge (0-th site) of the electrode is written as

$$g_{00}^a(E) = \frac{g_{|0|}^{0a}(E)}{1 - t^L g_{|1|}^{0a}(E)} = \begin{cases} \dfrac{2}{E + \sqrt{E^2 - 4(t^L)^2}} & \text{for } E > 2t^L, \\[2ex] \dfrac{E + i\sqrt{4(t^L)^2 - E^2}}{2(t^L)^2} & \text{for } -2t^L < E < 2t^L, \\[2ex] \dfrac{2}{E - \sqrt{E^2 - 4(t^L)^2}} & \text{for } E < -2t^L. \end{cases} \qquad (3.197)$$

Green functions for the Kagome-lattice chain

The statistical average of operator $\hat{\mathcal{O}}$ is given by Eq. (3.65),

$$\langle \mathcal{O}(t) \rangle = \mathrm{Tr}[\hat{\rho}(t_0)\hat{\mathcal{O}}_H(t)] \tag{3.198}$$

$$= \sum_{lm} \langle N, l|\hat{\rho}(t_0)|N, m\rangle\langle N, m|\hat{\mathcal{O}}_H(t)|N, l\rangle \tag{3.199}$$

$$= \sum_{l} \langle N, l|\hat{\rho}(t_0)|N, l\rangle\langle N, l|\hat{\mathcal{O}}_H(t)|N, l\rangle. \tag{3.200}$$

Here $|N, l\rangle$ is the N-electron eigenstate of the Hamiltonian $\hat{\mathcal{H}}^C$ and has the eigenenergy $\mathcal{E}_l$. To obtain the Green function $g_{ij}^{--}(E)$, we calculate $(\rho(t_0))_{ll} \equiv \langle N, l|\hat{\rho}(t_0)|N, l\rangle$ and $(g_{ij}^{--}(t_1, t_2))_{ll} \equiv \langle N, l|\mathrm{T}[\hat{c}_{Hi}\hat{c}_{Hj}^{\dagger}]|N, l\rangle$, and then we obtain the Green function by using Eq. (3.200). The density matrix is obtained as follows,

$$(\hat{\rho}(t_0))_{ll} \equiv \langle N, l|\hat{\rho}(t_0)|N, l\rangle \tag{3.201}$$

$$= \frac{\langle N, l|e^{-\beta(\hat{\mathcal{H}}^C - \mu^C \hat{\mathcal{N}}^C)}|N, l\rangle}{\mathrm{Tr}[e^{-\beta(\hat{\mathcal{H}}^C - \mu^C \hat{\mathcal{N}}^C)}]}, \tag{3.202}$$

where μ^C is the Fermi energy of the isolated Kagomé-lattice chain. Then, we obtain $(g_{ij}^{--}(t_1, t_2))_{ll}$ as follows,

$$i\hbar(g_{ij}^{--}(t_1, t_2))_{ll} \equiv \langle N, l|\mathrm{T}[\hat{c}_{Hi}(t_1)\hat{c}_{Hj}^{\dagger}(t_2)]|N, l\rangle$$

$$= \sum_{m} \Big\{ \langle N, l|\hat{c}_{Hi}(t_1)|N+1, m\rangle\langle N+1, m|\hat{c}_{Hj}^{\dagger}(t_2)|N, l\rangle\theta(t_1 - t_2)$$

$$- \langle N, l|\hat{c}_{Hj}^{\dagger}(t_2)|N-1, m\rangle\langle N-1, m|\hat{c}_{Hi}(t_1)|N, l\rangle\theta(t_2 - t_1) \Big\}. \tag{3.203}$$

Using the relation $\hat{c}_{Hi}(t_1) = \exp\big[+ i\frac{\hat{\mathcal{H}}^C}{\hbar}t_1\big]\hat{c}_{Hi}\exp\big[- i\frac{\hat{\mathcal{H}}^C}{\hbar}t_1\big]$, equation (3.203) is rewritten as follows,

$$i\hbar(g_{ij}^{--}(\tau))_{ll} = \sum_{m} \Big\{ e^{+i\frac{\mathcal{E}_l - \mathcal{E}_m}{\hbar}\tau}\langle N, l|\hat{c}_i|N+1, m\rangle\langle N+1, m|\hat{c}_j^{\dagger}|N, l\rangle\theta(\tau)$$

$$- e^{-i\frac{\mathcal{E}_l - \mathcal{E}_m}{\hbar}\tau}\langle N, l|\hat{c}_j^{\dagger}|N-1, m\rangle\langle N-1, m|\hat{c}_i|N, l\rangle\theta(-\tau) \Big\}, \tag{3.204}$$

where $\tau = t_1 - t_2$. We perform the Fourier transform for Eq. (3.204) and obtain,

$$i\hbar(g_{ij}^{--}(E))_{ll} = \sum_{m} \int_{-\infty}^{+\infty} d\tau e^{i\frac{E}{\hbar}\tau} \Big\{ e^{+i\frac{\mathcal{E}_l - \mathcal{E}_m}{\hbar}\tau}\langle N, l|\hat{c}_i|N+1, m\rangle\langle N+1, m|\hat{c}_j^{\dagger}|N, l\rangle\theta(\tau)$$

$$- e^{-i\frac{\mathcal{E}_l - \mathcal{E}_m}{\hbar}\tau}\langle N, l|\hat{c}_j^{\dagger}|N-1, m\rangle\langle N-1, m|\hat{c}_i|N, l\rangle\theta(-\tau) \Big\}$$

$$= \sum_{m} \Big\{ \int_{0}^{+\infty} d\tau e^{+i\frac{E + \mathcal{E}_l - \mathcal{E}_m}{\hbar}\tau - \delta\tau}\langle N, l|\hat{c}_i|N+1, m\rangle\langle N+1, m|\hat{c}_j^{\dagger}|N, l\rangle$$

$$- \int_{-\infty}^{0} d\tau e^{+i\frac{E - \mathcal{E}_l + \mathcal{E}_m}{\hbar}\tau + \delta\tau}\langle N, l|\hat{c}_j^{\dagger}|N-1, m\rangle\langle N-1, m|\hat{c}_i|N, l\rangle \Big\}. \tag{3.205}$$

Carrying out the integration, we have

$$(g_{ij}^{--}(E))_{ll} = \sum_m \left\{ \frac{\langle N, l|\hat{c}_i|N+1, m\rangle\langle N+1, m|\hat{c}_j^\dagger|N, l\rangle}{E + \mathcal{E}_l - \mathcal{E}_m + i\delta} \right.$$

$$\left. + \frac{\langle N, l|\hat{c}_j^\dagger|N-1, m\rangle\langle N-1, m|\hat{c}_i|N, l\rangle}{E - \mathcal{E}_l + \mathcal{E}_m - i\delta} \right\}.$$

(3.206)

Other functions are obtained similarly,

$$(g_{ij}^{++}(E))_{ll} = -\sum_m \left\{ \frac{\langle N, l|\hat{c}_i|N+1, m\rangle\langle N+1, m|\hat{c}_j^\dagger|N, l\rangle}{E + \mathcal{E}_l - \mathcal{E}_m - i\delta} \right.$$

$$\left. + \frac{\langle N, l|\hat{c}_j^\dagger|N-1, m\rangle\langle N-1, m|\hat{c}_i|N, l\rangle}{E - \mathcal{E}_l + \mathcal{E}_m + i\delta} \right\},$$

(3.207)

$$(g_{ij}^{+-}(E))_{ll} = -i\sum_m 2\pi\delta(E + \mathcal{E}_l - \mathcal{E}_m)\langle N, l|\hat{c}_i|N+1, m\rangle\langle N+1, m|\hat{c}_j^\dagger|N, l\rangle,$$

(3.208)

$$(g_{ij}^{-+}(E))_{ll} = i\sum_m 2\pi\delta(E + \mathcal{E}_l - \mathcal{E}_m)\langle N, l|\hat{c}_j^\dagger|N-1, m\rangle\langle N-1, m|\hat{c}_i|N, l\rangle.$$

(3.209)

We can produce the following functions using Eqs. (3.206)-(3.209).

$$(g_{ij}^r(E))_{ll} = (g_{ij}^{--}(E))_{ll} - (g_{ij}^{-+}(E))_{ll}$$

$$= \sum_m \left\{ \frac{\langle N, l|\hat{c}_i|N+1, m\rangle\langle N+1, m|\hat{c}_j^\dagger|N, l\rangle}{E + \mathcal{E}_l - \mathcal{E}_m + i\delta} \right.$$

$$\left. + \frac{\langle N, l|\hat{c}_j^\dagger|N-1, m\rangle\langle N-1, m|\hat{c}_i|N, l\rangle}{E - \mathcal{E}_l + \mathcal{E}_m + i\delta} \right\},$$

(3.210)

$$(g_{ij}^a(E))_{ll} = (g_{ij}^{--}(E))_{ll} - (g_{ij}^{+-}(E))_{ll}$$

$$= \sum_m \left\{ \frac{\langle N, l|\hat{c}_i|N+1, m\rangle\langle N+1, m|\hat{c}_j^\dagger|N, l\rangle}{E + \mathcal{E}_l - \mathcal{E}_m - i\delta} \right.$$

$$\left. + \frac{\langle N, l|\hat{c}_j^\dagger|N-1, m\rangle\langle N-1, m|\hat{c}_i|N, l\rangle}{E - \mathcal{E}_l + \mathcal{E}_m - i\delta} \right\},$$

(3.211)

$$(g_{ij}^k(E))_{ll} = (g_{ij}^{-+}(E))_{ll} - (g_{ij}^{+-}(E))_{ll}$$

$$= \sum_m \left\{ \frac{\langle N, l|\hat{c}_i|N+1, m\rangle\langle N+1, m|\hat{c}_j^\dagger|N, l\rangle}{E + \mathcal{E}_l - \mathcal{E}_m + i\delta} \right.$$

$$- \frac{\langle N, l|\hat{c}_i|N+1, m\rangle\langle N+1, m|\hat{c}_j^\dagger|N, l\rangle}{E + \mathcal{E}_l - \mathcal{E}_m - i\delta}$$

$$+ \frac{\langle N, l|\hat{c}_j^\dagger|N-1, m\rangle\langle N-1, m|\hat{c}_i|N, l\rangle}{E - \mathcal{E}_l + \mathcal{E}_m - i\delta}$$

$$\left. - \frac{\langle N, l|\hat{c}_j^\dagger|N-1, m\rangle\langle N-1, m|\hat{c}_i|N, l\rangle}{E - \mathcal{E}_l + \mathcal{E}_m + i\delta} \right\}.$$

(3.212)

Using Eqs. (3.200), (3.202) and (3.210), the advanced Green function for the Kagomé-lattice chain is given by,

$$g_{ij}^a(E) = \sum_l (\rho(t_0))_{ll}(g_{ij}^a(E))_{ll} \tag{3.213}$$

$$= \sum_l \frac{\langle N,l|e^{-\beta(\hat{\mathcal{H}}^C - \mu^C \hat{\mathcal{N}}^C)}|N,l\rangle}{\text{Tr}[e^{-\beta(\hat{\mathcal{H}}^C - \mu^C \hat{\mathcal{N}}^C)}]} \sum_m \left\{ \frac{\langle N,l|\hat{c}_i|N+1,m\rangle\langle N+1,m|\hat{c}_j^\dagger|N,l\rangle}{E + \mathcal{E}_l - \mathcal{E}_m - i\delta} \right.$$

$$\left. + \frac{\langle N,l|\hat{c}_j^\dagger|N-1,m\rangle\langle N-1,m|\hat{c}_i|N,l\rangle}{E - \mathcal{E}_l + \mathcal{E}_m - i\delta} \right\} \tag{3.214}$$

$$= \frac{1}{\text{Tr}[e^{-\beta(\hat{\mathcal{H}}^C - \mu^C \hat{\mathcal{N}}^C)}]}$$

$$\sum_{lm} \left\{ \langle N,l|e^{-\beta(\hat{\mathcal{H}}^C - \mu^C \hat{\mathcal{N}}^C)}|N,l\rangle \frac{\langle N,l|\hat{c}_i|N+1,m\rangle\langle N+1,m|\hat{c}_j^\dagger|N,l\rangle}{E + \mathcal{E}_l - \mathcal{E}_m - i\delta} \right.$$

$$\left. + \langle N,l|e^{-\beta(\hat{\mathcal{H}}^C - \mu^C \hat{\mathcal{N}}^C)}|N,l\rangle \frac{\langle N,l|\hat{c}_j^\dagger|N-1,m\rangle\langle N-1,m|\hat{c}_i|N,l\rangle}{E - \mathcal{E}_l + \mathcal{E}_m - i\delta} \right\}. \tag{3.215}$$

We consider the only first term,

$$\sum_{lm} \langle N,l|e^{-\beta(\hat{\mathcal{H}}^C - \mu^C \hat{\mathcal{N}}^C)}|N,l\rangle \frac{\langle N,l|\hat{c}_i|N+1,m\rangle\langle N+1,m|\hat{c}_j^\dagger|N,l\rangle}{E + \mathcal{E}_l - \mathcal{E}_m - i\delta}$$

$$= \sum_{lm} \langle N,l|e^{-\beta(\hat{\mathcal{H}}^C - \mu^C \hat{\mathcal{N}}^C)}|N,l\rangle \frac{\langle N+1,m|\hat{c}_j^\dagger|N,l\rangle\langle N,l|\hat{c}_i|N+1,m\rangle}{E + \mathcal{E}_l - \mathcal{E}_m - i\delta}$$

$$= \sum_{lm} \langle N-1,l|e^{-\beta(\hat{\mathcal{H}}^C - \mu^C \hat{\mathcal{N}}^C)}|N-1,l\rangle \frac{\langle N,m|\hat{c}_j^\dagger|N-1,l\rangle\langle N-1,l|\hat{c}_i|N,m\rangle}{E + \mathcal{E}_l - \mathcal{E}_m - i\delta}$$

$$= \sum_{lm} \langle N-1,m|e^{-\beta(\hat{\mathcal{H}}^C - \mu^C \hat{\mathcal{N}}^C)}|N-1,m\rangle \frac{\langle N,l|\hat{c}_j^\dagger|N-1,m\rangle\langle N-1,m|\hat{c}_i|N,l\rangle}{E - \mathcal{E}_l + \mathcal{E}_m - i\delta}. \tag{3.216}$$

Inserting Eq. (3.216) to Eq. (3.215) we have

$$g_{ij}^a(E) = \frac{1}{\text{Tr}[e^{-\beta(\hat{\mathcal{H}}^C - \mu^C \hat{\mathcal{N}}^C)}]}$$

$$\sum_{lm} \left\{ \left(e^{-\beta(\mathcal{E}_m - \mu^C(N-1))} + e^{-\beta(\mathcal{E}_l - \mu^C N)} \right) \frac{\langle N,l|\hat{c}_j^\dagger|N-1,m\rangle\langle N-1,m|\hat{c}_i|N,l\rangle}{E - \mathcal{E}_l + \mathcal{E}_m - i\delta} \right\}. \tag{3.217}$$

In the similar way, we obtain

$$g_{ij}^r(E) = \frac{1}{\text{Tr}[e^{-\beta(\hat{\mathcal{H}}^C - \mu^C \hat{\mathcal{N}}^C)}]}$$

$$\sum_{lm} \left\{ \left(e^{-\beta(\mathcal{E}_m - \mu^C(N-1))} + e^{-\beta(\mathcal{E}_l - \mu^C N)} \right) \frac{\langle N, l|\hat{c}_j^\dagger|N-1, m\rangle \langle N-1, m|\hat{c}_i|N, l\rangle}{E - \mathcal{E}_l + \mathcal{E}_m + i\delta} \right\},$$

$$\tag{3.218}$$

$$g_{ij}^k(E) = (1 - 2f(E))(g_{ij}^r(E) - g_{ij}^a(E)), \tag{3.219}$$

where the relation $1 - e^{-\beta(E - \mu^C)} = (1 - 2f(E))(1 + e^{-\beta(E - \mu^C)})$ has been used.

When we assume that there is no Coulomb interaction between electrons, the Green functions become more simple form. For example, the eigenstate $|N = 3, l\rangle$ where the α-th, β-th, and γ-th energy levels are filled with electrons is written as follows,

$$|3, l\rangle = \hat{a}_\alpha^\dagger \hat{a}_\beta^\dagger \hat{a}_\gamma^\dagger |0\rangle, \qquad (\alpha < \beta < \gamma) \tag{3.220}$$

where the operator $\hat{a}_m^\dagger$ creates an electron at m-th energy level with energy ε_m, and $|0\rangle$ is a vacuum state. The eigenenergy $\mathcal{E}_l$ for the state becomes $\varepsilon_\alpha + \varepsilon_\beta + \varepsilon_\gamma$. The orbital for the α-th energy level is written in the energy picture as follows,

$$|\alpha\rangle \equiv \hat{a}_\alpha^\dagger |0\rangle. \tag{3.221}$$

On the other hand, the orbital is also written in the site picture as follows,

$$|\alpha\rangle \equiv \sum_n \chi_n^\alpha \hat{c}_n^\dagger |0\rangle, \tag{3.222}$$

where χ_n^α is the amplitude of the α-th wavefunction at n-th site. A comparison of Eqs. (3.221) and (3.222) yields

$$\hat{a}_\alpha^\dagger = \sum_n \chi_n^\alpha \hat{c}_n^\dagger. \tag{3.223}$$

We can carry out $\langle 2, m|\hat{c}_i|3, l\rangle$ with aid of Eq. (3.223),

$$\langle 2, m|\hat{c}_i|3, l\rangle = \langle 0|\hat{a}_\eta \hat{a}_\xi \hat{c}_i \hat{a}_\alpha^\dagger \hat{a}_\beta^\dagger \hat{a}_\gamma^\dagger |0\rangle$$

$$= \langle \hat{a}_\eta \hat{a}_\beta^\dagger \rangle \langle \hat{a}_\xi \hat{a}_\alpha^\dagger \rangle \langle \hat{c}_i \hat{a}_\gamma^\dagger \rangle - \langle \hat{a}_\eta \hat{a}_\gamma^\dagger \rangle \langle \hat{a}_\xi \hat{a}_\alpha^\dagger \rangle \langle \hat{c}_i \hat{a}_\beta^\dagger \rangle + \langle \hat{a}_\eta \hat{a}_\gamma^\dagger \rangle \langle \hat{a}_\xi \hat{a}_\beta^\dagger \rangle \langle \hat{c}_i \hat{a}_\alpha^\dagger \rangle$$

$$= \delta_{\eta\beta} \delta_{\xi\alpha} \langle \hat{c}_i \hat{a}_\gamma^\dagger \rangle - \delta_{\eta\gamma} \delta_{\xi\alpha} \langle \hat{c}_i \hat{a}_\beta^\dagger \rangle + \delta_{\eta\gamma} \delta_{\xi\beta} \langle \hat{c}_i \hat{a}_\alpha^\dagger \rangle$$

$$= \delta_{\eta\beta} \delta_{\xi\alpha} \chi_i^\gamma - \delta_{\eta\gamma} \delta_{\xi\alpha} \chi_i^\beta + \delta_{\eta\gamma} \delta_{\xi\beta} \chi_i^\alpha. \tag{3.224}$$

We do similar calculations about all eigenstates and obtain the following simple form of Green functions,

$$g_{ij}^a(E) = \sum_n \frac{\chi_j^{n*} \chi_i^n}{E - \varepsilon_n - i\delta}, \tag{3.225}$$

$$g_{ij}^r(E) = \sum_n \frac{\chi_j^{n*} \chi_i^n}{E - \varepsilon_n + i\delta}, \tag{3.226}$$

$$g_{ij}^k(E) = (1 - 2f(E))(g_{ij}^r(E) - g_{ij}^a(E)), \tag{3.227}$$

where the summation runs over the all energy levels.

3.5.7　Green functions for the joint system

We have already obtained the Green functions for the isolated electrodes and the Kagomé-lattice chain in the previous subsection. To calculate the electronic current through the Kagomé-lattice chain by using Eq. (3.142), we must obtain the Keldysh Green functions G_{01}^{k} and G_{10}^{k} for the joint system which consists of the electrodes and the chain. Then the Dyson equations show that it is necessary to obtain the Green functions G_{mn}^{l} in order to calculate G_{01}^{k} and G_{10}^{k} ($l = a, r, k; m(n) = 0, 1, N, N + 1$). Therefore, the following contracted matrix forms of the Green functions and the self-energies should be considered instead of Eqs. (3.122)-(3.124),

$$
\mathbf{G}^{a} = \begin{bmatrix}
G_{00}^{a} & G_{01}^{a} & G_{0N}^{a} & G_{0\ N+1}^{a} \\
G_{10}^{a} & G_{11}^{a} & G_{1N}^{a} & G_{1\ N+1}^{a} \\
G_{N0}^{a} & G_{N1}^{a} & G_{NN}^{a} & G_{N\ N+1}^{a} \\
G_{N+1\ 0}^{a} & G_{N+1\ 1}^{a} & G_{N+1\ N}^{a} & G_{N+1\ N+1}^{a}
\end{bmatrix},
\tag{3.228}
$$

$$
\mathbf{g}^{a} = \begin{bmatrix}
g_{00}^{a} & 0 & 0 & 0 \\
0 & g_{11}^{a} & g_{1N}^{a} & 0 \\
0 & g_{N1}^{a} & g_{NN}^{a} & 0 \\
0 & 0 & 0 & g_{N+1\ N+1}^{a}
\end{bmatrix},
\tag{3.229}
$$

$$
\mathbf{\Sigma}^{a} = \begin{bmatrix}
0 & -t' & 0 & 0 \\
-t' & 0 & 0 & 0 \\
0 & 0 & 0 & -t' \\
0 & 0 & -t' & 0
\end{bmatrix}.
\tag{3.230}
$$

The retarded Green functions and the self-energies are obtained similarly. Furthermore, using the Dyson equations (3.125) and (3.126), we have the advanced and the retarded Green functions of the joint system as follows,

$$
\mathbf{G}^{a} = (\mathbf{I} - \mathbf{g}^{a}\mathbf{\Sigma}^{a})^{-1}\mathbf{g}^{a},
\tag{3.231}
$$

$$
\mathbf{G}^{r} = (\mathbf{I} - \mathbf{g}^{r}\mathbf{\Sigma}^{r})^{-1}\mathbf{g}^{r},
\tag{3.232}
$$

where $\mathbf{I}$ is the 4×4 unit matrix. The Keldysh Green functions obey the Dyson equation (3.127). We have the following equation from Eq. (3.127),

$$
\mathbf{G}^{k} = (\mathbf{I} - \mathbf{g}^{r}\mathbf{\Sigma}^{r})^{-1}\mathbf{g}^{k}(\mathbf{I} + \mathbf{g}^{a}\mathbf{\Sigma}^{a}).
\tag{3.233}
$$

Furthermore, using Eqs. (3.231) and (3.232), we obtain

$$
\mathbf{G}^{k} = \mathbf{G}^{r}\mathbf{g}^{r-1}\mathbf{g}^{k}\mathbf{g}^{a-1}\mathbf{G}^{a}.
\tag{3.234}
$$

When the i- and j-th sites are included in the Kagomé-lattice chain, the (i,j)-component of $\mathbf{g}^{r-1}\mathbf{g}^{k}\mathbf{g}^{a-1}$ is written with aid of Eq. (3.227) as follows,

$$
\{\mathbf{g}^{r-1}\mathbf{g}^{k}\mathbf{g}^{a-1}\}_{ij} = (1 - 2f)\{\mathbf{g}^{r-1}(\mathbf{g}^{r} - \mathbf{g}^{a})\mathbf{g}^{a-1})\}_{ij}
$$
$$
= (1 - 2f)(\{\mathbf{g}^{a-1}\}_{ij} - \{\mathbf{g}^{r-1}\}_{ij}).
\tag{3.235}
$$

Equation (3.235) is calculated as follows, by using Eqs. (3.225) and (3.226),

$$
\{\mathbf{g}^{r-1}\mathbf{g}^{k}\mathbf{g}^{a-1}\}_{ij} = (1 - 2f)(\{\mathbf{g}^{a-1}\}_{ij} - \{\mathbf{g}^{r-1}\}_{ij}) \propto (1 - 2f)\,\delta \to 0.
\tag{3.236}
$$

It means that the Fermi energy of the isolated Kagomé-lattice chain doesn't contribute the electronic current. On the other hand, When the $i \, (= j)$-th sites are included in the left or the right electrode, equation (3.235) is calculated as follows,

$$\{\mathbf{g}^{r-1}\mathbf{g}^k\mathbf{g}^{a-1}\}_{ii} = (1 - 2f)(\{\mathbf{g}^{a-1}\}_{ij} - \{\mathbf{g}^{r-1}\}_{ii})$$

$$= \begin{cases} (1 - 2f^L)((g_{00}^a)^{-1} - (g_{00}^r)^{-1}) & \text{for } i = 0, \\ (1 - 2f^R)((g_{N+1 \, N+1}^a)^{-1} - (g_{N+1 \, N+1}^r)^{-1}) & \text{for } i = N + 1. \end{cases}$$

$$(3.237)$$

Thus, we obtain the Keldysh Green functions for the joint system,

$$G_{01}^k = (1 - 2f^L)G_{00}^r((g_{00}^a)^{-1} - (g_{00}^r)^{-1})G_{01}^a$$
$$+ (1 - 2f^R)G_{0 \, N+1}^r((g_{N+1 \, N+1}^a)^{-1} - (g_{N+1 \, N+1}^r)^{-1})G_{N+1 \, 1}^a, \quad (3.238)$$
$$G_{10}^k = (1 - 2f^L)G_{10}^r((g_{00}^a)^{-1} - (g_{00}^r)^{-1})G_{00}^a$$
$$+ (1 - 2f^R)G_{1 \, N+1}^r((g_{N+1 \, N+1}^a)^{-1} - (g_{N+1 \, N+1}^r)^{-1})G_{N+1 \, 0}^a. \quad (3.239)$$

In this paper, first, we calculated numerically Eqs. (3.231)-(3.232) and obtained the G^a and G^r, and then we calculated numerically the G^k using Eqs. (3.238) and (3.239). Finally, the electronic currents are calculated using Eq. (3.142)

3.6   Appendix II; Additional data

Source-Drain-voltage dependence of current peaks

We investigate the source-drain-voltage dependence of the electronic-current vs gate-voltage characteristics of the four-plaquette-length Kagomé-lattice chain without an external electric field. The calculated results for various source-drain voltages are shown in Figs. 3.21(a)-(c).
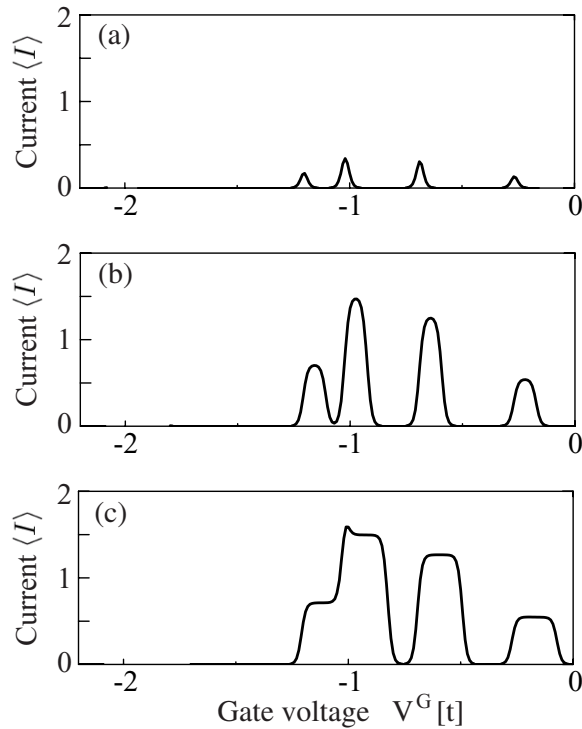

Figure 3.21: The calculated electronic-current vs gate-voltage characteristics of the four-plaquette-length Kagomé-lattice chain without an external electric field at the $V^{sd} =$ (a)0.01t, (b)0.1t, (c)0.2t.

Temperature dependence of current peaks

We investigate the temperature dependence of the electronic-current vs gate-voltage characteristics of the four-plaquette-length Kagomé-lattice chain. The calculated results for various tempretures voltages are shown in Fig. 3.22.
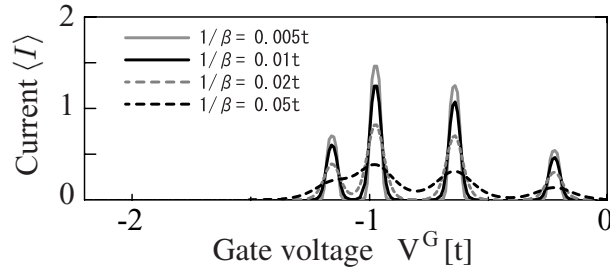

Figure 3.22: The calculated electronic-current vs gate-voltage characteristics of the four-plaquette-length Kagomé-lattice chain at the various temperatures, $\beta = 200t$, $\beta = 100t$, $\beta = 50t$, and $\beta = 20t$. An external filed isn't applied to the systems.

Electron transfer energy t^L dependence of current peaks

Figure 3.23 shows the transfer energy t^L $(= t^R)$ dependence of the current peaks of four-plaquette Kagomé-lattice chains.
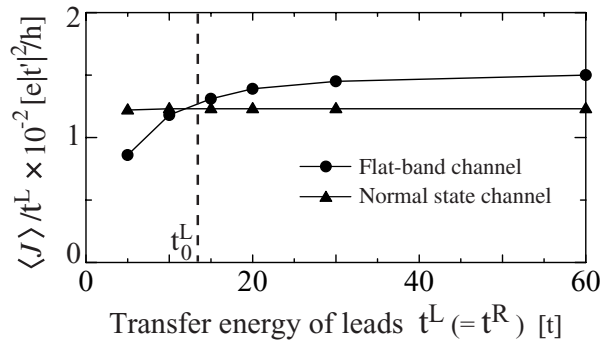

Figure 3.23: The transfer energy of electrode dependence of the current. Note that the longitudinal axis represents the value, which is divided current by transfer energy t^L. The broken line represents the threshold of the cancellation among the flat-band channels.

Coupling magnitude dependence of current peaks

Figure 3.24 shows the coupling magnitude dependence of the current peaks of (a) two- and (b) four-plaquette Kagomé-lattice chains. The current magnitudes of flat-band channels are greatly changed by the coupling magnitude.
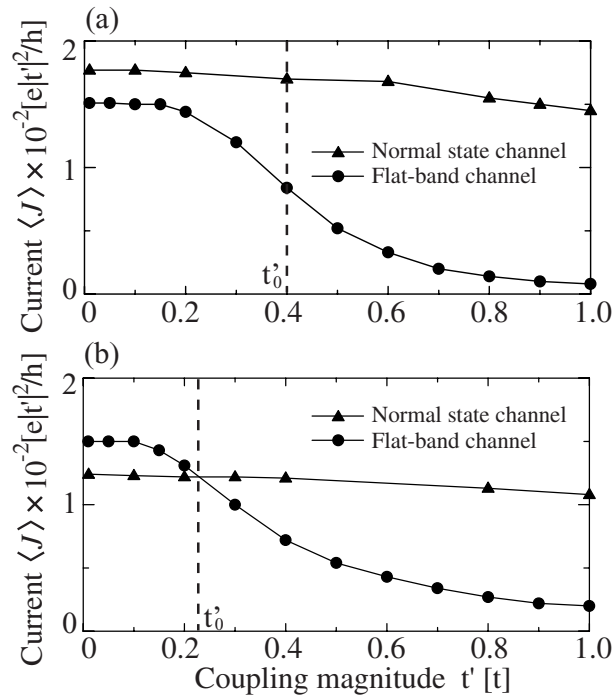

Figure 3.24: The calculated current peak height of normal state channel and flat-band state channel vs. coupling magnitude curves in the case of (a)two- and (b)four-plaquette length Kagomé lattice chains. The broken line represents the threshold of the cancellation among the flat-band channels.

Eigenstates of normal channels

Figure 3.25 shows the normal states of four-plaquette Kagomé-lattice chain. These states are arranged in energetic order.
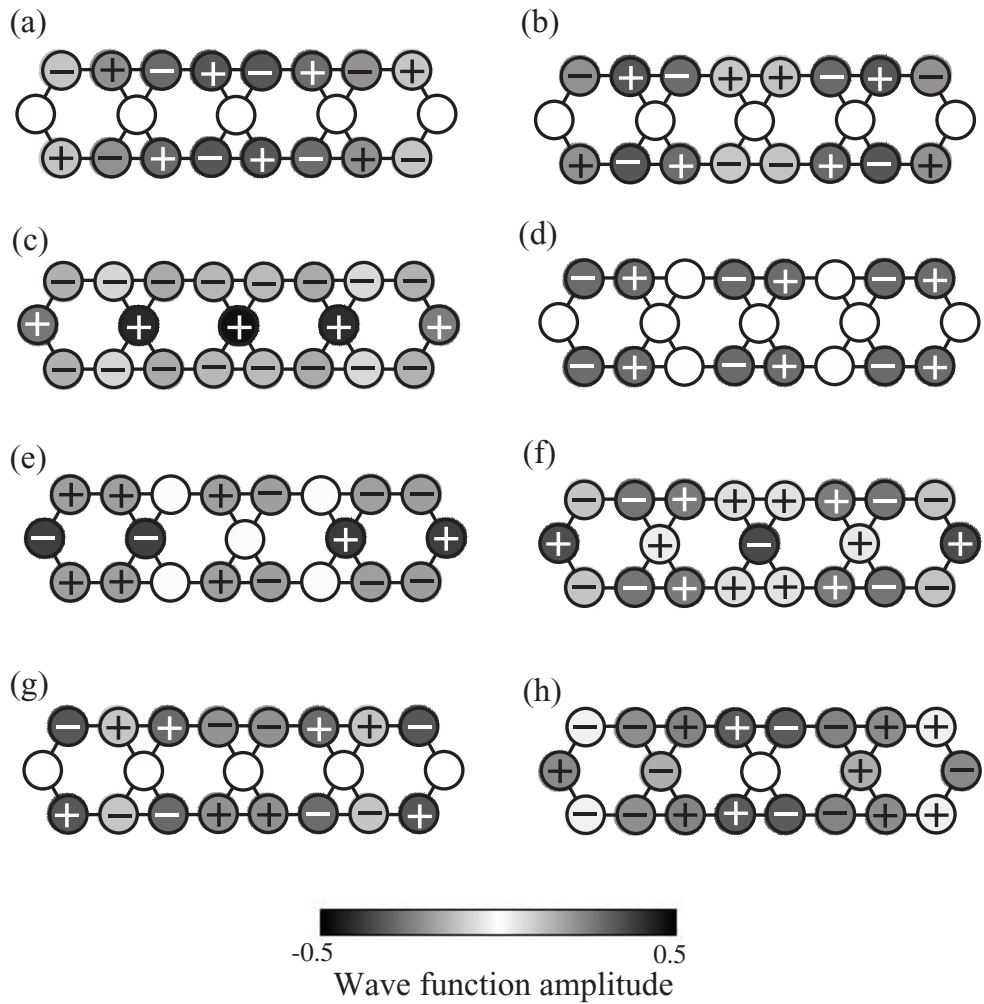

Figure 3.25: Normal states of four-plaquette Kagomé-lattice chain. These states are arranged in energetic order.

Chapter 4

Time-dependent current in Nanostructure systems

4.1   Purpose

Recently, designs of novel electronic devices using nanometer scale semiconductor structures and molecules have been attempted from both experiment and theory sides. When electronic currents through such nanostructures are calculated, it is often assumed that the electronic states of the systems have reached steady states. However, in experiments of conductive properties in nanostructures, the energy dissipative process and the dynamics have received much attention. Considering future practical applications, it is important to clarify the transient effects.

For example, Bird and coworkers studied the time-dependent conductivity of low-dimensional semiconductors with time resolution of a few hundred picoseconds [43]. As shown in Fig. 4.1(a), a voltage pulse is applied to the input microstrip line from a pulse generator, and the output pulse is measured using the 50-Ω input of an oscilloscope. Figure 4.1(b) shows the measured output pulse. This figure shows very clearly that they were able to detect the pulse with relatively a little distortion, aside from the noticeable overshoot associated with the rising edge. The origin has not been clarified yet, and it is expected that the origin isn't understood by using the calculation method of steady current.

An another example is seen in the conductive properties of single molecule [44–47]. The advance of STM has made it possible to measure electronic current flowing through a single molecule adsorbed on metal surface. It is expected that the quantum effect appears clearly in the molecular conductive properties. The difference between semiconductor nanostructure system and the single molecular system is that the coupling magnitude between electrons and molecular vibrations in the molecular system is stronger than that in the semiconductor system. For example, Kawai and coworkers found that inelastic current injected from STM tip excites the molecular vibrations [3]. The amplitudes of vibrations are increased gradually by the current. As a result, the molecule hops or rotates on the metal surface. Figures. 4.2 show the STM images of the carbon monoxide (CO) molecules adsorbed on the Pd(110) surface. The CO molecule marked "a" in Fig. 4.2A was dosed with tunneling electrons from STM tip for one second. The tunneling elec-
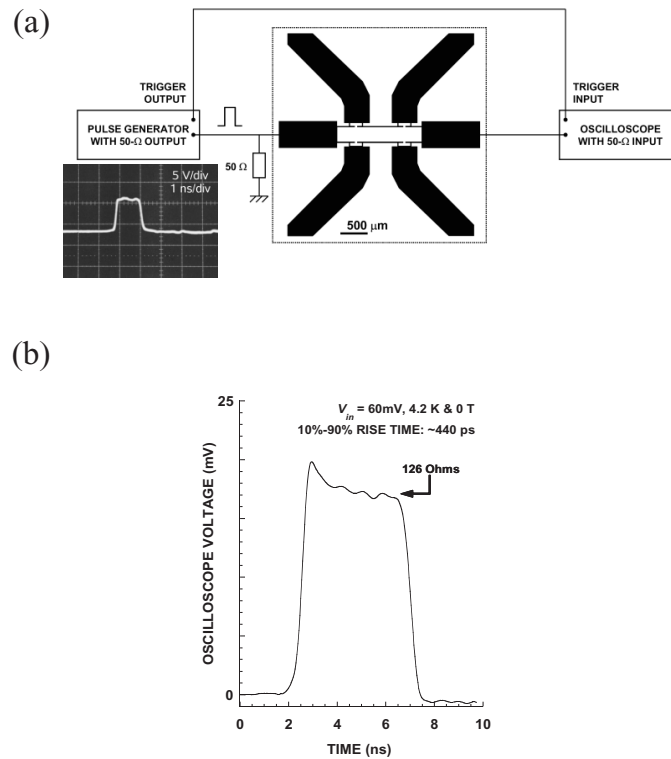
(a)

(b)

Figure 4.1: (a) Schematic diagram illustrating the instrumentation used in the pulsed measurements of the GaAs/AlGaAs Hall bar. The solid-black lines indicate the microstrip lines on top of the semiconductor die, which connect to the Ohmic contacts of the Hall bar. In a typical measurement, only two of these lines are used and the others are left unconnected [43]. Inset is the input pulse. (b) Measurement of the pulse-response of the GaAs/AlGaAs 2DEG at 4.2 K. The input pulse in this case has a rise time of 60 picoseconds, a fall time of about 250 picoseconds, and a duration of 4 picoseconds [43].
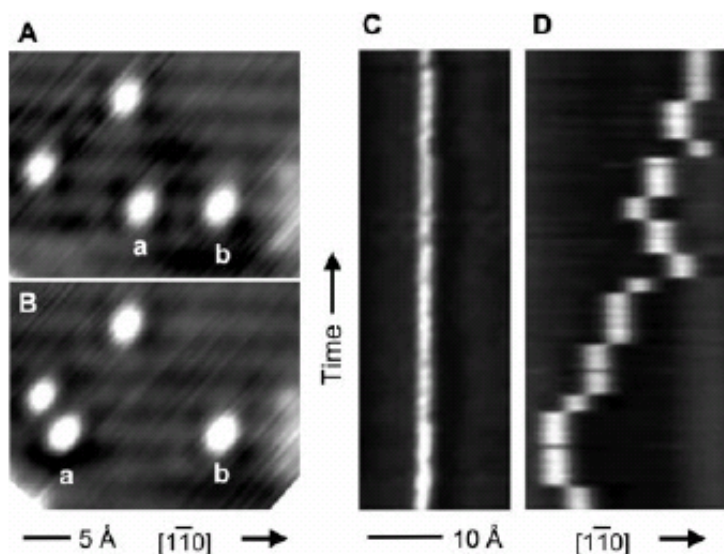
Figure 4.2: (A and B) STM images (31 Å by 25 Å, tunneling current 1 nA, sample bias voltage 50 mV) of four CO molecules on Pd(110) [3]. Images are (A) before and (B) after dosing tunneling electrons on the target molecule "a". (C and D) One-dimensional dose-and-scan method images for an isolated CO on Pd(110). Sample bias voltage for electron dosing is (C) 200 mV and (D) 300 mV. Totally 48 sequences are executed on both cases. Anisotropic hopping along the $[1\bar{1}0]$ direction with a unit of Pd lattice (2.75 Å) is clearly visible in the right panel.

trons give the energy to the molecular vibrations. The molecule "a" has jumped three Pd lattice spacing to the left along the $[1\bar{1}0]$ direction as shown in Fig. 4.2B. Therefore, these are time dependent phenomena with energy dissipative process.

In order to understand these situations, we should calculate time dependent electronic current without assumption that electronic current reaches a steady state [48, 49]. However, the calculation method of time dependent current has not yet been established. Thus, the purpose of this study is to propose the calculation method of time-dependent current.

4.2 System with energy and particle number conservation

In this section, we review the characteristics of the motion of electrons in closed systems where the energies and the particle numbers are conserved [50]. As an example, we consider the two-room system as shown in Fig. 4.3. The left room has a discrete energy level E_L, and the right room has a discrete energy level E_R. The two rooms are connected, and the electron transfer energy is written as $-v$. The probability amplitude that we find the electron in the left room is obtained with $\phi_L(t)$. Similarly, we define $\phi_R(t)$ which represents the probability amplitude

of electron in the right room. We treat electrons as spinless fermions. Then, the Schrödinger equation is written as follows,

$$i\hbar \frac{d}{dt}|\phi(t)\rangle = \hat{\mathcal{H}}|\phi(t)\rangle, \tag{4.1}$$

where the wavefunction and the Hamiltonian are written as,

$$|\phi(t)\rangle \equiv \begin{bmatrix} \phi_R(t) \\ \phi_L(t) \end{bmatrix} \equiv \phi_R(t)|R\rangle + \phi_L(t)|L\rangle, \tag{4.2}$$

$$\hat{\mathcal{H}} \equiv \begin{bmatrix} E_R & -v \\ -v & E_L \end{bmatrix}. \tag{4.3}$$

We write the electronic state at the initial time t_0 as $|\phi(t_0)\rangle$. When the Hamiltonian is independent of time, the electronic state at time $t(> t_0)$ is related to the initial electronic state $|\phi(t_0)\rangle$, by solving Eq. (4.1) as

$$|\phi(t)\rangle = \exp\left(-i\frac{\hat{\mathcal{H}}}{\hbar}(t - t_0)\right)|\phi(t_0)\rangle. \tag{4.4}$$

Especially, if the initial electronic state becomes an eigenstate of the Hamiltonian, Eq. (4.4) is rewritten as follows,

$$|\phi(t)\rangle = \exp\left(-i\frac{E}{\hbar}(t - t_0)\right)|E\rangle, \tag{4.5}$$

where $|E\rangle$ is an eigenstate which has an eigenvalue E. Then we obtain the probability that we find the electron in the right room as

$$\left|\langle R|\phi(t)\rangle\right|^2 = \left|\langle R|E\rangle\right|^2. \tag{4.6}$$

This result shows that the eigenstate of the system is a steady state. Then, we consider following two cases.

Case of $E_L = E_R = E_0$

First, we consider the case that two rooms have the same energy level E_0. In this case, the eigenenergies and the eigenfunctions of the Hamiltonian $\hat{\mathcal{H}}$ are obtained as

$$E_\pm = E_0 \pm v, \tag{4.7}$$

$$|E_\pm\rangle = \frac{1}{\sqrt{2}} \begin{bmatrix} 1 \\ \mp 1 \end{bmatrix} = \frac{1}{\sqrt{2}}|R\rangle \mp \frac{1}{\sqrt{2}}|L\rangle. \tag{4.8}$$

Using Eq. (4.8), we have following equations,

$$|R\rangle = +\frac{1}{\sqrt{2}}|E_+\rangle + \frac{1}{\sqrt{2}}|E_-\rangle, \tag{4.9}$$

$$|L\rangle = -\frac{1}{\sqrt{2}}|E_+\rangle + \frac{1}{\sqrt{2}}|E_-\rangle. \tag{4.10}$$

We assume that there is an electron in the only right room at the initial time t_0. Then the electronic state at any time is obtained using Eqs. (4.4) and (4.9),

$$|\phi(t)\rangle = \exp\left(-i\frac{\hat{\mathcal{H}}}{\hbar}(t - t_0)\right)|R\rangle \tag{4.11}$$

$$= \exp\left(-i\frac{\hat{\mathcal{H}}}{\hbar}(t - t_0)\right)\left(\frac{1}{\sqrt{2}}|E_+\rangle + \frac{1}{\sqrt{2}}|E_-\rangle\right) \tag{4.12}$$

$$= \frac{1}{\sqrt{2}}\exp\left(-i\frac{E_+}{\hbar}(t - t_0)\right)|E_+\rangle + \frac{1}{\sqrt{2}}\exp\left(-i\frac{E_-}{\hbar}(t - t_0)\right)|E_-\rangle. \tag{4.13}$$

It shows that the time evolution of the system can be expressed by the superposition of eigenstates $|E_{+(-)}\rangle$ each vibrating at frequency $E_{+(-)}/\hbar$. Using Eq. (4.8), Eq. (4.13) can be rewritten as

$$|\phi(t)\rangle = e^{-i\frac{E_0}{\hbar}t}\left\{\cos\left(\frac{v}{\hbar}t\right)|R\rangle + i\sin\left(\frac{v}{\hbar}t\right)|L\rangle\right\}. \tag{4.14}$$

The density matrix of the system is defined as follows,

$$\hat{\sigma}(t) \equiv |\phi(t)\rangle\langle\phi(t)|. \tag{4.15}$$

The probability that an electron is in the right room is obtained by using the density matrix,

$$\langle R|\hat{\sigma}(t)|R\rangle \equiv \langle R|\phi(t)\rangle\langle\phi(t)|R\rangle \tag{4.16}$$

$$= \cos^2\left(\frac{v}{\hbar}t\right) \tag{4.17}$$

$$= \frac{1}{2}\left\{1 + \cos\left(\frac{2v}{\hbar}t\right)\right\}. \tag{4.18}$$

Thus, the electron shuttles between two rooms with a frequency, $2v/\hbar$. The frequency corresponds to the energy difference between two eigenenergies,

$$\frac{E_+ - E_-}{\hbar} = \frac{2v}{\hbar}. \tag{4.19}$$

The motion of the electron is expressed by the interference of the eigenstates with the different frequencies. Figure 4.4 is the calculation results of the probability that an electron is in the right room. Here, E_L and E_R are set to 0, and the transfer energy v is 1. The electron in the right room at initial time moves completely into the left room after time $\pi\hbar/(2v)$.

Case of $E_L < E_R$

Next, we consider the case that two rooms have the different energy levels. When the energy level of the left room is different from that of the right room, the eigenenergies and the eigenfunctions of the Hamiltonian $\hat{\mathcal{H}}$ are obtained as

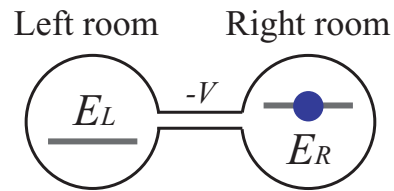$$E_\pm = \frac{E_R + E_L}{2} \pm \Delta, \tag{4.20}$$

Left room   Right room

Figure 4.3: Schematic picture of two-room system. The left and right rooms have discrete energy levels, E_L and E_R, respectively. The two rooms are connected.
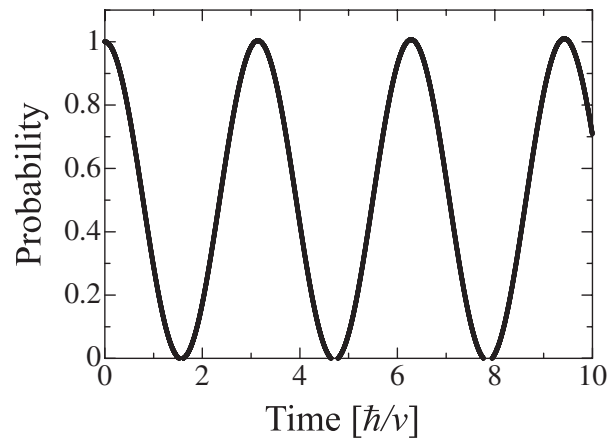

Figure 4.4: Calculated probability that electron is in the right room as a function of time. The eigenenergies of the left room and right room are set to zero. The electron transfer energy between two rooms is unity.

$$|E_\pm\rangle = \frac{1}{\sqrt{v^2 + [(E_R - E_L)/2 \mp \Delta]^2}} \left[\begin{array}{c} v \\ \frac{E_R - E_L}{2} \mp \Delta \end{array} \right], \tag{4.21}$$

where the quantity Δ has been introduced as,

$$\Delta \equiv \sqrt{\left(\frac{E_R - E_L}{2} \right)^2 + v^2}. \tag{4.22}$$

To simplify, it is assumed that the energy difference between E_R and E_L is much larger than the transfer energy v, and we neglect the term over the second order of $v/(E_R - E_L)$. Then we have the following energy eigenvalues,

$$E_+ \simeq \frac{E_R + E_L}{2} + \frac{E_R - E_L}{2} = E_R, \tag{4.23}$$

$$E_- \simeq \frac{E_R + E_L}{2} - \frac{E_R - E_L}{2} = E_L. \tag{4.24}$$

On the other hand, the eigenfunctions are also given as,

$$|E_+\rangle \simeq |R\rangle - \frac{v}{E_R - E_L}|L\rangle, \tag{4.25}$$

$$|E_-\rangle \simeq |L\rangle + \frac{v}{E_R - E_L}|R\rangle. \tag{4.26}$$

We can rewrite this equation as follows,

$$|R\rangle \simeq |E_+\rangle + \frac{v}{E_R - E_L}|E_-\rangle, \tag{4.27}$$

$$|L\rangle \simeq |E_-\rangle - \frac{v}{E_R - E_L}|E_+\rangle. \tag{4.28}$$

Using Eqs. (4.25)-(4.27), when an electron was in the right room at initial time, t_0, the wavefunction at time, $t \, (> t_0)$, is given by

$$|\phi(t)\rangle = \exp\left(-i\frac{\hat{\mathcal{H}}}{\hbar}(t - t_0) \right)|R\rangle \tag{4.29}$$

$$\simeq \exp\left(-i\frac{E_+}{\hbar}(t - t_0) \right)|E_+\rangle + \frac{v}{E_R - E_L} \exp\left(-i\frac{E_-}{\hbar}(t - t_0) \right)|E_-\rangle \tag{4.30}$$

$$\simeq \exp\left(-i\frac{E_+}{\hbar}(t - t_0) \right)|R\rangle$$
$$+ i\frac{2v}{E_R - E_L} \exp\left(-i\frac{E_+ + E_-}{2\hbar}(t - t_0) \right) \sin\left(\frac{E_+ - E_-}{2\hbar}(t - t_0) \right)|L\rangle. \tag{4.31}$$

Equation (4.30) shows that an origin of the electron motion is the interference between the eigenfunctions $|E_+\rangle$ and $|E_-\rangle$ vibrating with frequencies, $E_+/\hbar$ and $E_-/\hbar$, respectively. We obtain the probability that an electron is in the left room at time, t, by using the density matrix,

$$\langle L|\hat{\sigma}(t)|L\rangle = \langle L|\phi(t)\rangle\langle\phi(t)|L\rangle \tag{4.32}$$

$$\simeq \left(\frac{2v}{E_R - E_L} \right)^2 \sin^2\left(\frac{E_+ - E_-}{2\hbar}t \right) \tag{4.33}$$

$$= \left(\frac{2v}{E_R - E_L} \right)^2 \frac{1}{2}\left\{ 1 - \cos\left(\frac{E_+ - E_-}{\hbar}t \right) \right\}. \tag{4.34}$$
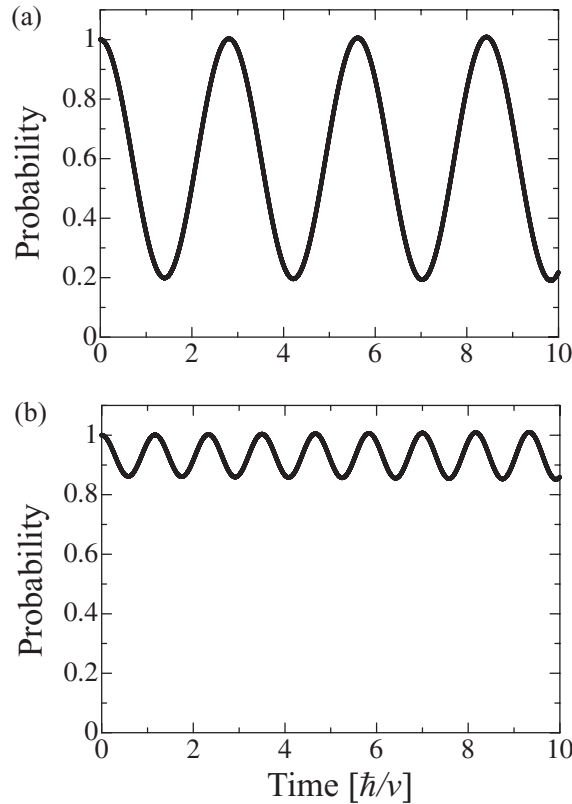
Figure 4.5: Calculated probability that electron is in the right room as a function of time. The right room have the eigenenergies, (a) $E_R = 1$ and (b) $E_R = 5$, respectively, whereas the eigenenergies of left room is $E_L = 0$. The electron transfer energy between two rooms is unity.

The electron shuttles between the right room and the left room with a frequency, $(E_+ - E_-)/\hbar$. However, the probability amplitude, $(2v/(E_R - E_L))^2$, is very small. Thus, the electron in the right room almost stays in the right room. Figures 4.5(a) and 4.5(b) are the calculated probabilities that an electron is in the right room under $E_L = 1$, $E_R = 0$, $v = 1$ and $E_L = 5$, $E_R = 0$, $v = 1$, respectively. We can confirm that when the energy difference between E_R and E_L becomes much larger than the transfer energy v, the period of the probability vibration becomes shorter and the magnitudes of amplitudes decrease.

   These calculation results show that even if the two rooms have different eigenenergies, electrons can not flow one-way from the high-energy room to the low-energy room. This is because the system is a closed system with respect to the energy and the particle number in the density matrix method. However, we must employ the opened systems regarding the energy and the particle number to describe the nonequilibrium states such as the electronic current flowing one-way from one electrode to another electrode. The density matrix method has advantage to calculate time development of the systems. Thus, we employ the hybrid method of the density matrix method and the projection operator method, which is explained in detail in the next section.

4.3 Model and Calculation method of time-dependent current

In this work, we investigate the time evolution of the system which consists of two bulk electrodes and a nanostructure by using the simple tight-binding model. The nanostructure (A) has the discrete energy levels ε_n^A, whereas the two bulk electrodes (B and C) have the continuous energy states, ε_k^B and ε_k^C, which are labeled with wavevector k, respectively. The Hamiltonian of the joint system of electrodes and a nanostructure is written as

$$\hat{\mathcal{H}} = \hat{\mathcal{H}}_0 + \hat{\mathcal{H}}_1, \tag{4.35}$$

where $\hat{\mathcal{H}}_0$ is the Hamiltonian of the isolated electrodes and an isolated nanostructure, and is defined as follows,

$$\hat{\mathcal{H}}_0 \equiv \hat{\mathcal{H}}^A + \hat{\mathcal{H}}^B + \hat{\mathcal{H}}^C \tag{4.36}$$

$$= \sum_n \varepsilon_n^A \hat{a}_n^\dagger \hat{a}_n + \sum_k \varepsilon_k^B \hat{b}_k^\dagger \hat{b}_k + \sum_k \varepsilon_k^C \hat{c}_k^\dagger \hat{c}_k. \tag{4.37}$$

Here, $\hat{a}_n$ is an annihilation operator of an electron in n-th energy level of the nanostructure. $\hat{b}_k$ and $\hat{c}_k$ are annihilation operators of an electron with wavevector, k, in the electrode B and C, respectively. We have treated electrons as spinless fermions in this work. The Hamiltonian $\hat{\mathcal{H}}_1$ represents the junction between the nanostructure and the electrodes,

$$\hat{\mathcal{H}}_1 = -t^{AB} \sum_{n,k} (\hat{a}_n^\dagger \hat{b}_k + \hat{b}_k^\dagger \hat{a}_n) - t^{AC} \sum_{n,k} (\hat{a}_n^\dagger \hat{c}_k + \hat{c}_k^\dagger \hat{a}_n), \tag{4.38}$$

where the quantity t^{AB} represents the electron transfer energy between the nanostructure A and the electrode B. Similarly, t^{AC} represents the transfer energy between the nanostructure A and the electrode C.

Density matrix method

The density matrix of the joint system is defined by Eq. (3.62). The time evolution of the density matrix obeys the following Liouville equation,

$$\frac{\partial \hat{\rho}(t)}{\partial t} = \frac{1}{i\hbar}[\hat{\mathcal{H}}, \hat{\rho}(t)] \equiv i\hat{\mathcal{L}}\hat{\rho}(t), \tag{4.39}$$

where $\hat{\mathcal{L}}$ is the Liouville operator and is defined as $\hat{\mathcal{L}} \bullet \equiv -1/\hbar[\hat{\mathcal{H}}, \bullet]$. The $\bullet$ represents any operator. Corresponding to Eqs. (4.35) and (4.36), $\hat{\mathcal{L}}$ is resolved as

$$\hat{\mathcal{L}} = \hat{\mathcal{L}}_0 + \hat{\mathcal{L}}_1 \tag{4.40}$$

$$= \hat{\mathcal{L}}_A + \hat{\mathcal{L}}_B + \hat{\mathcal{L}}_C + \hat{\mathcal{L}}_1, \tag{4.41}$$

where $\hat{\mathcal{L}}_i \bullet \equiv -1/\hbar[\hat{\mathcal{H}}_i, \bullet]$ ($i = 0, A, B, C, 1$). As shown in Sec. 4.2, the density matrix method can describe only closed systems having the energy and the particle number conservations. Thus, in order to calculate the time-dependent opened systems under nonequilibrium conditions, we apply the projection operator to the Liouville equation (4.39) [51].

Projection method

We would like to investigate the time development of the electronic states after the nanostructure is connected to the electrodes. It is expected that the electronic states of the nanostructure are changed by the connection, whereas the states of the electrodes are preserved because the system size of electrodes are much larger than that of nanostructure. Thus, we can reasonably resolve the density matrix of the joint system $\hat{\rho}(t)$ as follows,

$$\hat{\rho}(t) \rightarrow \hat{\rho}_B \hat{\rho}_C \hat{\sigma}(t), \tag{4.42}$$

where $\hat{\rho}_B$ and $\hat{\rho}_C$ are the time-independent density matrixes of the bulk electrodes, and $\hat{\sigma}(t)$ represents the time-dependent density matrix of the nanostructure in the joint system. We assume that the electronic states of electrodes (B and C) are written by the following grand canonical distribution, respectively.

$$\hat{\rho}_B = \frac{e^{-\beta(\hat{\mathcal{H}}_B - \mu_B \hat{N}_B)}}{\mathrm{Tr}_B\big[e^{-\beta(\hat{\mathcal{H}}_B - \mu_B \hat{N}_B)}\big]}, \tag{4.43}$$

$$\hat{\rho}_C = \frac{e^{-\beta(\hat{\mathcal{H}}_C - \mu_C \hat{N}_C)}}{\mathrm{Tr}_C\big[e^{-\beta(\hat{\mathcal{H}}_C - \mu_C \hat{N}_C)}\big]}. \tag{4.44}$$

Here, μ_i and $\hat{N}_i$ represent the Fermi energy and the electron number operator in electrode, respectively. The inverse temperature β is defined as $1/(k_B T)$. Tr_i means the trace over the eigenstates of the isolated electrode i ($i = B$ or C).

In order to realize the decomposition form of Eq. (4.42) from the $\hat{\rho}(t)$, we introduce the following projection operator $\hat{P}$,

$$\hat{P} \bullet \equiv \hat{\rho}_B \hat{\rho}_C \mathrm{Tr}_B \mathrm{Tr}_C \bullet . \tag{4.45}$$

The projection operator satisfies the relation $\hat{P}^2 = \hat{P}$. Furthermore another projection operator $\hat{Q}$ is defined as $(1 - \hat{P})$. When the projection operator $\hat{P}$ is applied to the density matrix $\hat{\rho}(t)$, we have the following equation,

$$\hat{P}\hat{\rho}(t) = \hat{\rho}_B \hat{\rho}_C \mathrm{Tr}_B \mathrm{Tr}_C \hat{\rho}(t) \tag{4.46}$$

$$\equiv \hat{\rho}_B \hat{\rho}_C \hat{\sigma}(t). \tag{4.47}$$

Here, the density matrix of the nanostructure in the joint system, $\hat{\sigma}(t)$, is defined by the trace of the $\hat{\rho}(t)$ over the eigenstates of all isolated electrodes,

$$\hat{\sigma}(t) \equiv \mathrm{Tr}_B \mathrm{Tr}_C \hat{\rho}(t). \tag{4.48}$$

The projected density matrix means that the electronic states of electrodes in the joint system are replaced by the time-independent grand canonical distribution. Therefore, we can consider the time-dependent opened systems under nonequilibrium states by using the Liouvile equation for the projected density matrix.

Applying the projection operators $\hat{P}$ and $\hat{Q}$ to the Liouville equation (4.39), we have

$$\frac{\partial \hat{P}\hat{\rho}(t)}{\partial t} = \hat{P}\frac{\partial \hat{\rho}(t)}{\partial t}$$
$$= \hat{P}i\hat{\mathcal{L}}\hat{P}\hat{\rho}(t) + \hat{P}i\hat{\mathcal{L}}\hat{Q}\hat{\rho}(t), \qquad (4.49)$$

$$\frac{\partial \hat{Q}\hat{\rho}(t)}{\partial t} = \hat{Q}\frac{\partial \hat{\rho}(t)}{\partial t}$$
$$= \hat{Q}i\hat{\mathcal{L}}\hat{P}\hat{\rho}(t) + \hat{Q}i\hat{\mathcal{L}}\hat{Q}\hat{\rho}(t), \qquad (4.50)$$

where $\hat{\rho}(t) = \hat{P}\hat{\rho}(t) + \hat{Q}\hat{\rho}(t)$ has been used. Using the variation of parameter method, Eq. (4.50) is solved as

$$\hat{Q}\hat{\rho}(t) = \int_{t_0}^{t} d\tau e^{(t-\tau)\hat{Q}i\hat{\mathcal{L}}}\hat{Q}i\hat{\mathcal{L}}\hat{P}\hat{\rho}(\tau) + e^{(t-t_0)\hat{Q}i\hat{\mathcal{L}}}\hat{Q}\hat{\rho}(t_0). \qquad (4.51)$$

The density matrix at initial time, t_0, is written as

$$\hat{\rho}(t_0) = \hat{\rho}_B\hat{\rho}_C\mathrm{Tr}_B\mathrm{Tr}_C\hat{\rho}(t_0), \qquad (4.52)$$

because the connection is performed just after the initial time. Inserting Eq. (4.52) to Eq. (4.51), the second term of Eq. (4.51) becomes zero. Therefore, inserting Eq. (4.51) to Eq. (4.49), we have

$$\frac{\partial \hat{P}\hat{\rho}(t)}{\partial t} = \hat{P}i\hat{\mathcal{L}}\hat{P}\hat{\rho}(t) + \hat{P}i\hat{\mathcal{L}}\int_{t_0}^{t} d\tau e^{(t-\tau)\hat{Q}i\hat{\mathcal{L}}}\hat{Q}i\hat{\mathcal{L}}\hat{P}\hat{\rho}(\tau). \qquad (4.53)$$

The first term can be rewrittn as

$$\hat{P}i\hat{\mathcal{L}}\hat{P}\hat{\rho}(t) = \hat{\rho}_B\hat{\rho}_C\mathrm{Tr}_B\mathrm{Tr}_C\{i\hat{\mathcal{L}}(\hat{\rho}_B\hat{\rho}_C\hat{\sigma}(t))\}$$
$$= \hat{\rho}_B\hat{\rho}_C\mathrm{Tr}_B\mathrm{Tr}_C\{\hat{\rho}_B\hat{\rho}_C(i\hat{\mathcal{L}}_A\hat{\sigma}(t))\} + \hat{\rho}_B\hat{\rho}_C\mathrm{Tr}_B\mathrm{Tr}_C\{(i\hat{\mathcal{L}}_B\hat{\rho}_B)\hat{\rho}_C\hat{\sigma}(t))\}$$
$$+ \hat{\rho}_B\hat{\rho}_C\mathrm{Tr}_B\mathrm{Tr}_C\{\hat{\rho}_B(i\hat{\mathcal{L}}_C\hat{\rho}_C)\hat{\sigma}(t)\} + \hat{\rho}_B\hat{\rho}_C\mathrm{Tr}_B\mathrm{Tr}_C\{i\hat{\mathcal{L}}_1(\hat{\rho}_B\hat{\rho}_C\hat{\sigma}(t))\}$$
$$= \hat{\rho}_B\hat{\rho}_C i\hat{\mathcal{L}}_A\hat{\sigma}(t). \qquad (4.54)$$

We can rewrite the second term as follows,

$$\hat{P}i\hat{\mathcal{L}}\int_{t_0}^{t} d\tau e^{(t-\tau)\hat{Q}i\hat{\mathcal{L}}}\hat{Q}i\hat{\mathcal{L}}\hat{P}\hat{\rho}(\tau) = \hat{P}i\hat{\mathcal{L}}\int_{t_0}^{t} d\tau e^{(t-\tau)\hat{Q}i\hat{\mathcal{L}}\hat{Q}}\hat{Q}i\hat{\mathcal{L}}\hat{P}\hat{\rho}(\tau)$$
$$= \hat{P}i\hat{\mathcal{L}}\int_{t_0}^{t} d\tau e^{(t-\tau)\hat{Q}i\hat{\mathcal{L}}\hat{Q}}i\hat{\mathcal{L}}_1\hat{P}\hat{\rho}(\tau)$$
$$= \hat{P}i\hat{\mathcal{L}}_1\int_{t_0}^{t} d\tau e^{(t-\tau)\hat{Q}i\hat{\mathcal{L}}\hat{Q}}i\hat{\mathcal{L}}_1\hat{P}\hat{\rho}(\tau). \qquad (4.55)$$

Here, we have used the following relations to obtain Eqs. (4.54) and (4.55),

$$i\hat{\mathcal{L}}_{B(C)}\hat{\rho}_{B(C)} = 0, \qquad (4.56)$$

$$\mathrm{Tr}_{B(C)}[i\hat{\mathcal{L}}_1\hat{\rho}_{B(C)}] = 0, \qquad (4.57)$$

$$i\hat{\mathcal{L}}_B\hat{P}\bullet = 0, \qquad (4.58)$$

$$\hat{P}i\hat{\mathcal{L}}_B\hat{P}\bullet = 0, \qquad (4.59)$$

$$\hat{P}i\hat{\mathcal{L}}\hat{Q}\bullet = \hat{P}i\hat{\mathcal{L}}_1\bullet. \qquad (4.60)$$

As a result, we obtain the exact form of the equation of motion for the density matrix of nanostructure in the joint system,

$$\frac{\partial \hat{\sigma}(t)}{\partial t} = i\hat{\mathcal{L}}_A \hat{\sigma}(t) + \mathrm{Tr}_B \mathrm{Tr}_C i\hat{\mathcal{L}}_1 \int_{t_0}^t d\tau e^{(t-\tau)\hat{Q}i\hat{\mathcal{L}}\hat{Q}} i\hat{\mathcal{L}}_1 \hat{\rho}_B \hat{\rho}_C \hat{\sigma}(\tau). \tag{4.61}$$

It is very difficult to exactly solve the equation. Therefore, we treat the effect of connection between a nanostructure and an electrode as a perturbation. When the $\hat{\mathcal{L}}$ in the exponential part in Eq. (4.61) is replaced by $\hat{\mathcal{L}}_0$, the part is rewrittn as

$$\exp\left((t-\tau)\hat{Q}i\hat{\mathcal{L}}\hat{Q}\right) \rightarrow \exp\left((t-\tau)\hat{Q}i\hat{\mathcal{L}}_0\hat{Q}\right) \tag{4.62}$$
$$= \exp\left((t-\tau)(1-\hat{P})i\hat{\mathcal{L}}_0(1-\hat{P})\right)$$
$$= \exp\left((t-\tau)i\hat{\mathcal{L}}_0\right). \tag{4.63}$$

Here, $\hat{Q}i\hat{\mathcal{L}}_0\hat{P} \bullet = 0$ and $\hat{P}i\hat{\mathcal{L}}_0 \bullet = 0$ have been used. Thus, we obtain the equation of motion for the second-order of $\hat{\mathcal{H}}_1$,

$$\frac{\partial \hat{\sigma}(t)}{\partial t} = i\hat{\mathcal{L}}_A \hat{\sigma}(t) + \mathrm{Tr}_B \mathrm{Tr}_C i\hat{\mathcal{L}}_1 \int_{t_0}^t d\tau e^{(t-\tau)i\hat{\mathcal{L}}_0} i\hat{\mathcal{L}}_1 \hat{\rho}_B \hat{\rho}_C \hat{\sigma}(\tau) \tag{4.64}$$

For later discussions, we consider the equation of motion for the density matrix in the interaction picture. Using Eq. (3.48), the projected density matrix $\hat{\sigma}(t)$ in the interaction picture is defined as

$$\hat{\sigma}_I(t) = e^{i\frac{\hat{\mathcal{H}}_0}{\hbar}(t-t_0)} \hat{\sigma}(t) e^{-i\frac{\hat{\mathcal{H}}_0}{\hbar}(t-t_0)}$$
$$= e^{i\frac{\hat{\mathcal{H}}_A}{\hbar}(t-t_0)} \hat{\sigma}(t) e^{-i\frac{\hat{\mathcal{H}}_A}{\hbar}(t-t_0)}$$
$$= e^{i\hat{\mathcal{L}}_A(t-t_0)} \hat{\sigma}(t). \tag{4.65}$$

We have the following equation of motion for the density matrix in the interaction picture,

$$\frac{\partial \hat{\sigma}_I(t)}{\partial t} = \frac{\partial}{\partial t}\left(e^{-i\hat{\mathcal{L}}_A(t-t_0)} \hat{\sigma}(t)\right)$$
$$= -i\hat{\mathcal{L}}_A e^{-i\mathcal{L}_A(t-t_0)} \hat{\sigma}(t) + e^{-i\hat{\mathcal{L}}_A(t-t_0)} \frac{\partial \hat{\sigma}(t)}{\partial t}. \tag{4.66}$$

In this work, we investigate the transient electronic current flowing through the nanostructure using Eqs. (4.64) and (4.66).
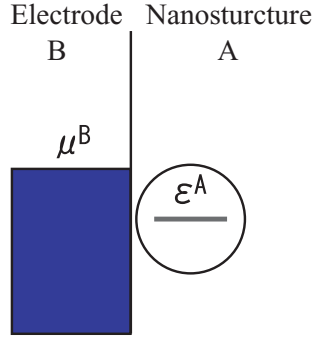
Figure 4.6: Schematic picture of the joint system consisting of an electrode (B) and a nanostructure (A).

4.4   Results and Discussion

4.4.1   The joint system of a nanostructure and an electrode

We consider the joint system of a nanostructure (A) and one electrode (B). For simplicity, the nanostructure is assumed to have only one discrete energy level. Inserting Eq. (4.64) to Eq. (4.66) and developing the commutation relations $\hat{\mathcal{L}}_A$ and $\hat{\mathcal{L}}_1$, we obtain

$$
\begin{aligned}
\frac{\partial \hat{\sigma}_I(t)}{\partial t} = \left(\frac{t^{AB}}{\hbar}\right)^2 \int_{t_0}^t d\tau \sum_k \sum_{k'} \{ & - \hat{a}_I(t)\hat{a}_I^\dagger(\tau)\hat{\sigma}_I(\tau)\mathrm{Tr}_B[\hat{\rho}_B \hat{b}_{Ik}^\dagger \hat{b}_{Ik'}(\tau - t)] \\
& - \hat{a}_I^\dagger(t)\hat{a}_I(\tau)\hat{\sigma}_I(\tau)\mathrm{Tr}_B[\hat{\rho}_B \hat{b}_{Ik}\hat{b}_{Ik'}^\dagger(\tau - t)] \\
& + \hat{a}_I(t)\hat{\sigma}_I(\tau)\hat{a}_I^\dagger(\tau)\mathrm{Tr}_B[\hat{\rho}_B \hat{b}_{Ik'}(\tau - t)\hat{b}_{Ik}^\dagger] \\
& + \hat{a}_I^\dagger(t)\hat{\sigma}_I(\tau)\hat{a}_I(\tau)\mathrm{Tr}_B[\hat{\rho}_B \hat{b}_{Ik'}^\dagger(\tau - t)\hat{b}_{Ik}] \\
& + \hat{a}_I(\tau)\hat{\sigma}_I(\tau)\hat{a}_I^\dagger(t)\mathrm{Tr}_B[\hat{\rho}_B \hat{b}_{Ik'}\hat{b}_{Ik}^\dagger(\tau - t)] \\
& + \hat{a}_I^\dagger(\tau)\hat{\sigma}_I(\tau)\hat{a}_I(t)\mathrm{Tr}_B[\hat{\rho}_B \hat{b}_{Ik'}^\dagger \hat{b}_{Ik}(\tau - t)] \\
& - \hat{\sigma}_I(\tau)\hat{a}_I(\tau)\hat{a}_I^\dagger(t)\mathrm{Tr}_B[\hat{\rho}_B \hat{b}_{Ik}^\dagger(\tau - t)\hat{b}_{Ik'}] \\
& - \hat{\sigma}_I(\tau)\hat{a}_I^\dagger(\tau)\hat{a}_I(t)\mathrm{Tr}_B[\hat{\rho}_B \hat{b}_{Ik}(\tau - t)\hat{b}_{Ik'}^\dagger]\}.
\end{aligned}
$$
(4.67)

To obtain the above equation, we neglect terms which don't satisfy the particle-number-conservation law, such as terms including $\hat{a}_I(t)\hat{a}_I(\tau)$ and $\hat{b}_{Ik}^\dagger \hat{b}_{Ik'}^\dagger(\tau - t)$. The trace over the eigenstates of electrode (B) can be realized by using the Fermi distribution function, $f_k^{\mu_B}$, such as

$$
\mathrm{Tr}_B[\hat{\rho}_B \hat{b}_{Ik}^\dagger \hat{b}_{Ik'}(\tau - t)] = e^{-i\varepsilon_k^B(\tau - t)/\hbar} f_k^{\mu_B} \delta_{kk'}, \tag{4.68}
$$

where $f_k^{\mu_B} \equiv 1/(e^{\beta(\varepsilon_k^B - \mu_B)} + 1)$.

Then we consider the diagonal component of the density matrix $\hat{\sigma}(t)$. We represent the eigenstates of the isolated nanostructure as $|0\rangle$ and $|1\rangle$. $|0\rangle$ is the vacuum

state, and $|1\rangle$ is the state occupying the nanostructure with a single electron. Thus, $|1\rangle$ is related to $|0\rangle$ as,

$$|1\rangle = \hat{a}^\dagger |0\rangle. \tag{4.69}$$

Using Eqs. (4.67)-(4.69), the time dependence of the probability that an electron is located in the nanostructure is obtained as follows,

$$\frac{\partial \langle 1|\hat{\sigma}(t)|1\rangle}{\partial t} = \left(\frac{t^{AB}}{\hbar}\right)^2 \int_{t_0}^{t} d\tau \sum_k 2\cos((\varepsilon^A - \varepsilon_k^B)(\tau - t)/\hbar)$$
$$\{f_k^{\mu_B}\langle 0|\hat{\sigma}(\tau)|0\rangle - (1 - f_k^{\mu_B})\langle 1|\hat{\sigma}(\tau)|1\rangle\}. \tag{4.70}$$

The first term represents the electronic flow from the occupied states of electrode to the unoccupied states of nanostructure, and the second term represents the flow from the occupied states of nanostructure to the unoccupied states of electrode. These flows vibrate at frequency of $(\varepsilon^A - \varepsilon_k^B)/\hbar$. The diagonal components of the density matrix satisfies the relation, $\langle 0|\hat{\sigma}(t)|0\rangle + \langle 1|\hat{\sigma}(t)|1\rangle = 1$, because the density matrix is normalized. Thus, from Eq. (4.70), we have

$$\frac{\partial \langle 1|\hat{\sigma}(t)|1\rangle}{\partial t} = \left(\frac{t^{AB}}{\hbar}\right)^2 \int_{t_0}^{t} d\tau \sum_k 2\cos((\varepsilon^A - \varepsilon_k^B)(\tau - t)/\hbar)(-\langle 1|\hat{\sigma}(\tau)|1\rangle + f_k^{\mu_B}). \tag{4.71}$$

Equation (4.71) is divided into the first term which does not depends on the Fermi energy of the electrode and the second term which depend on it.

Then, we convert the summation over the wavevectors, k, to the integral on the energy. To simplify, we assume that the density of states in the electrodes is uniform from the bottom of the energy band to the top of the energy band as

$$\sum_k \cdots = D \int_{-\varepsilon_{\text{edge}}}^{+\varepsilon_{\text{edge}}} d\varepsilon \cdots . \tag{4.72}$$

Here, the magnitude of the density of states is assumed to be constant, D, between the band bottom, $-\varepsilon_{\text{edge}}$, to the band top, $\varepsilon_{\text{edge}}$. When the $\varepsilon_{\text{edge}} \gg \varepsilon^A$ is satisfied, the first term of Eq. (4.71) can be rewritten as

$$\sum_k \cos((\varepsilon_k^B - \varepsilon^A)(t - \tau)/\hbar) = D \int_{-\varepsilon_{\text{edge}}}^{+\varepsilon_{\text{edge}}} d\varepsilon \cos((\varepsilon - \varepsilon^A)(t - \tau)/\hbar) \tag{4.73}$$

$$\simeq 2\pi\hbar D \frac{\sin(\varepsilon_{\text{edge}}(t - \tau)/\hbar)}{\pi(t - \tau)}. \tag{4.74}$$

Furthermore, when the band width is enough large, the following equation is obtained approximatively from Eq. (4.74),

$$2\pi\hbar D \frac{\sin(\varepsilon_{\text{edge}}(t - \tau)/\hbar)}{\pi(t - \tau)} \rightarrow 2\pi\hbar D\delta(t - \tau). \tag{4.75}$$
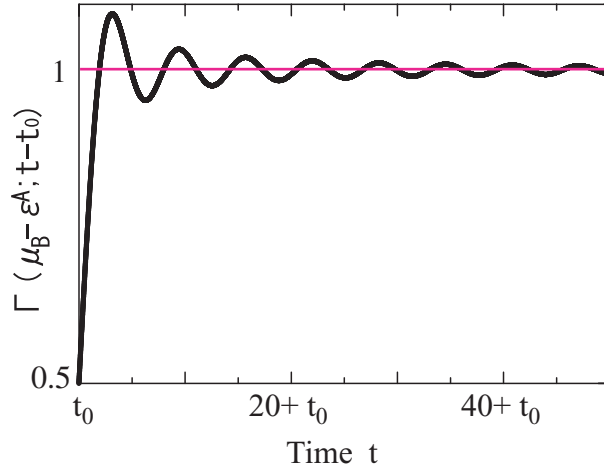
Figure 4.7: Calculated function, $\Gamma(\mu_B - \varepsilon^A; t - t_0)$. Here, $\varepsilon^A = -1$, $\mu_B = 0$ and $\hbar = 1$ have been employed. The function, Γ, converges to 1 in case of $\mu_B > \varepsilon^A$, while it converges to 0 in case of $\mu_B < \varepsilon^A$.

When the temperature is zero, the second term of Eq. (4.71) is rewritten as follows,

$$\sum_k \cos((\varepsilon_k^B - \varepsilon^A)(t - \tau)/\hbar) f_k^{\mu_B} = D \int_{-\varepsilon_{\text{edge}}}^{\mu_B} d\varepsilon \cos((\varepsilon - \varepsilon^A)(t - \tau)/\hbar) \quad (4.76)$$

$$\to \pi\hbar D \delta(t - \tau) + \pi\hbar D \frac{\sin((\mu_B - \varepsilon^A)(t - \tau)/\hbar)}{\pi(t - \tau)}. \quad (4.77)$$

Using Eqs. (4.75) and (4.77), Eq. (4.71) is rewritten as

$$\frac{\partial \langle 1|\hat{\sigma}(t)|1\rangle}{\partial t} = \left(\frac{t^{AB}}{\hbar}\right)^2 2\hbar D \left\{ -\pi \langle 1|\hat{\sigma}(t)|1\rangle + \frac{\pi}{2} + \int_0^{t-t_0} ds \frac{\sin((\mu_B - \varepsilon^A)s/\hbar)}{s} \right\} \quad (4.78)$$

$$= \left(\frac{t^{AB}}{\hbar}\right)^2 2\pi\hbar D \left\{ -\langle 1|\hat{\sigma}(t)|1\rangle + \Gamma(\mu_B - \varepsilon^A; t - t_0) \right\}, \quad (4.79)$$

where

$$\Gamma(\mu_B - \varepsilon^A; t - t_0) \equiv +\frac{1}{2} + \int_0^{t-t_0} ds \frac{\sin((\mu_B - \varepsilon^A)s/\hbar)}{\pi s}. \quad (4.80)$$

The first term of Eq. (4.79) leads the joint system to a steady state. The second term contains the Fermi energy of electrode and decides the probability that electron is located in the nanostructure under the steady state of the system.

The first term of Eq. (4.79) is derived from the first term of Eq. (4.71). When the band width becomes very wide, an electron having wavevector, k, shuttles between a nanostructure and an electrode with a frequency, $(\varepsilon_k^B - \varepsilon^A)/\hbar$. The probabilistic motion of electron is expressed by the superposition of these various

frequencies, because the energy ε_k^B can take values from $-\varepsilon_{\text{edge}}$ to $\varepsilon_{\text{edge}}$. As the result, the delta function appears as shown in Eqs. (4.73)-(4.75) and the first term of Eq. (4.79) is produced. It shows that the existence of a lot of states in the electrode is essential to lead the joint system to a steady state. If the band width of the electrode is very narrow ($\varepsilon_k^B \sim \varepsilon^B$), electrons simply shuttle between an electrode and a nanostructure at a single frequency about $(\varepsilon^B - \varepsilon^A)/\hbar$, instead of reaching to the steady states. In this case, there is an analogy between this system and the two-room system discussed in Sec. 4.2.

On the other hand, the function, Γ, is derived from the second term of Eq. (4.71). The function, Γ, depends on the Fermi energy of the electrode. It reflects two different electron motions. One is the shuttle motion between the occupied states of electrode and the unoccupied state of nanostructure. Another one is that between the unoccupied states of electrode and the occupied state of nanostructure. Therefore, the frequency of the function, Γ, is decided by the superposition of frequencies from $(-\varepsilon_{\text{edge}} - \varepsilon^A)/\hbar$ to $(\mu_B - \varepsilon^A)/\hbar$ and from $(\mu_B - \varepsilon^A)/\hbar$ to $(+\varepsilon_{\text{edge}} - \varepsilon^A)/\hbar$. As the result, the superposition gives the function, Γ, the frequency $(\mu_B - \varepsilon^A)/\hbar$ as shown in Eq. (4.77). In other words, the vibration of the electronic current originates from the quantum interference between the current from the nanostructure to the electrode and the current in the contrary direction. As an example, the calculated function, Γ, is shown in Fig. 4.7, where $\varepsilon^A = -1$, $\mu_B = 0$ and $\hbar = 1$ are employed. The function converges to 1 in case of $\mu_B > \varepsilon^A$. However, it converges to 0 in case of $\mu_B < \varepsilon^A$.

The time derivative of the density matrix, $\langle 1|\hat{\sigma}(t)|1\rangle$, corresponds to the electronic current between an electrode and a nanostructure, $\langle I(t)\rangle$. The electronic current is defined using Eq. (4.79) as follows,

$$\langle I(t)\rangle \equiv e\frac{\partial\langle 1|\hat{\sigma}(t)|1\rangle}{\partial t} \tag{4.81}$$

$$= e\left(\frac{t^{AB}}{\hbar}\right)^2 2\pi\hbar D\left\{ -\langle 1|\hat{\sigma}(t)|1\rangle + \Gamma(\mu_B - \varepsilon^A; t - t_0)\right\}. \tag{4.82}$$

In order to compute the electronic current, we use a small but finite time slice Δt for Eq. (4.79),

$$\frac{\langle 1|\hat{\sigma}(t + \Delta t)|1\rangle - \langle 1|\hat{\sigma}(t)|1\rangle}{\Delta t} = \left(\frac{t^{AB}}{\hbar}\right)^2 2\pi\hbar D\left\{ -\langle 1|\hat{\sigma}(t)|1\rangle + \Gamma(\mu_B - \varepsilon^A; t - t_0)\right\}, \tag{4.83}$$

$$\frac{\langle 1|\hat{\sigma}(t)|1\rangle - \langle 1|\hat{\sigma}(t - \Delta t)|1\rangle}{\Delta t} = \left(\frac{t^{AB}}{\hbar}\right)^2 2\pi\hbar D\left\{ -\langle 1|\hat{\sigma}(t)|1\rangle + \Gamma(\mu_B - \varepsilon^A; t - t_0)\right\}. \tag{4.84}$$

Combining the above two equations, we have the following recurrence formula,

$$\langle 1|\hat{\sigma}(t + 2\Delta t)|1\rangle$$

$$= \langle 1|\hat{\sigma}(t)|1\rangle + 2\Delta t\left(\frac{t^{AB}}{\hbar}\right)^2 2\pi\hbar D\left\{ -\langle 1|\hat{\sigma}(t + \Delta t)|1\rangle + \Gamma(\mu_B - \varepsilon^A; t + \Delta t - t_0)\right\}. \tag{4.85}$$

Using this formula, we obtain $\langle 1|\hat{\sigma}(t)|1\rangle$ from the initial state $\langle 1|\hat{\sigma}(t_0)|1\rangle$. Furthermore, we obtain electronic current by inserting this $\langle 1|\hat{\sigma}(t)|1\rangle$ to Eq. (4.82).

Next, we apply the formula to the simple systems and confirm whether the formula gives valid results.

- Case of $\mu_B > \varepsilon^A$

  First, we investigate the time development of the electronic state when the Fermi energy of the electrode is higher than the energy level of nanostructure. It is assumed that nanostructure is not filled with electrons at initial time. In this case, the time development of electron number in the nanostructure and transient electronic current are shown by the red line and the blue line, respectively, in Fig. 4.8(a). Here, $t^{AB} = 0.2$, $\mu_B = 0$, $\varepsilon^A = -1$, $D = 1$, $\hbar = 1$ and $t_0 = 0$ have been employed. The electrons flow to the nanostructure from the electrode, and, after that, the joint system reaches to the steady state that the nanostructure is filled with one electron. To estimate the relaxation time, it is assumed that there is not time dependence of the memory function, and we obtain the following equation from Eq. (4.79),

  $$\langle 1|\hat{\sigma}(t)|1\rangle \propto \left(-e^{-\left(\frac{t^{AB}}{\hbar}\right)^2 2\pi\hbar Dt} + 1\right). \tag{4.86}$$

  Thus, the relaxation time is decided by the square of coupling magnitude t^{AB}. The small vibration of electronic current in approaching to the steady state comes from the interference between the current from the electrode to the nanostructure and the inverse current. The frequency of this vibration is $(\mu_B - \varepsilon^A)/\hbar$.

  Then, we investigate the time development of the joint system in case that the nanostructure has already been filled with an electron. The calculation result is shown in Fig. 4.8(b). A few electrons are released from the nanostructure just after the connection. The reason is that some electrons in the nanostructure can transfer to the unoccupied states of the electrode. Actually, such current doesn't appear in case that the energy difference between the energy level of the nanostructure and the Fermi energy of the electrode is much larger than the coupling magnitude t^{AB}, because the electrons in the nanostructure cannot flow to the unoccupied states of the electrode.

  We can easily obtain the steady state without numerical calculations. As shown in Fig. 4.7, the function Γ converges to 1. Thus, the density matrix satisfies the following equation in the steady state,

  $$\lim_{t \to +\infty} \frac{\partial \langle 1|\hat{\sigma}(t)|1\rangle}{\partial t} = \left(\frac{t^{AB}}{\hbar}\right)^2 2\pi\hbar D\{-\langle 1|\hat{\sigma}(\infty)|1\rangle + 1\}. \tag{4.87}$$

  When time passed longer than the relaxation time, the time derivative of density matrix must converge to zero. Thus we obtain

  $$\{-\langle 1|\hat{\sigma}(\infty)|1\rangle + 1\} = 0. \tag{4.88}$$

  It shows that a state filled with an electron becomes a steady state independent of initial states.
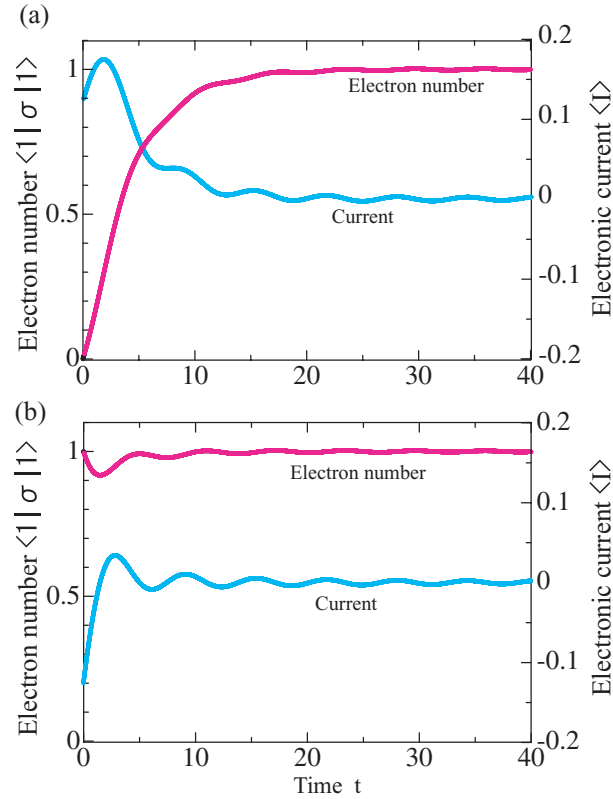
Figure 4.8: Calculated electron number in the nanostructure and electronic current as a function of time, in case (a) that the there was not electron in the nanostructure at initial time and in case (b) that the nanostructure was filled with an electron at initial time. The energy level of the nanostructure is lower than the Fermi energy of the electrode. $t^{AB} = 0.2$, $\mu_B = 0$, $\varepsilon^A = -1$, $D = 1$, $\hbar = 1$ and $t_0 = 0$ have been used.
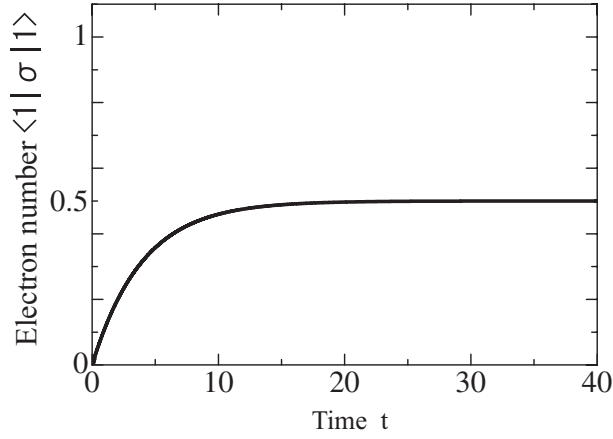
Figure 4.9: Calculated electron number in the nanostructure as a function of time, in case that there was no electrons in the nanostructure at initial time. The energy level of the nanostructure is equal to the Fermi energy of the electrode. $t^{AB} = 0.2$, $\mu_B = 0$, $\varepsilon^A = 0$, $D = 1$, $\hbar = 1$ and $t_0 = 0$ have been used.

- Case of $\mu_B = \varepsilon^A$

  Then we consider the time development in case that the Fermi energy is equal to the energy level of the nanostructure. In this case, the function, Γ, has a constant value 0.5. Therefore, the number of electron in nanostructure converges to 0.5 without vibrating after the connection. Figure 4.9 is the calculated result when $\mu_B = \varepsilon^A = 0$. It is assumed that there was no electrons in the nanostructure at initial time. The other parameters are same to ones used in Fig. 4.8(a). The reason of no vibration is that the vibration of current from the electrode to the nanostructure and the vibration of current from the nanostructure to the electrode are canceled out each other.

- Case of $\mu_B \gg \varepsilon^A$

  In case that the energy difference between Fermi energy of the electrode and the energy level of the nanostructure is much larger than the coupling magnitude t^{AB}, the vibration doesn't appear in the variation of electron number in the nanostructure, because the frequency of Γ is too high and the vibration is canceled out each other. In other words, it is easy for current to flow from the electrode to the nanostructure, but it is difficult to come back from the nanostructure to the electrode. Thus, the vibration induced by the interference between these currents doesn't appear. Figure 4.10(a) is the calculated result when $\mu_B = 0$ and $\varepsilon^A = -10$. The other parameters are same to ones used in Fig. 4.8(a). We show the memory function in this case in Fig. 4.10(b). The frequency is higher than that shown in Fig. 4.7.

Using the formula developed in this work, we investigated the joint systems which consist of an electrode and a nanostructure, and confirmed that the formula gave the valid results for the transient phenomena.
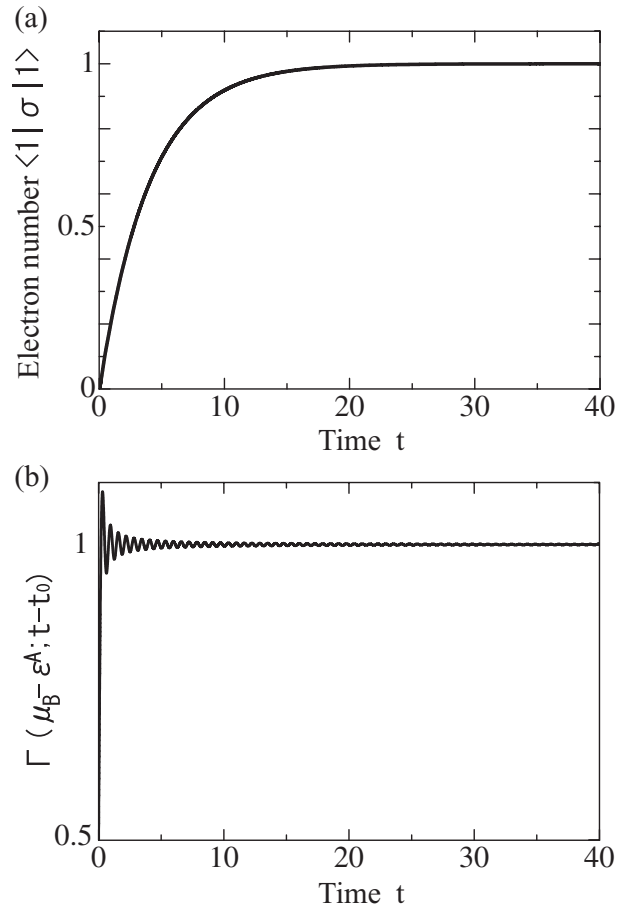
Figure 4.10: (a) Calculated electron number of the nanostructure as a function of time, in case that the there was no electrons in the nanostructure at initial time. (b) Calculated function, Γ. These figures correspond to the case where the energy level of the nanostructure is lower than the Fermi energy of the electrode, and the energy difference is much larger than the coupling magnitude. $t^{AB} = 0.2$, $\mu_B = 0$, $\varepsilon^A = -10$, $D = 1$, $\hbar = 1$ and $t_0 = 0$ have been used.
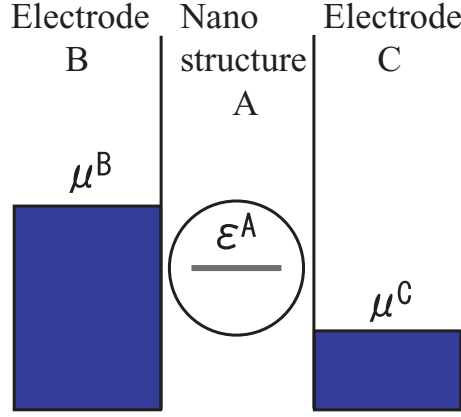
Figure 4.11: Schematic energy diagram of the joint system consisting of two electrodes (B and C) and a nanostructure (A).

4.4.2 The joint system of a nanostructure and two electrodes

Then, we consider the joint system which consists of two electrodes (B and C) and a nanostructure (A). It is reasonably assumed that the Fermi energy of the left electrode μ_B is larger than that of the right electrode μ_C. Figure 4.11 shows the schematic energy diagram of the joint system. From the same calculations that we used to obtain Eq. (4.79), we have the equation of time derivative of density matrix for the joint system as follows,

$$\frac{\partial \langle 1|\hat{\sigma}(t)|1\rangle}{\partial t} = \left(\frac{t^{AB}}{\hbar}\right)^2 2\pi \hbar D\Big\{ -\langle 1|\hat{\sigma}(t)|1\rangle + \Gamma(\mu_B - \varepsilon^A; t - t_0)\Big\}$$
$$+ \left(\frac{t^{AC}}{\hbar}\right)^2 2\pi \hbar D\Big\{ -\langle 1|\hat{\sigma}(t)|1\rangle + \Gamma(\mu_C - \varepsilon^A; t - t_0)\Big\}, \quad (4.89)$$

where we assume that the densities of states of two electrodes are same. The electronic current at left contact is given by the following equation,

$$\langle I_L(t)\rangle = e\left(\frac{t^{AB}}{\hbar}\right)^2 2\pi \hbar D\Big\{ -\langle 1|\hat{\sigma}(t)|1\rangle + \Gamma(\mu_B - \varepsilon^A; t - t_0)\Big\}. \quad (4.90)$$

Similarly, the electronic current at right contact is written by

$$\langle I_R(t)\rangle = -e\left(\frac{t^{AC}}{\hbar}\right)^2 2\pi \hbar D\Big\{ -\langle 1|\hat{\sigma}(t)|1\rangle + \Gamma(\mu_C - \varepsilon^A; t - t_0)\Big\}. \quad (4.91)$$

Using above equations, we investigate the two situations. One is a case that the energy level of nanostructure is located just exactly at the middle position of Fermi energies of two electrodes. Another one is a case that the energy level of nanostructure is located near a Fermi energy of an electrode. We assume that there is no electrons in the nanostructure at initial time, t_0.

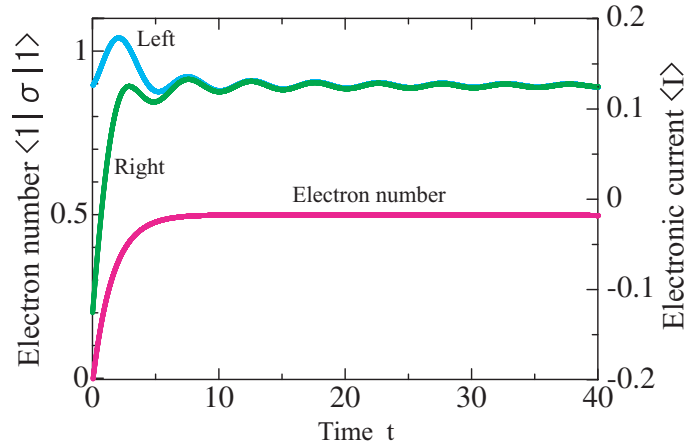- Case of $(\mu_B - \varepsilon^A) = (\varepsilon^A - \mu_C)$

Figure 4.12: Calculated electron number of the nanostructure and electronic currents as a function of time, in case that the there was no electrons in the nanostructure at initial time. The electron number is shown by a red line. The electronic currents at left and right contacts are shown by blue and green lines, respectively. These currents have the same frequency in this case. $t^{AB} = t^{AC} = 0.2$, $\mu_B = 1$, $\mu_C = -1$, $\varepsilon^A = 0$, $D = 1$, $\hbar = 1$ and $t_0 = 0$ have been used.

First, we consider the situation that the energy level of nanostructure is located at the middle position of Fermi energies of two electrodes. The parameters adopted in this calculation are $t^{AB} = t^{AC} = 0.2$, $\mu_B = 1$, $\mu_C = -1$, $\varepsilon^A = 0$, $D = 1$, $\hbar = 1$ and $t_0 = 0$. The calculated number of electron in the nanostructure and electronic currents are shown in Fig. 4.12. The electron number is shown by a redline. The currents at the left and the right conntacts are shown by blue and green lines, respectively. Under the steady state, electrons come into the nanostructure from the left electrode and then the electrons flow out to the right electrode. Since these current have same magnitude, the nanostructure is half filled with electrons. The current at left contact vibrates with a frequency, $|\mu_B - \varepsilon^A|/\hbar$. The frequency of the current at right contact is equal to that of the current at left contact. Thus, vibration doesn't appear in the change of the electron number. Furthermore, Fig. 4.12 shows that, just after the connection, electrons flow into the nanostructure from not only the left electrode but also the right electrode.

• Case of $(\mu_B - \varepsilon^A) \neq (\varepsilon^A - \mu_C)$

Finally, we consider a case that the energy level of nanostructure is located near the Fermi energy of left electrode. The parameters adopted in this calculation are $t^{AB} = t^{AC} = 0.2$, $\mu_B = 1$, $\mu_C = -1$, $\varepsilon^A = 0.8$, $D = 1$, $\hbar = 1$ and $t_0 = 0$. The calculated number of electron in the nanostructure and electronic currents are shown in Fig. 4.13. The electron number and the currents are shown using the same colored curves used in Fig. 4.12. In this case, the current at left contact vibrates with a frequency, $|\mu_B - \varepsilon^A|/\hbar$. On the other hand, the current at right contact vibrates with a different fre-
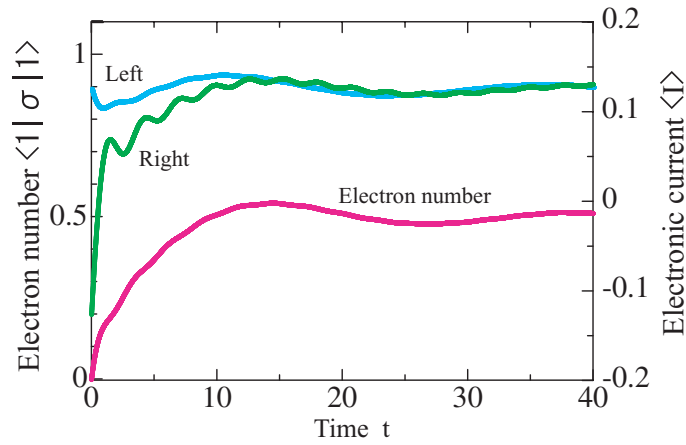
Figure 4.13: Calculated electron number of the nanostructure and electronic currents as a function of time, in case that the there was no electrons in the nanostructure at initial time. The electron number is shown by a red line. The electronic current between the left (right) electrode and the nanostructure is shown by a blue (green) line. These currents have different frequencies in this case. $t^{AB} = t^{AC} = 0.2$, $\mu_B = 1$, $\mu_C = -1$, $\varepsilon^A = 0.8$, $D = 1$, $\hbar = 1$ and $t_0 = 0$ have been used.
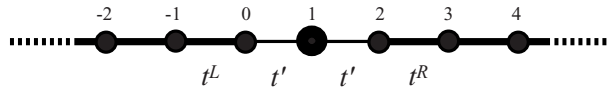

Figure 4.14: Schematic picture of the joint system. The sites labeled with the number of less than zero are included in the left electrode, while the sites labeled with the number of more than two are included in the right electrode. The nanostructure, which has a single orbital, corresponds to the 1-st site.

quency, $|\mu_C - \varepsilon^A|/\hbar$. As a result, the change of the number of electron in the nanostructure shows the vibration. Therefore, the system takes more time to reach the steady state than the previous case. These phenomena are the results of the quantum interference which can not be obtained by electronic-current calculation methods under the steady state.

4.4.3 Comparison between the nonequilibrium Green function method and the projected density matrix method

In order to confirm the validity of the projected density matrix method developed in this work, we compare the steady current obtained by the nonequilibrium-Green-function method with the steady current obtained by the projected density-matrix method. We consider the joint system as shown in Fig. 4.14. Each lattice point has a single orbital. The left electrode is numbered as less than zero, and the right electrode is numbered as more than two. The 1-st site represents the

nanostructure. The energy level of the nanostructure is written by ε^A. The transfer energies in the left and right electrodes are defined as t^L and t^R, respectively. The magnitude of contact between the nanostructure and the electrode is set as t'. Then, using the nonequilibrium Green function method, the steady current is obtained as follows,

$$\langle I \rangle = 4\frac{e}{h}t'^4 \int_{-\infty}^{+\infty} dE(f^L(E) - f^R(E)){\rm Im}[g_{00}^a(E)]G_{11}^r(E)G_{11}^a(E){\rm Im}[g_{22}^a(E)].$$
(4.92)

When we employ the wide-band approximation for the electrodes, the Green function of the joint system is rewritten as follows,

$$G_{11}^a = \frac{g_{11}^a}{1 - t'^2(g_{11}^a g_{22}^a + g_{11}^a g_{00}^a)}$$
(4.93)

$$\simeq \frac{\frac{1}{E - \varepsilon^A + i\delta}}{1 - t'^2\left(\frac{1}{E - \varepsilon^A + i\delta}\frac{-i}{t^R} + \frac{1}{E - \varepsilon^A + i\delta}\frac{-i}{t^L}\right)}$$
(4.94)

$$= \frac{1}{E - \varepsilon^A + i\left(\delta + t'^2\left(\frac{1}{t^R} + \frac{1}{t^L}\right)\right)}.$$
(4.95)

In case that the energy level of the nanostructure is located between Fermi energies of two electrodes, we have the following steady current formula,

$$\langle I \rangle = 4\frac{e}{h}t'^4\frac{1}{t^L}\frac{1}{t^R}\pi\frac{1}{t'^2\left(\frac{1}{t^R} + \frac{1}{t^L}\right)}$$
$$= \frac{e}{h}\frac{2\pi t'^2}{t^L},$$
(4.96)

where we assume $t^L = t^R$. The density of states of the left electrode is defined as,

$$D = \frac{1}{\pi}{\rm Im}[g_{00}^a] = \frac{1}{\pi t^L}.$$
(4.97)

Thus, the steady current is rewritten as

$$\langle I \rangle = \frac{e}{h}2\pi^2 t'^2 D.$$
(4.98)

On the other hand, the current between the left electrode and the nanostructure is written as

$$\langle I_L(t) \rangle = e\left(\frac{t'}{\hbar}\right)^2 2\pi\hbar D\left\{-\langle 1|\hat{\sigma}(t)|1\rangle + \Gamma(\mu_L - \epsilon^A; t - t_0)\right\}.$$
(4.99)

After reaching the steady state, the current at left contact is equal to the current at right contact. Under the steady state, the memory function converges to 1, thus we have

$$\langle I(+\infty) \rangle = e\left(\frac{t'}{\hbar}\right)^2 2\pi\hbar D\left\{-\langle 1|\hat{\sigma}(+\infty)|1\rangle + 1\right\}.$$
(4.100)

From Fig. 4.12, $\langle 1|\hat{\sigma}(+\infty)|1\rangle$ has 0.5 under the steady state. Therefore we obtain the steady current from the density matrix method as follows,

$$
\begin{aligned}
\langle I(+\infty)\rangle &= e\left(\frac{t'}{\hbar}\right)^2 \pi\hbar D \\
&= \frac{e}{h}2\pi^2 t'^2 D.
\end{aligned}
\tag{4.101}
$$

We can confirm that the nonequilibrium-Green-function method and the projected density-matrix method give the same steady current in the model discussed in this work.

4.5 Conclusions

We developed the calculation method for the time-dependent electronic current, using the density matrix method and the projection operator method under the simple tight-binding approximation. Then we applied the formula to the simple joint systems which consist of two-bulk electrodes and a nanostructure. It was confirmed that the expected steady state is realized in the joint system. Furthermore, we found that when the Fermi energy of electrode is located near the discrete energy level of the nanostructure, the transient current shows vibration. It is clarified that such oscillation originates from the quantum interference between the current from the electrode to the nanostructure and the inverse current. Finally, we confirmed that the nonequilibrium-Green-function method and the projected density-matrix method give the same steady electronic current in our model discussed in this work.

Chapter 5

Summary

The advance of nanotechnology, which aims for the micro-fabrication and the integration of electronic devices, has made it possible to fabricate various nanometer-scale structures. For example, the remarkable progress is seen in the semiconductor electronics or molecular science fields. It is known that the quantum effects, such as the interference, clearly appear in the physical characteristics of the nanometer-scale systems. In chapters 2 and 3, we studied the optical and electron transport properties of nanostructure network systems, which have the multiple degenerate electronic states originating from the quantum interference induced by the particular spatial symmetry of the system [36, 40, 52–56]. On the other hand, recently, the energy dissipative process and the dynamics of the transport properties of nanostructure systems also attract much attention. When the practical applications of the nanostructures are considered, we cannot ignore these. However, the calculation method of time-dependent current has not been established yet. Thus, in chapter 4, we proposed the calculation method of time-dependent current, in which the density matrix method and the projection operator method are used. The main conclusions obtained in this thesis are as follows.

- Chapter 2

    We studied the optical properties of the InAs Kagomé quantum-wire system employing a tight-binding model. The Kagomé lattice have the flat bands at the conduction-band bottom and the valence-band top. We assumed that an electron and a hole exist in the conduction band and the valence band in this system, respectively. We investigated the binding energy and the radius of flat-band exciton, which is the bound state of the electron and the hole. For the comparison, excitons in the square, triangular, Tasaki and one-dimensional lattices are investigated. Tasaki lattice also has flat bands.

    It was found that the binding energies of excitons in the Kagomé and Tasaki lattices are much larger than those in other two-dimensional lattices and even larger than that in the one-dimensional lattice, although the radii of excitons in the Kagomé and Tasaki lattice are almost same as that in the triangular lattice. Furthermore, the binding energy of exciton in the Tasaki lattice is larger than on-site Coulomb attractive energy. These results

111

indicate that the localization nature of exciton is not the unique origin of larger exciton binding energy. By the perturbation analysis, it was shown that both the localization nature and the macroscopic degree of degeneracy of the flat-band eigenstates of electron and hole are the origins of large exciton binding energy. It was also found that when a magnetic field is applied, the binding energy of a flat-band exciton shows a large variation, because the flat bands become dispersive by applying the magnetic field.

• Chapter 3

We investigated electron transport properties of the finite-size Kagomé-lattice-chain systems, using the simple tight-binding model and nonequilibrium Green function method. To simplify, we assumed that the Coulomb interaction doesn't work between electrons.

We found that the current through the flat-band channel is sensitive to the direction of the applied electric field; a large current is observed to flow along the chain when the electric field is applied perpendicular to the chain, while no current is observed to flow along the chain when the electric field is applied along the chain. By analyzing how the flat-band degeneracy is broken, we clarified that this strange anisotropy originates from the unique feature of the flat-band states. Flat-band state has simultaneously both itinerant and localized characteristics. However, the electric field along the chain changes the flat-band states to the spatially localized states, while the electric field perpendicular to the chain changes it to the spatially extended states. Thus, the electronic current is sensitively changed by the direction of applied electric field. Moreover, we found that the transport characteristic changes from the quantum interference to noninterference regimes with increasing electric field perpendicular to the chain, and the current magnitude becomes nearly independent of the size of the Kagomé-lattice chain at the boundary of both regimes. The conditions for observing such current were also determined.

• Chapter 4

We developed the calculation method of time-dependent electronic current, using the density-matrix method and the projection-operator method under the tight-binding approximation. To simplify, we assumed that the Coulomb interaction doesn't work between electrons.

We applied the method to the simple joint systems which consist of two-bulk electrodes and a nanostructure. It was confirmed that the expected steady state is realized in the joint system. Furthermore, we confirmed that the nonequilibrium-Green-function method and the projected density-matrix method give the same steady electronic current in our model discussed in this work. Using the method developed in this thesis, we found that the oscillation of the transient currents originates from the quantum interference between the current from the electrode to the nanostructure and the inverse current.

In this thesis, we investigated the transport and optical properties of nanostructure network systems using the simple tight-binding models. Here, we should like to emphasize that the degeneracy and quantum interference of electronic states promote exotic properties in nanoscale systems. For example, we have clarified that the optical property is dramatically changed, when the degeneracy induced by the quantum interference is removed by an external field. Furthermore, we also clarified that the interference effects appear in the dynamics of nanostructure systems. We expect that the knowledge and method obtained in this thesis will give the new possibility to the future science.

Appendix A

Flat-band states

In this appendix, we review the characteristics of flat-band states originating from the interference of electron wavefunctions. Flat-band systems are classified into three types from the viewpoint of the mechanism of the flat-band appearance. The mechanisms are explained as follows [29].
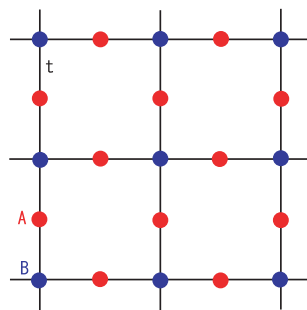
- Lieb type

Figure A.1: An example of Lieb-type lattices. The red (blue) circles represent the A (B) lattice points. The quantity, t, is the transfer energy of electrons.

- Tasaki type
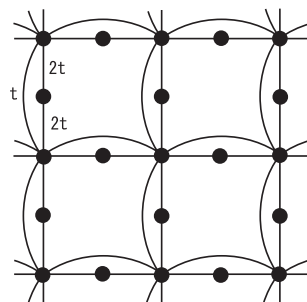
Figure A.2: An example of Tasaki-type lattices.

115
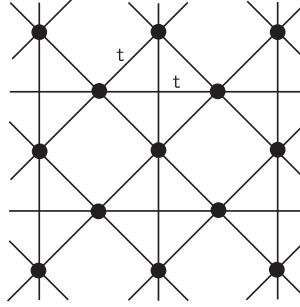
- Mielke type

Figure A.3: An example of Mielke-type lattices.

A.1   Lieb type

Lieb-type lattices have AB-sublattice structures as shown in Fig. A.1. The Hamiltonians of the conductive electrons in such lattices are written as follows,

$$\mathcal{H} = \left[\begin{array}{c|c} 0 & T_{AB} \\ \hline T_{BA} & 0 \end{array}\right], \tag{A.1}$$

where the matrix T_{AB} has the $|A|\times|B|$ dimension, and represents electron transfer between the A lattice points and the B lattice points. Here, $|A|$ means the number of the A lattice points. When the exchanges between the rows are operated on the above Hamiltonian matrix, the Hamiltonian is rewritten as follows,

$$\mathcal{H} = \left[\begin{array}{c|c} T_{BA} & 0 \\ \hline 0 & T_{AB} \end{array}\right]. \tag{A.2}$$

The number of the eigenstates with eigenvalue zero is more than $(|A|+|B|) - 2|B| = (|A|-|B|)$, because the rank of the matrix $\mathcal{H}$ is less than $2|B|$ as shown in Eq. (A.2). For example, the lattice shown in Fig. A.1 has two A-lattice points and one B-lattice point per unit cell, thus, the $(2-1)N$-fold degenerate eigenstates have the same eigenenergy, zero. Here, N is the number of unit cell of the lattice. These N-fold degenerate eigenstates produce the flat band, when the system size increases from the finite size with N unit cells to the periodic-infinite size.

In order that the systems have the multiple degenerate states with the eigenvalue zero, the following equation should be satisfied,
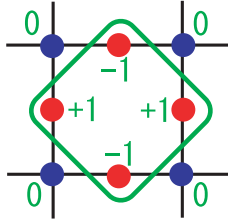
$$T_{AB}\mathbf{v} = \mathbf{0}, \tag{A.3}$$

Figure A.4: One of the flat-band eigenstates of the Lieb-type lattice shown in Fig. A.1.

where $\mathbf{v}$ is the $|A|$-dimensional vector. Using the knowledge of the linear algebra, we can show that there are $(|A|-|B|)$ vectors which satisfy Eq. (A.3). In other words, one of the eigenfunctions of Hamiltonian (A.1) with eigenvalue zero, ψ, is written as following form,

$$\psi = \begin{bmatrix} v_1 \\ v_2 \\ \vdots \\ v_{|A|} \\ 0 \\ \vdots \\ 0 \end{bmatrix}, \tag{A.4}$$

where v_i is the i-th component of vector $\mathbf{v}$. This result shows that the wavefunctions have the amplitude only on the A-lattice points. For example, in the Lieb-type lattice as shown in Fig. A.1, one of the degenerate eigenfunctions is localized in a unit cell as shown in figure A.4. The ±1 and 0 represent the wavefunction amplitudes. Such localized states exist similarly in the other unit cells. Thus, these localized eigenstates produce the flat band, when the system size changes from the finite size to the periodic-infinite size. Figure A.5 shows the electronic band structure of the lattice shown in Fig. A.1 [29]. Here, the electron transfer energy, t, is unity. The Lieb-type lattices always have a flat band in the center of the electronic band structure. Furthermore, we notice that the localized state has the overlap with the neighbor localized states. It shows that the Wannier functions of a flat-band eigenstates are extended over an entire system. It means that the flat-band electronic states have both localized and itinerant characteristics.

A.2 Tasaki type

In the previous section, we showed that the flat-band eigenstates are localized in each unit cell. Tasaki found that when the isolated small cell has the localized eigenstate, such localized states remain as the eigenstates in the larger systems made by the combination of the small cells. As well as the mechanism of the flat-band appearance of the Lieb type, the localized eigenstates produce the flat bands. In order to produce the localized state by the quantum interference, the shape of small cell is very important. The small cell must be a "complete graph", which
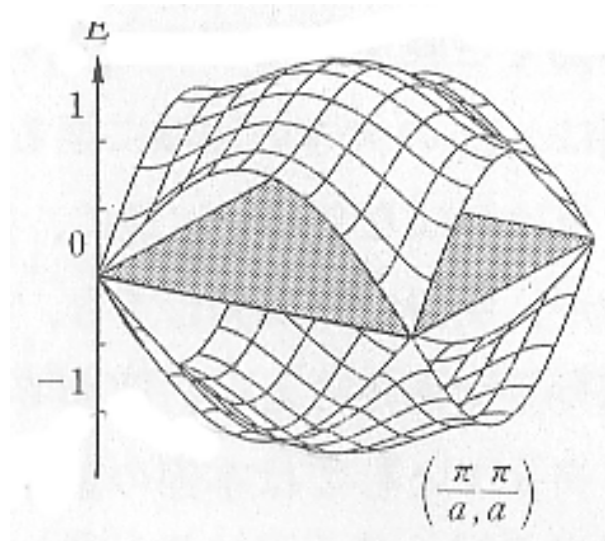
Figure A.5: The band structure of the Lieb-type lattice shown in Fig. A.1 [29].
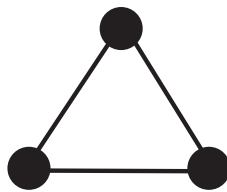

Figure A.6: The triangular cell.

have the bonds between all lattice points. The triangular cell as shown in Fig. A.6 is an example of a complete graph. When we set the electron transfer energy as unity, the Hamiltonian of the triangular cell is represented as follows,

$$\mathcal{H} = \begin{bmatrix} 1 & 1 & 1 \\ 1 & 1 & 1 \\ 1 & 1 & 1 \end{bmatrix}. \tag{A.5}$$

Here, it is assumed that the on-site energy is equal to the transfer energy. The triangular cell has the 2-fold degenerate eigenvalues, 0, and one eigenvalue, 3. The 2-fold degenerate eigenstates can be written as follows,

$$\psi^{(1)} = \begin{bmatrix} 0 \\ 1 \\ -1 \end{bmatrix}, \tag{A.6}$$

$$\psi^{(2)} = \begin{bmatrix} 1 \\ -1 \\ 0 \end{bmatrix}. \tag{A.7}$$

It is important that the above eigenstates have the node. In the Tasaki-type lattices, the eigenstate having the node remains even in the large systems made by the combination of the cells. Then, we explain the procedure to make localized eigenstates of the Tasaki-type lattices.

- Procedure 1.
  We consider the transformed triangular cell shown in Fig. A.7, instead of
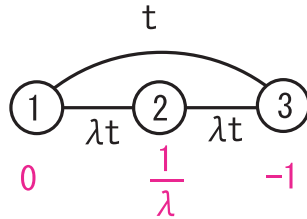

Figure A.7: The transformed triangular cell. The quantity t and λt represent the electron transfer energies. The lattice points are labeled by numbers in the lattice points. The red numbers represent the amplitudes of the wavefunction (A.10).

the triangular cell. We assume the Hamiltonian as follows,

$$\mathcal{H}_{cell} \equiv t(c_1^\dagger + \lambda c_2^\dagger + c_3^\dagger)(c_1 + \lambda c_2 + c_3)$$
$$= t \begin{bmatrix} 1 & \lambda & 1 \\ \lambda & \lambda^2 & \lambda \\ 1 & \lambda & 1 \end{bmatrix}, \tag{A.8}$$

where, c_i is the annihilation operator of electron at i-th lattice point. In order that the cell has the eigenvalue zero, the eigenfunction ψ_c should obey the following equation.

$$(c_1 + \lambda c_2 + c_3)\psi_c = 0. \tag{A.9}$$

Thus, the eigenfunctions with the eigenvalue zero can be selected as follows,

$$\psi_c^{(1)} = \begin{bmatrix} 0 \\ \frac{1}{\lambda} \\ -1 \end{bmatrix}, \tag{A.10}$$

$$\psi_c^{(2)} = \begin{bmatrix} -1 \\ \frac{1}{\lambda} \\ 0 \end{bmatrix}. \tag{A.11}$$

Note that these two eigenfunctions are independent and nonorthogonal each other.
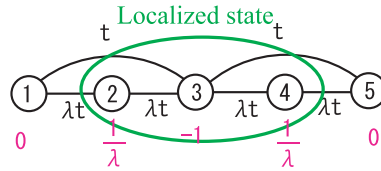
• Procedure 2.

Figure A.8: The finite system made by the combination of the two cells. The lattice points are labeled by numbers in the lattice points. The red numbers represent the amplitudes of the wavefunction.

Next, we connect the two cells as shown in Fig. A.8. The Hamiltonian of the system connected two cells is written as

$$\mathcal{H}_{2cell} = t \begin{bmatrix} 1 & \lambda & 1 & 0 & 0 \\ \lambda & \lambda^2 & \lambda & 0 & 0 \\ 1 & \lambda & 2 & \lambda & 1 \\ 0 & 0 & \lambda & \lambda^2 & \lambda \\ 0 & 0 & 1 & \lambda & 1 \end{bmatrix}. \tag{A.12}$$

The wavefunction which consist of the combination of the $\psi_c^{(1)}$ in the left-side cell and the $\psi_c^{(2)}$ in the right-side cell is the eigenfunction of above Hamiltonian. In other words, this Hamiltonian has the following eigenfunctions,

$$\psi_{2cell} = \begin{bmatrix} 0 \\ \frac{1}{\lambda} \\ -1 \\ \frac{1}{\lambda} \\ 0 \end{bmatrix}. \tag{A.13}$$

The wavefunction, ψ_{2cell}, is the localized eigenstates having the nodes at the edges. Furthermore, the wavefunction has the eigenvalue, zero.
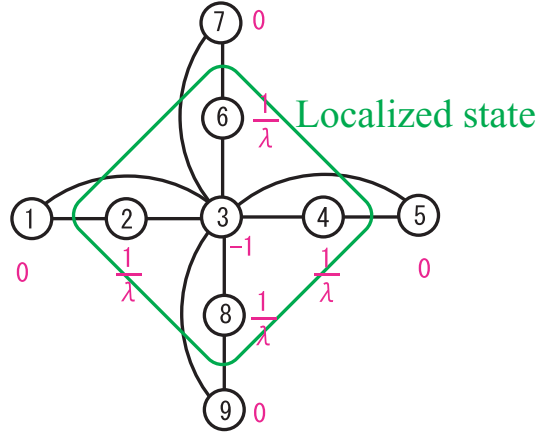
Figure A.9: The two-dimensional finite system made by the combination of the four cells. The lattice points are labeled by numbers in the lattice points. The red numbers represent the amplitudes of the wavefunction.

- Procedure 3.

Then, we repeat the procedure 2 and can build two-dimensional systems. For example, the Hamiltonian of the finite system consisting of the four cells as shown in Fig. A.9 can be written as,

$$\mathcal{H}_{4cell} = t \begin{bmatrix} 1 & \lambda & 1 & 0 & 0 & 0 & 0 & 0 & 0 \\ \lambda & \lambda^2 & \lambda & 0 & 0 & 0 & 0 & 0 & 0 \\ 1 & \lambda & 4 & \lambda & 1 & \lambda & 1 & \lambda & 1 \\ 0 & 0 & \lambda & \lambda^2 & \lambda & 0 & 0 & 0 & 0 \\ 0 & 0 & 1 & \lambda & 1 & 0 & 0 & 0 & 0 \\ 0 & 0 & \lambda & 0 & 0 & \lambda^2 & \lambda & 0 & 0 \\ 0 & 0 & 1 & 0 & 0 & \lambda & 1 & 0 & 0 \\ 0 & 0 & \lambda & 0 & 0 & 0 & 0 & \lambda^2 & \lambda \\ 0 & 0 & 1 & 0 & 0 & 0 & 0 & \lambda & 1 \end{bmatrix}, \qquad (A.14)$$

and a localized eigenstate, ψ_{4cell}, is obtained as follows,

$$\psi_{4cell} = \begin{bmatrix} 0 \\ \frac{1}{\lambda} \\ -1 \\ \frac{1}{\lambda} \\ 0 \\ \frac{1}{\lambda} \\ 0 \\ \frac{1}{\lambda} \\ 0 \end{bmatrix}. \qquad (A.15)$$

We can confirm that the wavefunction amplitudes become zero at the edges of the finite system and the eigenvalue of the state is zero.
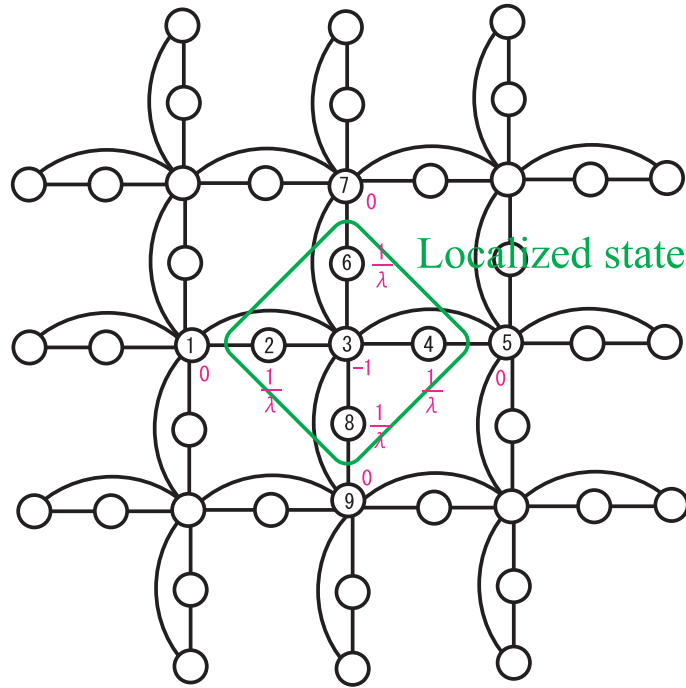
• Procedure 4.

Figure A.10: The two-dimensional finite system made by the combination of the many cells. The lattice points are labeled by numbers in the lattice points. The red numbers represent the amplitudes of the wavefunction.

Finally, as shown in Fig. A.10, we can build the much larger systems by linking the finite system shown in Fig. A.9 together at edges. In this process, the state ψ_{4cell} is still staying as the eigenfunction. Such localized eigenstate exist similarly in each unit cell. And all the localized eigenstates have zero eigenvalues, thus, the flat band appear in the electronic band structures. Figure A.11 represents the electronic band structure of the Tasaki-type lattice shown in Fig. A.2. The band structure has the band gap between the dispersive bands and the flat band.

A.3   Mielke type

In this section, we use the basic knowledge of graph theory [57] to explain the mechanism of flat-band appearance. Flat band is one of the characteristics of the line graph of the AB-sublattice systems. The Kagomé lattice is classed to the Mielke type.

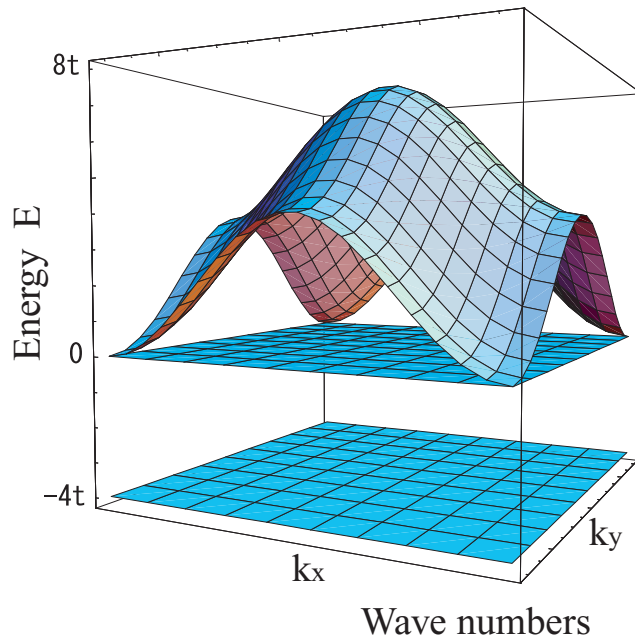### A.3.1   The basis of the graph theory

• Definition of the graph

Figure A.11: The electronic band structure of the Tasaki-type lattice which is shown in Fig. A.2 (in case of $\lambda = 2$). When the variable λ takes the value except for two, the flat band at $E = 0$ changes to the dispersive band. However the flat band at $E = -4t$ remains.

The graph, $G(V, E)$, means a collection of vertices (sites) and edges (bonds) between them. Here, V is the set of vertices, and E is the set of edges. The i-th vertex is represented by v_i, and the edge connecting between two vertexes, v_i and v_j, is represented by $e_{ij} \equiv (v_i, v_j)$. The graph $G(V, E)$ as shown in Fig. A.12 is represented as follows,

$$V = \{v_1, v_2, v_3, v_4\}, \tag{A.16}$$

$$\begin{aligned} E &= \{(v_1, v_2), (v_1, v_3), (v_3, v_2), (v_3, v_4)\} \\ &= \{e_{12}, e_{13}, e_{32}, e_{34}\}. \end{aligned} \tag{A.17}$$

We don't consider the graph where the interval of two vertices is connected by multiple edges or the edge connects a single vertex (loop edge), as shown in Fig. A.13.

- Plane graph

  When all edges cross only at vertexes, the graph is called the plane graph. For example, the graph as shown in Fig. A.14 isn't the plane graph.
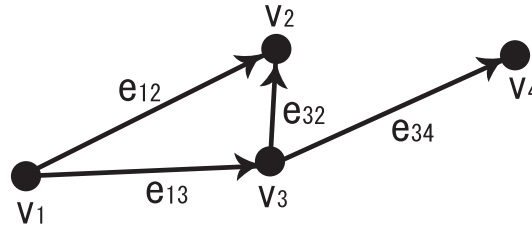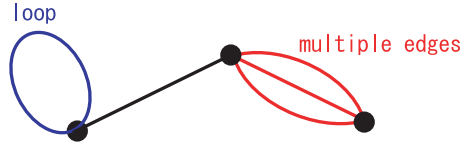
- Regular graph

Figure A.12: An example of the graph $G(V, E)$.

Figure A.13: An example which we don't call a graph.

When every vertex has the same degree, we call the graph the regular graph. In the graph theory, the degree of the vertex means the number of the vertexes which connect with it in edges.

- Adjacency matrix $A(G)$ and Incidence matrix $B(G)$ of the graph G

We define the adjacency matrix of the graph G to be the matrix $A(G) = \{a_{ij}\}$ where $a_{ij} = 1$ if the two vertices, v_i and v_j, are adjacent and $a_{ij} = 0$ otherwise. Thus, the adjacency matrix is written as follows,

$$a_{ij} = \begin{cases} 1 & e_{ij} \in E \\ 0 & e_{ij} \notin E \end{cases}. \tag{A.18}$$

The adjacency matrix is the $|V| \times |V|$ dimensional matrix. Here, $|V|$ represents the number of the vertexes of the graph G.

Furthermore we introduce the following incidence matrix $B(G) = \{b_{ij}\}$ of the graph G,

$$b_{ij} = \begin{cases} 1 & \text{if } v_i \text{ is the starting point of the edge } e_{j(\equiv kl)} \text{ (or if } i = k) \\ -1 & \text{if } v_i \text{ is the end point of the edge } e_{j(\equiv kl)} \text{ (or if } i = l) \\ 0 & \text{otherwise} \end{cases}. \tag{A.19}$$

The incidence matrix is the $|V| \times |E|$ dimensional matrix.

A.3.2   Line graph

We show the procedure for making the line graph L_G from the graph G. As an example, it is shown that the Kagomé lattice is the line graph of the hexagonal lattice.
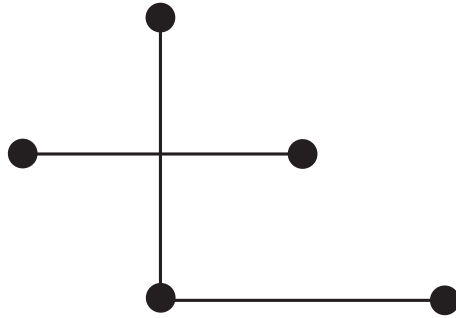
Figure A.14: The example which we don't call a plane graph.

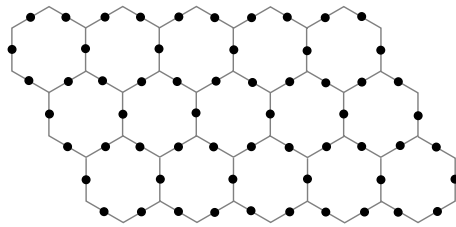(1) As shown in Fig. A.15, we add the new vertexes $\{v_L\}$ to the center of every edge of graph G.

Figure A.15: The hexagonal lattice G (solid lines) and the added vertexes $\{v_L\}$ (solid circles).

(2) If an edge of the graph G is connected to another edge at a vertex, new edge e_L is drawn between the two vertexes v_L on these edges. We call the new graph which is produced by above procedure "a line graph of G", and express it with $L_G(V_L, E_L)$. Here $V_L(E_L)$ is the collection of the $\{v_L(e_L)\}$
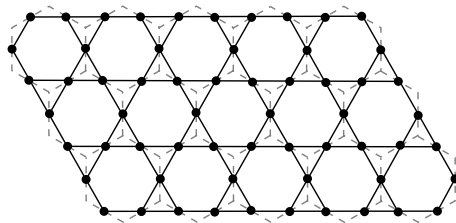

Figure A.16: The broken lines represent the hexagonal lattice G, and the solid lines is the Kagomé lattice which is the line graph L_G of the hexagonal lattice.

Figure A.16 shows that the Kagomé lattice is the line graph of the hexagonal lattice. The lattice shown in Fig. A.3 is the line graph of the square lattice.

A.3.3   Theorem of the graph theory

(1) Theorem 1.

   If the graph G is a plane graph, we have the following equation [57].

   $$A(G) = D(G) - B(G) \cdot B(G)^t, \tag{A.20}$$

   where the matrix $D(G)$ is defined as

   $$d_{ij} = \begin{cases} \text{the degree of the vertex } v_i & \text{for } i = j \\ 0 & \text{for } i \neq j \end{cases}. \tag{A.21}$$

   In the graph theory, the degree of the vertex means the number of the vertexes which connect with it in edges. In case that the graph G is a regular graph, the matrix $D(G)$ is rewritten as follows,

   $$D(G) = z I_{|V|}, \tag{A.22}$$

   where z is the degree of the vertex, and $I_{|V|}$ represents the $|V| \times |V|$ unit matrix. Thus, Eq. (A.20) may be written as

   $$A(G) = z I_{|V|} - B(G) \cdot B(G)^t. \tag{A.23}$$

   The proof of the equation (A.20).

   Because the component of the matrix $(BB^t)_{ij}$ is written by $\sum_{l=1}^{m} b_{il} b_{jl}$, if $i = j$, the components of $(BB^t)_{ii}$ are equal to the degree of the vertex v_i: if edge(v_i, v_j) $(i \neq j)$ is one of the edge of the graph G, the component of $(BB^t)_{ii}$ is equal to -1: otherwise, the component of $(BB^t)_{ii}$ becomes zero.

(2) Theorem 2.

   If the graph G is a plane graph, a regular graph, and an AB sublattice structure, we have a following equation [22–24],

   $$A(L_G) = B(G)^t \cdot B(G) - 2 I_{|E|}. \tag{A.24}$$

   Here, every direction of the edge is unified from the vertex of the A sublattice to that of the B sublattice.

(3) Theorem 3.

   The incidence matrix $B(G)$ is linear map which projects the $|E|$ dimensional space to the $|V|$ dimensional space. The any closed path space c in the graph G is the kernel of the $B(G)$. In other words, if a closed path in the graph G is shown by $\mathbf{z}_c$, we obtain following equation [57],

   $$B(G)\mathbf{z}_c = \mathbf{0}. \tag{A.25}$$
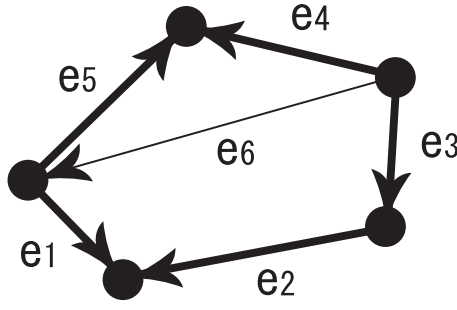
   Definition of the closed path $\mathbf{z}_c$

Figure A.17: An example of the closed path $\mathbf{z}_c$.

The closed path space c has the orientation, and is defined as,

$$
\mathbf{z}_c = \begin{cases} 1 & \text{if the closed path } c \text{ contains } e_i \text{ and } e_i \text{ and } c \text{ have the same orientation} \\ -1 & \text{if the closed path } c \text{ contains } e_i \text{ and } e_i \text{ and } c \text{ have opposite orientation} \\ 0 & \text{if the closed path } c \text{ does not contain } e_i. \end{cases}
\tag{A.26}
$$

For example, in case of Fig. A.17, the collection of the edge is written by,

$$
V = \{e_1, e_2, e_3, e_4, e_5, e_6\}.
\tag{A.27}
$$

We set anticlockwise closed path space c which is shown by bold solid lines in Fig. A.17. Then the closed path $\mathbf{z}_c$ can be written as,

$$
\mathbf{z}_c = \{\overset{e_1}{1}, \overset{e_2}{-1}, \overset{e_3}{-1}, \overset{e_4}{1}, \overset{e_5}{-1}, \overset{e_6}{0}\}.
\tag{A.28}
$$

A.3.4 Flat band and Graph theory

We used the following Hamiltonian under the tight-binding approximation in this paper,

$$
\mathcal{H} = \sum_{i,j} t_{ij} \hat{a}_i^\dagger \hat{a}_j.
\tag{A.29}
$$

In case that $t_{ij} = 1$, we can consider that the lattice points and the bonds between them of the tight-binding models correspond to the vertexes and the edges of the graph, respectively. Thus, the Hamiltonian matrix (A.29) is equal to the adjacency matrix (A.18).

We have already shown that the line graph L_G of the hexagonal lattice G is the Kagomé lattice. To obtain the eigenstates of the Kagomé lattice, we diagonalize the adjacency matrix $A(L_G)$. The shrödinger equation to be solved is written as follow, using the adjacency matrix,

$$
A(L_G)\Psi_{|E|}^L = E_L \Psi_{|E|}^L,
\tag{A.30}
$$

where $\Psi_{|E|}^L$ and E_L represent the eigenvectors and the eigenenergies, respectively. Substituting Eq. (A.24) into Eq. (A.30), we obtain

$$
B(G)^t \cdot B(G)\Psi_{|E|}^L - 2\Psi_{|E|}^L = E_L \Psi_{|E|}^L.
\tag{A.31}
$$

If we take the closed path $\mathbf{z}_c$ in the hexagonal lattice G as $\Psi^L_{|E|}$, the shrödinger equation is rewritten as follows by using Eq. (A.25),

$$-2\Psi^L_{|E|} = E_L \Psi^L_{|E|}. \tag{A.32}$$

The result means that the closed paths $\mathbf{z}_c$ are the eigenvectors. Furthermore, such closed paths innumerable exist. Thus the eigenvectors correspond to the flat-band eigenstates. The degree of the degeneracy is equivalent to the number of the linear independent closed paths, as shown in Fig. A.18.
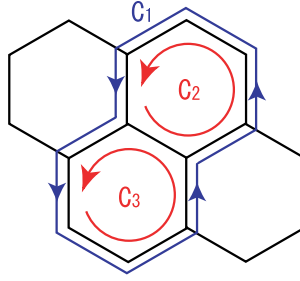

Figure A.18: A closed path c_1 is decomposed to two linear independent closed paths c_2 and c_3.

A.3.5   Flat-band eigenstates

A linear independent closed path of the hexagonal lattice is shown in Fig. A.19. The closed path is written as

$$\mathbf{z}_c = \{\overset{e_{12}}{0}, \overset{e_{14}}{0}, \overset{e_{16}}{0}, \overset{e_{32}}{+1}, \overset{e_{34}}{-1}, \overset{e_{38}}{0}, \overset{e_{52}}{-1}, \overset{e_{56}}{+1}, \overset{e_{58}}{0}, \overset{e_{74}}{+1}, \overset{e_{76}}{-1}, \overset{e_{78}}{0}\}. \tag{A.33}$$

The closed path (A.33) is equivalent to a flat-band eigenstate, because the edges of hexagonal lattice correspond to the vertexes of the Kagomé lattice. Thus, as shown in Fig. A.20, we obtain a flat-band eigenstate localized around hexagonal area

$$\Psi^L_{|E|} = \{\overset{e_{12}}{0}, \overset{e_{14}}{0}, \overset{e_{16}}{0}, \overset{e_{32}}{+1}, \overset{e_{34}}{-1}, \overset{e_{38}}{0}, \overset{e_{52}}{-1}, \overset{e_{56}}{+1}, \overset{e_{58}}{0}, \overset{e_{74}}{+1}, \overset{e_{76}}{-1}, \overset{e_{78}}{0}\}. \tag{A.34}$$

Such localized states exist similarly in each hexagonal area and produce the flat-band states. The degree of the degeneracy is equivalent to the number of the unit cell, because the linear independent closed paths exist at each hexagonal ring. Flat-band eigenstates make the nonorthogonal system. The electronic band structure of the Kagomé lattice is shown in Fig. A.21(b). A flat band of the Mielke type lattices appears at the $E = -2$.

A.3.6   Band structure except flat band

In this subsection, we show the relation of the dispersive band structures between a graph G (ex. hexagonal lattice) and the line graph L_G (ex. Kagomé lattice). The
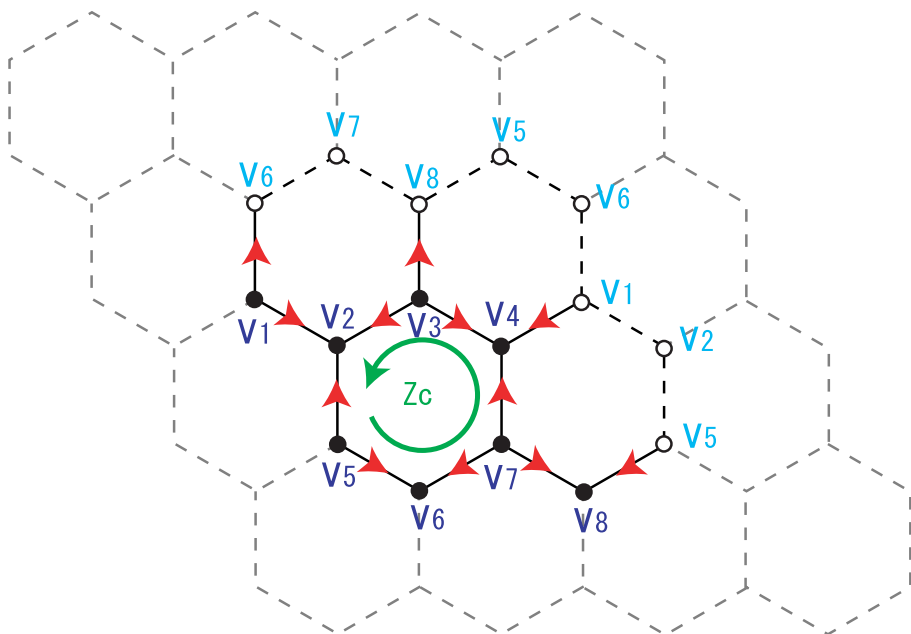
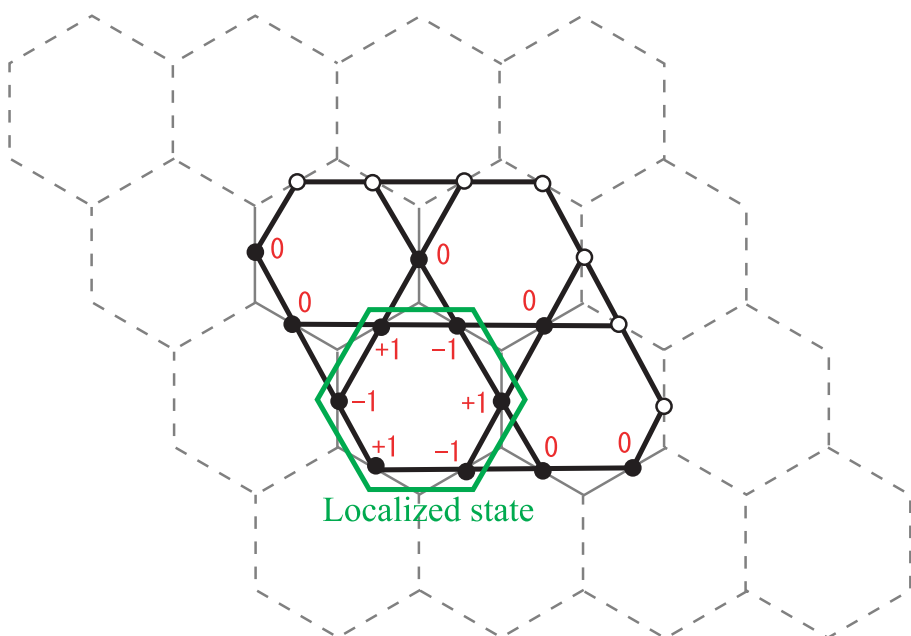Figure A.19: A linear independent closed path $\mathbf{z}_c$ of the hexagonal lattice.

Figure A.20: A localized eigenstate of the Kagomé lattice.

following equation is the Schrödinger equation of the graph G,

$$A(G)\Psi_{|V|}^G = E_G\Psi_{|V|}^G, \tag{A.35}$$

where $\Psi_{|V|}^G$ and E_G represent the eigenvectors and the eigenvalues of the graph G. Substituting Eq. (A.23) into Eq. (A.35), we obtain

$$z\Psi_{|V|}^G - B(G) \cdot B(G)^t\Psi_{|V|}^G = E_G\Psi_{|V|}^G \tag{A.36}$$

,where z represents the degree of the vertex of the graph G. In case of the hexagonal lattice, z is equal to the 3. On the other hand, the Schrödinger equation of the line graph G can be written using Eq. (A.24) as follows,

$$B(G)^t \cdot B(G)\Psi_{|E|}^L - 2\Psi_{|E|}^L = E_L\Psi_{|E|}^L. \tag{A.37}$$

We can prove that the eigenvalues except zero of the $(B(G)^t \cdot B(G))$ are equal to the eigenvalues of the $(B(G) \cdot B(G)^t)$, thus, using Eq. (A.36) and Eq. (A.37) we obtain

$$E_L = z - 2 - E_G. \tag{A.38}$$

If the graph G has the AB-sublattice structure, the band structures become symmetric for E=0. Thus, the relation of the dispersive band structures between a graph G and the line graph L_G is deduced as follows,

$$E_L = z - 2 + E_G. \tag{A.39}$$

As an example, we show the band structures of the hexagonal lattice (G) and Kagomé lattice (L_G) in Fig. A.21(a) and Fig. A.21(b), respectively.
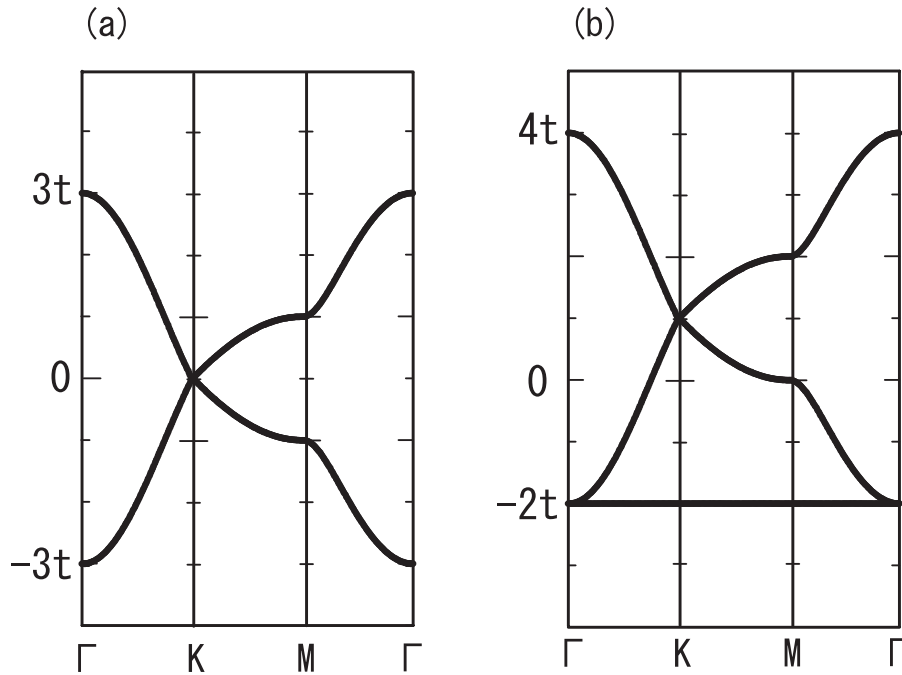
Figure A.21: (a) The band structures of the hexagonal lattice and (b) the Kagomé lattice.

A.4   Summary

(1) Lieb type

Condition; AB-sublattice structure with the difference in the lattice point number of A-sublattice and B-sublattice.

Characteristics; A flat band appears at the $E = 0$, because the band structures of the AB-sublattice structures become symmetric for E=0.

(2) Tasaki type

Condition; The existence of the complete graph cell.

Characteristics; The band structure has the band gap between the dispersive bands and the flat band.

(3) Mielke type

Condition; The line graph L_G of the AB-sublattice structure G in the plane graphs.

Characteristics; The flat band appears at $E = -2t$. The dispersive band structures of the L_G and G are the identical.

References

[1] R. A. Webb, S. Washburn, C. P. Umbach, and R. B. Laibowitz. Observation of h/e aharonov-bohm oscillations in normal-metal rings. *Phys. Rev. Lett.*, Vol. 54, pp. 2696–2699, 1985.

[2] B. J. van Wees, H. van Houten, C. W. J. Beenakker, J. G. Williamson, L. P. Kouwenhoven, D. van der Marel, and C. T. Foxon. Quantized conductance of point contacts in a two-dimensional electron gas. *Phys. Rev. Lett.*, Vol. 60, pp. 848–850, 1988.

[3] T. Komeda, Y. Kim, M. Kawai, B. N. J. Persson, and H. Ueba. Lateral hopping of molecules induced by excitation of internal vibration mode. *Science*, Vol. 295, pp. 2055–2058, 2002.

[4] B. C. Stipe, M. A. Rezaei, and W. Ho. Coupling of vibrational excitation to the rotational motion of a single adsorbed molecule. *Phys. Rev. Lett.*, Vol. 81, pp. 1263–1266, 1998.

[5] Y. Kim, T. Komeda, and M. Kawai. Single-molecule reaction and characterization by vibrational excitation. *Phys. Rev. Lett.*, Vol. 89, pp. 126104–1–126104–4, 2002.

[6] J. I. Pascual, N. Lorente, Z. Song, H. Conrad, and H.-P. Rust. Selectivity in vibrationally mediated single-molecule chemistry. *Nature*, Vol. 423, pp. 525–528, 2003.

[7] B. N. J. Persson and A. Baratoff. Inelastic electron tunneling from a metal tip: The contribution from resonant processes. *Phys. Rev. Lett.*, Vol. 59, pp. 339–342, 1987.

[8] K. Kumakura, J. Motohisa, and T. Fukui. Formation and characterization of coupled quantum dots (CQDs) by selective area metalorganic vapor phase epitaxy. *J. Cryst. Growth.*, Vol. 170, pp. 700–704, 1997.

[9] P. Mohan, F. Nakajima, M. Akabori, J. Motohisa, and T. Fukui. Fabrication of semiconductor kagome lattice structure by selective area metalorganic vapor phase epitaxy. *Appl. Phys. Lett.*, Vol. 83, pp. 689–691, 2003.

[10] P. Mohan, J. Motohisa, and T. Fukui. Realization of inas-based two-dimensional artificial lattice by selective area metalorganic vapor phase epitaxy. *Appl. Phys. Lett.*, Vol. 84, pp. 2664–2666, 2004.

[11] J. Motohisa and T. Fukui. *unpublished*.

[12] K. Shiraishi, H. Tamura, and H. Takayanagi. Design of a semiconductor ferromagnet in a quantum-dot artificial crystal. *Appl. Phys. Lett.*, Vol. 78, pp. 3702–3704, 2001.

[13] D. R. Hofstadter. Energy levels and wave functions of Bloch electrons in rational and irrational magnetic fields. *Phys. Rev. B*, Vol. 14, pp. 2239–2249, 1976.

[14] C. Albrecht, J. H. Smet, K. von Klitzing, V. Umansky D. Weiss, and H. Schweizer. Evidence of Hofstadter's fractal energy spectrum in the quantized hall conductance. *Phys. Rev. Lett.*, Vol. 86, pp. 147–150, 2001.

[15] B. Moulton, J. Lu, R. Hajndl, S. Hariharan, and M. J. Zaworotko. Crystal Engineering of a Nanoscale Kagomé Lattice. *Angew. Chem. Int. Ed.*, Vol. 41, pp. 2821–2824, 2002.

[16] G. R. Desiraju. Supramolecular synthons in crystal engineering - a new organic synthesis. *Angew. Chem. Int. Ed. Engl.*, Vol. 34, pp. 2311–2327, 1995.

[17] B. Moulton and M. J. Zaworotko. From molecules to crystal engineering: Supramolecular isomerism and polymorphism in network solids. *Chem. Rev.*, Vol. 101, pp. 1629–1658, 2001.

[18] J. L. Atwood. Kagomé lattice: A molecular toolkit for magnetism. *Nature Materials*, Vol. 1, pp. 91–92, 2002.

[19] W. Schmitt, J. P. Hill, M. P. Juanico, A. Caneschi, F. Costantino, C. E. Anson, and A. K. Powell. Supramolecular coordination assemblies of dinuclear FeIII complexes. *Angew. Chem. Int. Ed.*, Vol. 44, pp. 4187–4192, 2005.

[20] K. Tagami and M. Tsukada. Current-controlled magnetism in T-shape tapeporphyrin molecular bridges. *Current Applied Physics*, Vol. 3, pp. 439–444, 2003.

[21] K. Tagami and M. Tsukada. A novel viewpoint for source-drain driven current inside triangular nanographene : Close relationship with magnetic current. *e-J. Surf. Sci. Nanotech.*, Vol. 2, pp. 205–209, 2004.

[22] A. Mielke. Ferromagnetic ground states for the Hubbard model on line graphs. *J. Phys. A: Math. Gen.*, Vol. 24, pp. L73–L77, 1991.

[23] A. Mielke. Ferromagnetism in the Hubbard model on line graphs and further considerations. *J. Phys. A: Math. Gen.*, Vol. 24, pp. 3311–3321, 1991.

[24] A. Mielke. Exact ground states for the Hubbard model on the Kagome lattice. *J. Phys. A: Math. Gen.*, Vol. 25, pp. 4335–4345, 1992.

[25] A. Mielke and H. Tasaki. Ferromagnetism in the Hubbard model. Examples from models with degenerate single-electron ground states. *Commun. Math. Phys.*, Vol. 158, pp. 341–371, 1993.

[26] K. Shiraishi, H. Tamura, and H. Takayanagi. *unpublished*.

[27] E. H. Lieb. Two theorems on the Hubbard model. *Phys. Rev. Lett.*, Vol. 62, pp. 1201–1204, 1989.

[28] E. H. Lieb. Two theorems on the Hubbard model (Erratum). *Phys. Rev. Lett.*, Vol. 62, p. 1927, 1989.

[29] K. Kusakabe and H. Aoki. *Tataidensiron I kyoujisei*. University of Tokyo Press.

[30] Hartmut Haug and Stephan W. Koch. *Quantum theory of the optical and electronic properties of semiconductors (Third edition)*. World Scientific, 1994.

[31] K. Ishida. Dimensional crossover in excitons on a square lattice. *Phys. Rev. B*, Vol. 49, pp. 5541–5548, 1994.

[32] K. Ishida, H. Aoki, and T. Chikyu. One-dimensional exciton in a two-band tight-binding model with long-range interactions. *Phys. Rev. B*, Vol. 47, pp. 7594–7597, 1993.

[33] K. Kusakabe and H. Aoki. Ferromagnetic spin-wave theory in the multiband hubbard model having a flat band. *Phys. Rev. Lett.*, Vol. 72, pp. 144–147, 1994.

[34] Y. Hasegawa, Y. Hatsugai, M. Kohmoto, and G. Montambaux. Stabilization of flux states on two-dimensional lattices. *Phys. Rev. B*, Vol. 41, pp. 9174–9182, 1990.

[35] T. Kimura, H. Tamura, K. Shiraishi, and H. Takayanagi. Magnetic-field effects on a two-dimensional Kagomé lattice of quantum dots. *Phys. Rev. B*, Vol. 65, pp. 081307(R)–1–081307(R)–4, 2002.

[36] H. ishii, T. Nakayama, and J. I. Inoue. Flat-band exciton in two-dimensional Kagomé quantum wire systems. *Phys. Rev. B*, Vol. 69, pp. 085325–1–085325–7, 2004.

[37] L. V. Keldysh. Diagram technique for nonequilibrium processes. *Sov. Phys. JETP*, Vol. 20, pp. 1018–1026, 1965.

[38] C. Caroli, R. Combescot, P. Nozieres, and D. Saint-James. Direct calculation of the tunneling current. *J. Phys. C: Solid St. Phys.*, Vol. 4, pp. 916–929, 1971.

[39] S. Hershfield, J. H. Davies, and J. W. Wilkins. Resonant tunneling through an Anderson impurity. I. Current in the symmetric model. *Phys. Rev. B*, Vol. 46, pp. 7046–7060, 1992.

[40] H. Ishii and T. Nakayama. Quantum Electron Transport in Finite-size Flatband Kagome Lattice Systems. *Physics of Semiconductors 27th International Conference on the Physics of Semiconductors, edited by J. Menéndez and C. G. Van de Walle*, Vol. CP772, pp. 1285–1286, 2005.

[41] T. Fujikawa and H. Arai. Nonequilibrium Green's function approach to core spectroscopies. *Recent Res. Devel. Physics*, Vol. 4, pp. 657–703, 2003.

[42] E. M. Lifshitz and L. P. Pitaevskii. *Physical Kinetics (Course of Theoretical Physics)*. Butterworth-Heinemann, 1981.

[43] B. Naser, J. Heeren, and D. K. Ferry. 50-Ohm-matched system for low-temperature measurement of the time-resolved conductance of low-dimensional semiconductors. *preprint*.

[44] J. Park, A. N. Pasupathy, J. I. Goldsmith, C. Chang, Y. Yaish, J. R. Petta, M. Rinkoski, J. P. Sethna, H. D. Abruña, P. L. McEuen, and D. C. Ralph. Coulomb blockade and the Kondo effect in single-atom transistors. *Nature*, Vol. 417, pp. 722–725, 2002.

[45] M. A. Reed, C. Zhou, C. J. Muller, T. P. Burgin, and J. M. Tour. Conductance of a molecular junction. *Science*, Vol. 278, pp. 252–254, 1997.

[46] S. J. Tans, M. H. Devoret, H. Dai, A. Thess, R. E. Smalley, L. J. Geerligs, and C. Dekker. Individual single-wall carbon nanotubes as quantum wires. *Nature*, Vol. 386, pp. 474–477, 1997.

[47] T.-H. Lee and R. M. Dickson. Single-molecule LEDs from nanoscale electroluminescent junctions. *J. Phys. Chem. B*, Vol. 107, pp. 7387–7390, 2003.

[48] A. Mitra, I. Aleiner, and A. J. Millis. Phonon effects in molecular transistors: Quantal and classical treatment. *Phys. Rev. B*, Vol. 69, pp. 245302–1–245302–21, 2004.

[49] N. Mingo, K. Makoshi, T. Mii, and H. Ueba. Theory of the relation between inelastic scanning tunneling spectroscopy of adsorbates and their vibrational deexcitation. *Surf. Sci.*, Vol. 482-485, pp. 96–100, 2001.

[50] Toshiaki Iitaka. *Ryousi dainamikusu nyuumonn (Parithi butsurigaku kosu)*. Maruzen, 1994.

[51] Hideki Yukuwa, editor. Toukei butsurigaku (Iwanami-kouza Gendaibutsurigaku no kizo, 2nd ed.). Iwanami shoten, 1978.

[52] H. Ishii, T. Nakayama, and J. Inoue. Flat-band exciton states in kagome semiconductor quantum-wire lattices. *The Proceedings of the 26th International Conference on the Physics of Semiconductors, edited by A. R. Long and J. H. Davies (IOP publishing)*, pp. CD–P207, 2002.

[53] H. Ishii, T. Nakayama, and J. Inoue. Flat-band excitonic states in kagome lattice on semiconductor surfaces. *Surf. Sci.*, Vol. 514, pp. 206–210, 2002.

[54] H. Ishii and T. Nakayama. Exciton and Quantum Transport in Kagome Bond-Network System. *Proc. Int. Symp. Super-Functionality Organic Devices*, Vol. IPAP Conf. Series 6, pp. 91–94, 2005.

[55] H. Ishii and T. Nakayama. Symmetry Breaking and Electron Transport in Kagome-Chain Systems. *e-J. Surf. Sci. Nanotech.*, Vol. 3, , 2005.

[56] J. Inoue, H. Ishii, and T. Nakayama. Nonlinear optical response from kagome quantum dot array. *J. Lumin.*, Vol. 102-103, pp. 226–231, 2003.

[57] B. Bollobás. *GRAPH THEORY An Introductory Course*. Springer-Verlag, 1979.

Publications

(1) H. Ishii, T. Nakayama, and J. Inoue:" Flat-band excitonic states in Kagome lattice on semiconductor surfaces ", Surf. Sci. **514** 206 (2002)

(2) H. Ishii, T. Nakayama and J. Inoue:" Flat-band Exciton States in Kagome Semiconductor Quantum-wire Lattice ", Physics of Semiconductors 26th International Conference on the Physics of semiconductors **171** P207 (2002)

(3) H. Ishii, T. Nakayama, and J. I. Inoue:" Flat-band exciton in two-dimensional Kagome quantum wire systems ", Phys. Rev. B **69** 085325 (2004)

(4) H. Ishii and T. Nakayama:" Quantum Electron Transport in Finite-size Flat-band Kagome Lattice Systems ", Physics of Semiconductors 27th International Conference on the Physics of semiconductors CP**772** 1285 (2005)

(5) H. Ishii and T. Nakayama: " Exciton and Quantum Transport in Kagome Bond-Network System ", Proc. Int. Symp. Super-Functionality Organic Devices, IPAP Conf. Series **6** 91 (2005)

(6) H. Ishii and T. Nakayama:" Symmetry Breaking and Electron Transport in Kagome-Chain Systems ", e-J. Surf. Sci. Nanotech. **3** 399 (2005)

(7) J. Inoue, H. Ishii, and T. Nakayama: " Nonlinear optical response from Kagome quantum dot array", Journal of Luminescence, **102-103** 226 (2003)